Excess noise of an Er/Yb fiber superfluorescent radiation source

É. I. Alekseev, E. N. Bazarov, Yu. A. Barannikov, V. P. Gapontsev, V. P. Gubin, I. E. Samartsev, and N. I. Starostin

Instutute of Radio Engineering and Electronics, Russian Academy of Sciences, Fryazino
(Submitted February 24, 1997)
Pis'ma Zh. Tekh. Fiz. **23**, 1–6 (December 12, 1997)

A study is made of the noise in the output intensity of a high-power superfluorescent fiber radiation source generating 20 mW in the 1.55 μm region of the spectrum. The source is constructed in an all-fiber technology from a quartz fiber activated with ytterbium and erbium. It is found that the spectral density of the noise in the frequency range 100–500 kHz is uniform and corresponds to the excess noise of ''thermal'' sources. It is shown that the noise in the output intensity of the source can be compensated (decreased by an order of magnitude) in a two-channel scheme of photodetection, where it approaches a level close to the photon shot noise. © *1997 American Institute of Physics.* [S1063-7850(97)00112-2]

Superfluorescent fiber radiation sources with diode pumping are promising for use in low-coherence interferometry (white-light interferometry) and its applications, e.g., in fiber-optic gyroscopes.[1] To obtain a high sensitivity of the interferometric sensor it is necessary to have a high radiation power in the fiber and a low noise level. One way of making high-power superfluorescent fiber sources (generating more than 10 mW at 1.55 μm) is to use fibers with several activators in efficient optical pumping schemes with an all-fiber technology of the superfluorescent fiber sources. In schemes of this kind one can expect some additional intensity noise besides the excess noise inherent to all wide-band (''thermal'') sources.[2] It is also of interest to explore the possibility of compensating the intensity noise[3] to the fundamental shot-noise limit.

The present paper reports an experimental investigation of the noise characteristics of a high-power Er/Yb superfluorescent fiber source which also utilizes active stabilization of the radiation output power.

A simplified scheme of the superfluorescent fiber source (SFS) is shown in Fig. 1, which also shows a block diagram of the apparatus for measuring the noise of this source. The activated fiber (AF) has a core doped with erbium and ytterbium at concentrations of 0.1 and 2 wt.%, respectively. The cutoff wavelength of the higher mode of the activated fiber is 1.1 μm. Pump radiation at a wavelength of 0.98 μm from a multimode laser diode (LD) with a fiber output is coupled into the activated fiber by means of a special single-to-multimode fiber directional coupler-multiplexer (DCM) fabricated at the end of a length of activated fiber. An optical isolator (OI) with fiber input–output is used to reduce the influence of reflections on the parameters of the superfluorescent fiber source.

The source utilized active stabilization of the output power by means of an automatic regulation system which reduced the slow fluctuations to a level of less than 0.5%. The output power of the superfluorescent fiber source was 20 mW. The stability of the mean wavelength of the radiation spectrum was around 0.01 nm (upon a change in the temperature of the medium by 1°C). The spectrum had a double-humped shape analogous to that given in Ref. 4, with a power-weighted mean spectral width of 8 nm. The residual polarization of the output radiation of the superfluorescent fiber source was around 0.4%.

Radiation from the fiber output of the investigated superfluorescent fiber source passed through an attenuator (A) and a fiber polarizer (P) to the entrance of a fiber directional coupler (DC), the two outputs of which are connected to photodetectors ($PD_{1,2}$) through attenuators (A_1 and A_2). The attenuators A and $A_{1,2}$ were devices with a variable gap between the ends of two fibers. The noise from the outputs of the photodetectors was amplified by identical amplifiers ($Amp_{1,2}$) having a passband extending from 100 Hz to 1 MHz and was then sent to a computing device (CD). The electronics had provisions for equalizing the amplitudes and phase characteristics of the two channels. The noise at the output of the CD was detected by means of a spectrum analyzer (SA) and oscilloscope (OS).

It should be noted that measurements of the noise of the superfluorescent fiber source on our apparatus gave identical results with and without the polarizer. This can be attributed to the high polarization symmetry of the measuring apparatus.

Figure 2 shows the rms noise current i_n at the entrance of the photodetector as a function of the mean current of the photodetector. Measurements were made in a band $\Delta f = 100$ Hz at a center frequency of the spectrum analyzer $f = 100$ kHz, and the values of i_n were rescaled to a bandwidth of 1 Hz. Curve *1* corresponds to the noise for one channel, and curve *2* to that for both channels for the same power of the light incident on the photodetector. The measured noise in a single channel is described well by the relation for the excess noise of a wideband source (curve *3*):

$$i_n = (\lambda_0^2 \Delta f / c \Delta\lambda)^{1/2} I_0, \tag{1}$$

where λ_0 and $\Delta\lambda$ are the power-weighted (for a power spectrum $P(\lambda)$) mean wavelength and spectral width of the radiation from the source, $q \simeq 0.8$ A/W is the quantum sensitivity of the photodetector in the 1.55 μm region; c is the speed of light in vacuum, $I_0 = qP_0$ is the mean current of the photodetector (P_0 is the mean power of the light incident on

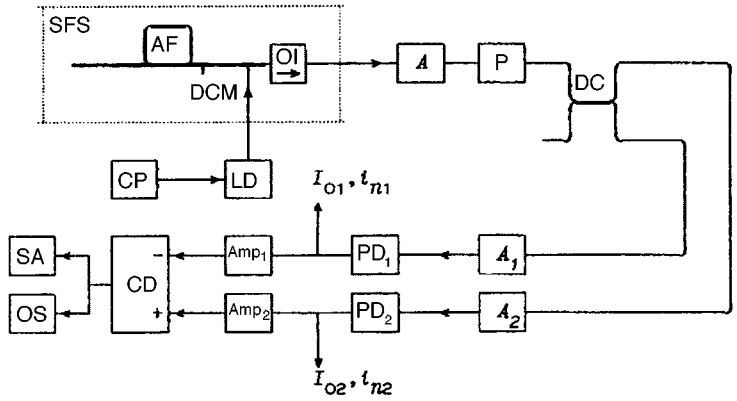

FIG. 1.

the photodetector). We note the good agreement between the theory and experiment (curves *3* and *1*).

The quantitative agreement of curves *1* and *3* indicates that the other noise mechanisms besides the ''classical'' excess noise considered above give only a small contribution to the resultant noise in Er/Yb superfluorescent fiber sources at $f=100$ kHz. In the case of two working channels the noise delivered to the input of a single photodetector cannot be less than a limiting value determined by the shot noise of the radiation,

$$i_n=(2)^{1/2}(2eI_0\Delta f\ )^{1/2}, \tag{2}$$

where e is the charge of an electron, and the factor of $2^{1/2}$ takes into account the addition of uncorrelated shot noise in the two channels. Equation (2) is plotted by curve *4* in Fig. 2, from which it follows that the excess noise of the source in a two-channel photodetection scheme can be compensated to a level approximately 3 times higher than the shot-noise limit.

The factors limiting the compensation of the intensity noise have not yet been studied. It can be noted, however, that such factors as inequality of the optical power incident on the photodetector or differences in the optical spectra at the outputs of the directional couplers (which, in general, do occur) are not the factors limiting the noise in our experiment, since they lead to a dependence of the form $i_n\sim I_0$, whereas in our experiment $i_n\sim I_0^{1/2}$.

We note that a dependence of the form $i_n\sim I_0$ in the noise-compensation regime is observed at high light powers incident on the photodetector (for $I_0\geqslant 1$ mA).

Figure 3 shows the noise spectrum $i_n(f\ )$ for the region of Fourier frequencies $f=15-500$ kHz, measured for a single channel at a mean photodetector current $I_0\simeq 0.4$ mA. The increase in noise in the low-frequency region ($f<50$ kHz) points to the existence of other sources of intensity noise besides the excess noise. These might include mode noise of the pump laser diode and redistribution in the fiber directional couplers. The high-frequency region of the spectrum of these noises in the radiation of a superfluorescent fiber source should be weakened in intensity on account of the long lifetime of the working levels of erbium.

The results of this study demonstrate the possibility of raising the sensitivity of fiber-optic gyroscopes[5] by roughly an order of magnitude by using high-power Er/Yb fiber radiation sources and a two-channel scheme of photodetection of the signal.

Thus in this study we have investigated experimentally the intensity noise of a high-power superfluorescent Er/Yb

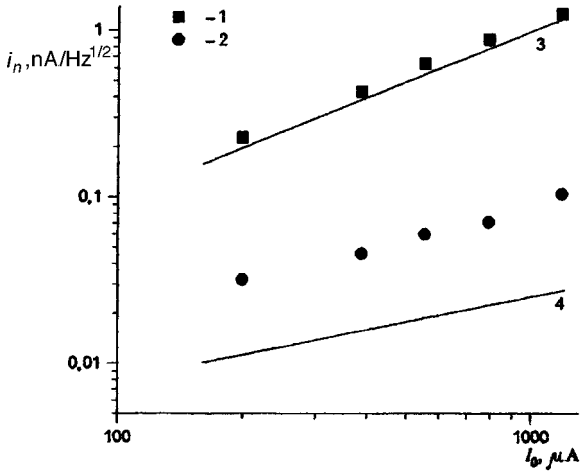

FIG. 2.

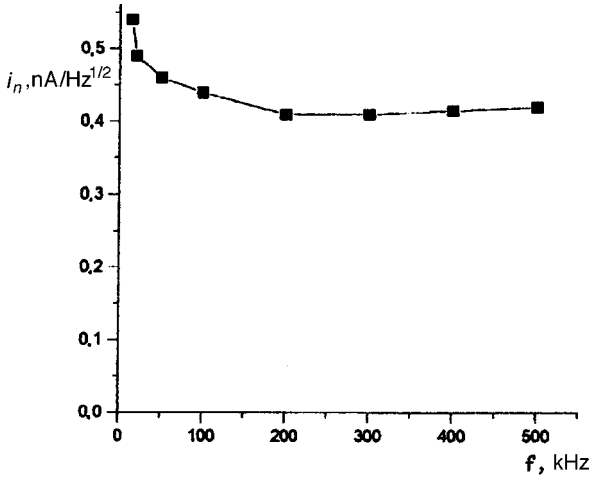

FIG. 3.

fiber source having an all-fiber optical circuit and generating 20 mW in the 1.55 μm region of the spectrum. We have shown that for Fourier frequencies in the region 100–500 kHz the spectral density of the noise is uniform and corresponds to the excess noise of the ''thermal'' sources. In this region the contributions of mode noise of the pump laser diode and of redistribution in the fiber directional couplers are small. It is also shown that the intensity noise of a given source can be compensated (decreased by an order of magnitude) in a two-channel photodetection scheme, to a level close to that of the photon shot noise.

The authors are grateful to V. V. Fomin, V. M. Brylov, and B. G. Ignatov for assistance and helpful discussions.

This study was done with the support of the Russian Fund for Fundamental Research, Grant No. 96-02-18434.

[1] P. F. Wysocki, M. J. F. Digonnet, B. J. Kim, and H. J. Shaw, J. Lightwave Technol. **12**, 550 (1994).
[2] W. K. Burns, R. P. Moeller, and A. Dandridge, IEEE Photonics Technol. Lett. **2**, 606 (1990).
[3] P. R. Morkel, R. I. Laming, H. O. Edwards, and D. N. Payne, *CLEO'90*, Anaheim, Calif. (1990), pp. 154–155.
[4] É. I. Alekseev, E. N. Bazarov, G. A. Gerasimov *et al.*, Pis'ma Zh. Tekh. Fiz. **21**(23), 89 (1995) [Tech. Phys. Lett. **21**, 990 (1995)].
[5] É. I. Alekseev, E. N. Bazarov, G. A. Gerasimov *et al.*, Pis'ma Zh. Tekh. Fiz. **20**(2), 62 (1994) [Tech. Phys. Lett. **20**, 74 (1994)].

Translated by Steve Torstveit

Similarities and differences between the effects of orientation of red blood cells in a nematic liquid-crystal medium and the Fröhlich electrical vibrations

N. V. Kamanina

S. I. Vavilov State Optical Institute All-Russia Science Center, St. Petersburg
(Submitted March 31, 1997; resubmitted September 17, 1997)
Pis'ma Zh. Tekh. Fiz. **23**, 7–15 (December 12, 1997)

A qualitative explanation is given for the effect wherein red blood cells are oriented in a nonlinear liquid-crystal medium, and it is shown that it is different from the Fröhlich interaction for living biological systems. © *1997 American Institute of Physics.* [S1063-7850(97)00212-7]

The unique electro-, magneto-, and thermooptic effects in liquid crystals are now being studied in earnest[1,2] and are finding wide use in coherent-optical information processing schemes,[3,4] laser physics,[5] systems for surface processing and flaw detection,[6] and medicine.[7] The physical phenomena resulting from forces exerted on a liquid-crystal mesophase on account of the electric, magnetic, and thermal fields, deformation, and other causes are due in general to the weak intermolecular interaction of the structural elements of liquid-crystal media.[8]

Another important property of liquid crystals is their orienting ability, which is used in creating composite materials.[9,10] Liquid crystals will orient particles suspended in them and will act as molecular matrices which are easily controlled by an external field. Moreover, because of the interaction between the matrix and the particles suspended in it, the latter become sensitive to the external field, with the result that the orientation of the liquid-crystal matrix also changes.

To take advantage of such factors as the presence of weak dispersion forces between the molecules of liquid crystals and the high orienting ability, we recently proposed a nonlinear liquid-crystal medium for visualizing, fixing, and orienting human red blood cells.[11] Blood reacts to the extremely multifarious processes that are triggered in an organism by various external factors or by a change in the number or activity of the cells circulating in the blood, by the state of the liquid phase, and by the reactivity of these components in relations to the physical factors of the medium. At the present time the configuration of the red blood cells (erythrocytes) is an important indicator of the health of a person,[12] along with the color and hemoglobin concentration of the blood. A healthy human red cell is disk-shaped. A transformation of the erythrocytes can result from energy and immunological imbalances.[12] An elevation of the count of transformed cells is a deleterious factor that can lead to a number of pathological processes in the human organism. A judicious choice of the medium into which the erythrocytes are placed will make it possible to determine rather simply both the number and shape of the cells. Moreover, the possibility of limiting the number of degrees of freedom of the cells (without loss of important vital functions) and to line up a group of test cells along a single direction will substantially simplify the data processing, which presents many difficulties for medical personnel in the the usual biochemical studies.

In this paper we give a qualitative explanation for the orientation of erythrocytes of a healthy organism in liquid-crystal composites with different values of the optical and dielectric anisotropy. Since the parameters mentioned are macroscopic characteristics of the medium and are related to the packing fraction of the liquid crystal molecules, this study will reveal the similarities and differences in the nature of the interaction of erythrocytes with liquid-crystal molecules of different mixtures and will also explore the distinctions between the orientation effect and the Fröhlich forces.

The samples were sandwich cells with dimensions of 25×25 mm and a gap width of 10 μm. A liquid-crystal mixture with a suspension of erythrocytes was drawn into the gap by capillary forces. The erythrocyte concentration was $\sim 5-7\%$ of the total mass of the sample. The erythrocytes were 5–8 μm in diameter. Thus the thickness of the liquid-crystal cell accomodated a single layer of erythrocytes, which simplified the subsequent study of their behavior in the liquid-crystal medium.

All the cells were made with an orienting coating based on a fluoroplastic solution in a mixture of acetone and amyl acetate. The first experiments were done with an admixture of toluene in the orienting coating, but it turned out that this substance caused a greater number of deformed erythrocytes while having no effect on the change in the angle of suspension of the liquid-crystal molecules and the related alignment direction of the erythrocytes. Initially the choice of the organic orienting substance was motivated by the fact that, as had been shown in Refs. 13 and 14, the properties of the orienting film have a substantial influence on the dynamical characteristics of a liquid crystal and largely determine the value of the tilt angle of the liquid-crystal molecules to the substrate surface. Since the highest contrast and fastest response are obtained when polymer orienting coatings are used, the compound indicated above has assuredly been used more often than oxide orienting substances. After the orienting film was obtained by centrifuging, it was rubbed with a flannel cloth, and then used to make *S*-type cells. The flaws created in the rubbing of the orienting film were furrows, to which one can loosely ascribe a sinusoidal relief.

As the initial matrix we use a nematic liquid-crystal composite with different refractive indices Δn and dielectric anisotropies $\Delta\varepsilon$: ZhK-807 ($\Delta n=0.215$, $\Delta\varepsilon>0$); ZhK-1282 ($\Delta n=0.164$, $\Delta\varepsilon=9.9$); ZhK-1289 ($\Delta n=0.168$, $\Delta\varepsilon=10$). For experiments in polarized light a Lyumam-2I microscope with a photographic attachment was used. With the replace-

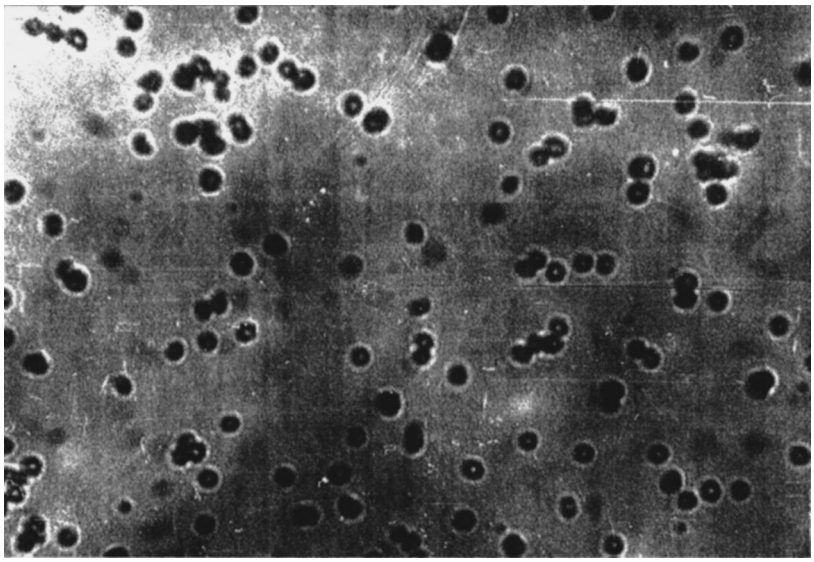

FIG. 1. Pattern of the distribution of erythrocytes in an unoriented liquid-crystal cell. The Fröhlich interaction is manifested for individual erythrocytes.

able objectives it gave magnifications of up to $\times 800$. We studied the erythrocyte distribution pattern in polarized light with the liquid-crystal cell placed between a polarizer and an analyzer set at a 45° angle between them.

Figures 1 and 2 show the results of a study of a uniform distribution of blood cells in an unoriented liquid-crystal cell and in a cell with a rubbed orienting coating. The liquid crystal ZhK-1289 was used as the electrooptic crystal. We recall that photographs of the erythrocyte distribution pattern in the liquid-crystal composite ZhK-1282 were given in Ref. 11. The distribution of the blood cells in an unoriented liquid-crystal medium was shown there as well. It should be said that for all the liquid-crystal mixtures investigated in the present study, as in Ref. 11, the blood cells were found to align along a single preferred direction.

It follows from these studies that erythrocytes, which are not neutral particles,[15] can be oriented along boundaries of rubbing-induced inhomogeneities of the mesophase. Actually, the rubbing of the surface of the orienting film promotes the formation of a geometric microrelief which causes a redistribution of the surface charge arising on electrification. The electric charge is concentrated differently at the hills and valleys of the furrows of the orienting film and creates[4] the potential relief responsible for the packing of the liquid-crystal molecules. These factors can cause displacement of the overlapping regions in associates consisting of two liquid-crystal molecules with overlappimg rigid cores and an antiparallel orientation.[16] The dipole moment of the stretching vibration of the C≡N bond, which is oriented along the long axis of the rigid core of the liquid-crystal molecule, is uncompensated, and the red blood cells are attracted to it and become oriented along boundaries of inhomogeneities of the mezophase.

The general features of the distribution of the red blood cells along a preferred direction are the same for all three of the liquid-crystal media that we studied. However, we did observe differences in the tilt angles of groups of erythrocytes when liquid crystals with different indices Δn and $\Delta\varepsilon$ were used. The difference in the tilt angles of the erythrocytes is due, first, to the difference in the electrophysical

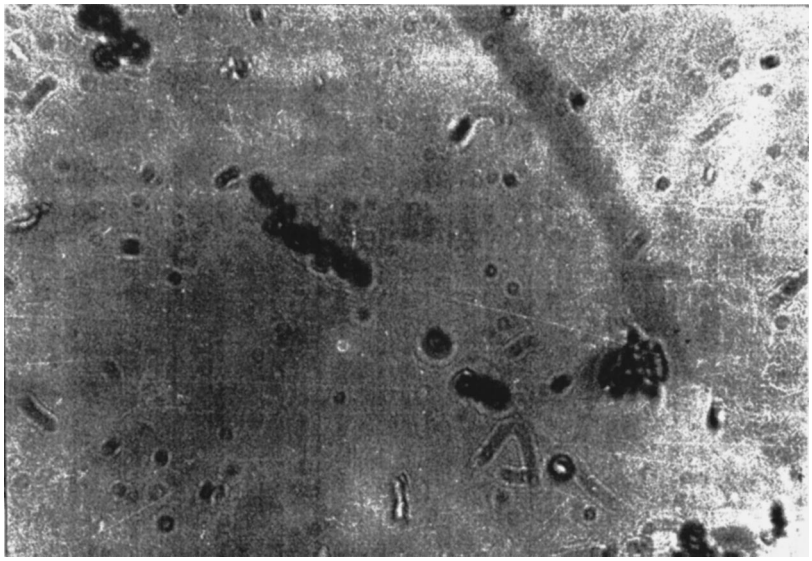

FIG. 2. Manifestation of the orientation of erythrocytes in a liquid-crystal cell with a rubbed polymer orienting coating.

properties of the liquid-crystal mixtures used, and, second, to subtle effects involving the influence of the solid–liquid-crystal interface on the energy of the surface interaction. It is known that the latter is given by the Rapini potential and determines the tilt angle of the liquid-crystal molecules. One of the most successful approximations of the surface free energy density F_s is of the form[9]

$$F_s=(1/2)(W_s \sin^2 \vartheta),$$

where ϑ is the tilt angle of the director of the liquid-crystal molecules with respect to the surface, and W_s is the anchoring energy of the liquid crystal to the surface. In its physical meaning, F_s is equivalent to an interphase surface tension. The values of W_s in the formula for F_s vary over a rather wide range: 10^{-4}–10^{-8} J/m^2 (Ref. 9). The anchoring energy depends on many factors: the nature of the surface, the quality of the rubbing, the aging of the solid surface, and also the properties of the liquid-crystal mixtures used. Under otherwise similar conditions, the liquid-crystal molecules corresponding to different mixtures will lead to different surface densities of uncompensated surface dipoles and to some differences in their orientation direction. Interacting with the liquid-crystal molecules, the erythrocytes follow the relief that has been created and align along a preferred direction with a definite tilt angle.

We note that the alignment of the erythrocytes along a preferred direction is a characteristic feature of their orientation in nonlinear liquid-crystal media, and it is different from the Fröhlich interaction. Fröhlich's theory actually predicts that the blood cells in living blood are attracted to one another because of the presence of a cell membrane potential and electrical vibrations that arise, with a frequency of the order of 10^{11}–10^{12} Hz. For a membrane thickness of 10^{-6} cm and an electrical potential difference of 100 mV a high electric field of the order of 10^5 V/cm is created, which naturally causes the membrane to become highly polarized and effects the organelles of the cell (e.g., proteins). These begin to oscillate at a still higher frequency. The oscillating polar systems can interact with one another, and this interaction is sustained by exchange processes occurring in a living organism. Visually the interacting blood cells begin to coalesce, leading to their subsequent aggregation.

We note that the presence of Fröhlich forces is also detected in our experiments in unoriented liquid-crystal cells. We have observed regions in which there are 3–5 erythrocytes clumped together. However, the subsequent alignment of the erythrocytes along a single direction is a definite indication that another mechanism is in effect, viz., the interaction of the blood cells with the liquid-crystal molecules, which follow the microrelief that is created.

Further, it has been shown[18] that the Fröhlich interaction can be strongly suppressed or eliminated entirely if: 1) the potential of the cell membranes decreases; 2) the store of exchange energy is exhausted. It was shown[18] that when erythrocytes are placed in solutions of suspension with pH=6.3 the membrane potential is close to zero. This substantially reduces the collisions of the erythrocytes and their subsequent coalescence and destroys the cellular organization (it is suppressed by gluteraldehyde, for example). The interaction of the blood cells in suspension can be restored by changing the pH of the solution to 7.6. Thus the authors of Ref. 18 demonstrated the possibility of substantially weakening the Fröhlich interaction by processing erythrocytes in phosphate-buffered silane and the complete disorganization of the cellular structure by processing in gluteraldehyde.

In our experiments the erythrocytes were embalmed in a buffer mixture with pH=7.23–7.25. At these values of the pH a certain slowing of the vital activity of the cellular structures sets in, but the membrane potential is not completely eliminated. The residual potential makes for a charge on the erythrocytes and promotes their subsequent interaction with uncompensated liquid-crystal dipoles. It must be said that in order to decrease the error it would be well to do the experiments with living erythrocytes immediately after the blood is collected from the finger. There are certain difficulties with this, however, since the blood plasma is subject to immunological reactions.[19]

The research reported above and the arguments presented can be summarized as follows:

We have established the similarities and differences in the orientation of erythrocytes in an interaction with liquid-crystal molecules in liquid-crystal composites having different electrooptic properties. We have examined the mechanism of interaction of blood cells with uncompensated liquid-crystal dipoles. We have ascertained the influence of the Fröhlich forces on the formation of microscopic groups of erythrocytes when a suspension of these cells is placed in an uncompensated liquid-crystal medium. We have demonstrated the difference between the orientation of erythrocytes in a nonlinear liquid-crystal medium as compared to the onset of Fröhloch's electrical vibrations for living biological systems. We have selected a medium which is rather favorable for studying blood cells: it does not cause total loss of the important vital functions of the cells, and the residual membrane potential ensures an interaction of the erythrocytes with the liquid-crystal molecules and their alignment in a row at a certain angle to the surface of the substrate.

This last circumstance is of great significance from an applied standpoint. Comparison testing of a blood sample from a healthy organism against some pathology by means of a correlation type of information processing (the Van der Lugt correlation function and a joint transformation) encounters difficulties if the blood cells are rotated. Optical systems of this kind are not invariant with respect to rotation of the cells in the blood sample. The chosen medium, which limits the number of degrees of freedom of the blood cells (on account of the viscosity of the liquid crystals) and aligns them at the same angle to a common direction (on account of the orienting ability of the liquid crystals), substantially simplifies the correlation analysis. Furthermore, when the blood cells are aligned in a row they can be easily tested for shape, providing information to medical personnel about the severity of certain illnesses. In addition, it is easier to count the blood cells with the aid of an oriented liquid-crystal cell as compared to the quantitative estimate obtained in a Goryaev chamber, and such cells may find application in ordinary laboratory studies of blood smears.

The author thanks I. E. Morichev for the opportunity of discussing the results and V. N. Kidalov for assistance in this study.

The author is grateful to the Organizing and Scientific Committees of the European Conference on Liquid Crystals (ECLC'97, March 3–8, Zakopane, Poland) for providing a conference grant which made it possible to present research material in an international forum, and also to the Russian Fund for Fundamental Research for Travel Grant No. 97-02-26601.

[1] P. G. de Gennes, *The Physics of Liquid Crystals*, Oxford University Press (1974).
[2] S. M. Arekelyan and Yu. S. Chilingaryan, *Nonlinear Optics of Liquid Crystals* [in Russian], Nauka, Moscow (1984).
[3] A. A. Vasil'ev, D. Kasasent, I. N. Kompanets, and A. V. Parfenov, *Spatial Light Modulators*, Radio i Svyaz', Moscow (1987).
[4] N. V. Kamanina, L. N. Soms, and A. A. Tarasov, Opt. Spektrosk. **68**, 691 (1990) [Opt. Spectrosc. **68**, 403 (1990)].
[5] V. V. Danilov, Opt. Zh., No. 7, pp. 8–19 (1993).
[6] M. G. Tomilin, Mol. Cryst. Liq. Cryst. **193**, 7 (1990).
[7] A. Adamchik and Z. Strugal'skiĭ, *Liquid Crystals* [Russian transl. from Polish], Sov. Radio, Moscow (1979).
[8] G. R. Luckhurst and G. W. Gray (Eds.), *The Molecular Physics of Liquid Crystals*, Academic Press, New York (1979).
[9] G. M. Zharkova and A. S. Sonin, *Liquid-Crystal Composites* [in Russian], VO ''Nauka'', Novosibirsk (1994).
[10] R. Yamaguchi and S. Sato, Jpn. J. Appl. Phys., Part 2 **31(3a)**, L254 (1992).
[11] N. V. Kamanina and V. N. Kidalov, Pis'ma Zh. Tekh. Fiz. **22**(14), 39 (1996) [Tech. Phys. Lett. **22**, 571 (1996)].
[12] V. N. Kidalov and V. F. Lysak, Lab. Delo. Meditsina, No. 8, pp. 36–40 (1989).
[13] D. W. Berreman, J. Opt. Soc. Am. **62**, 502 (1972).
[14] N. V. Kamanina and N. A. Vasilenko, Proc. Soc. Photo-Opt. Instrum. Eng. (SPIE) **2731**, 220 (1995).
[15] V. V. Ignat'ev, V. N. Kidalov, V. O. Samoĭlov *et al.*, Fiziol. Zh. I. M. Sechenova, No. 12, pp. 115–120 (1995).
[16] E. M. Aver'yanov, V. A. Zhuĭkov, V. F. Shabanov, and P. V. Adomenas, Kristallografiya **27**, 333 (1982) [Sov. Phys. Crystallogr. **27**, 201 (1982)].
[17] H. Fröhlich, IEEE Trans. Microwave Theory Tech. **MTT-26**, 613 (1978).
[18] S. Rowlands, L. S. Sewchand, and E. G. Enns, Phys. Lett. A **87**, 256 (1982).
[19] V. A. Levtov, S. A. Regirer, and N. Kh. Shadrina, *Rheology of Blood* [in Russian], Meditsina, Moscow (1992).

Translated by Steve Torstveit

Magnetoplasmon modes in the response of a mesoscopic particle of a semimetal or a nonmagnetic insulator

S. I. Bastrukov and D. V. Podgaĭnyĭ

Joint Institute for Nuclear Research, Dubna
(Submitted November 20, 1996)
Pis'ma Zh. Tekh. Fiz. **23**, 16–21 (December 12, 1997)

The macroscopic features of the behavior of a mesoscopic particle in a magnetic field are investigated for mesoscopic particles possessing the properties of a semimetal or a nonmagnetic insulator. It is shown that for a fixed value of the magnetic field the frequency of the Alfvén magnetoplasma mode falls off monotonically (as $1/R$) as the radius of the particle increases.
 [S1063-7850(97)00312-1]

The significant progress that has been achieved toward miniaturization of computer technology continues to provide the main stimulus for the intensive research on the mesoscopic properties of micron samples and nanoparticles of conducting materials.[1] A feature of mesoscopic particles is that they are polyatomic systems whose stability of formation is conditional on the organization of the charge carriers in the shell and depends substantially on the parity of the number of atoms forming them (the binding energy is determined by the shell and even–even effects which are characteristic for microscopic systems such as atoms and atomic nuclei). At the same time, in the response of a mesoscopic particle to an external electromagnetic perturbation one can discern the completely macroscopic behavior of the charge carriers that is characteristic of solids of infinite volume. The only mesoscopic objects that have been well studied at present are atomic clusters of alkali metals, the charge carriers in which are electrons (see, e.g., Refs. 2 and 3 and the references cited therein). Meanwhile, the mesoscopic properties of fine particulates of other conducting materials, such as semimetals, remain less well studied.

A distinctive physical property of semimetals (bismuth, antimony, tungsten) cooled to liquid-helium temperatures (below 2 K) and immersed in a uniform magnetic field is their ability to support the propagation of transverse low-frequency oscillations,[4–8] which are known in magnetohydrodynamics as Alfvén waves[9,10] and which are characterized by dispersionless propagation:

$$\omega = c_A k, \quad c_A = V_A \cos\theta, \quad V_A = B/(4\pi\rho)^{1/2}, \tag{1}$$

where $\rho = n(m_e^* + m_h^*)$ is the mass density of the neutralized electron–hole plasma (m_e^* and m_h^* are the effective masses of the electron and hole), and θ is the angle between the propagation direction (wave vector $\mathbf{k}$) of the wave and the direction of the magnetic field $\mathbf{B}$. Alfvén waves can also be excited in nonmagnetic semiconductors.[11,12] This macroscopic property is a consequence of the microscopic mechanism of conduction of a semimetal or a nonmagnetic insulator, the carriers of which, unlike the case of simple metals, are electrons and holes with equal densities $n = n_e = n_h$. It is appropriate to mention here that the equality of the electron and hole densities n_e and n_h is what makes it impossible for helical magnetoplasma waves (helicons) to propagate in the aforementioned materials.[6–8]

In this report we discuss the macroscopic features of the behavior of a mesoscopic particle in a magnetic field for mesoscopic particles possessing the properties of a semimetal or nonmagnetic insulator. The goal of our analysis is to determine the mesoscopic size effect in the response of such a particle to an external electromagnetic perturbation, the physical nature of which is due to the excitation of natural oscillations of the Alfvén type in a neutralized and magnetized solid-state (electron–hole) plasma. From a constructive standpoint the problem consists in obtaining the explicit dependence of the frequency of the Alfvén modes on the dimensions of the sample in order to assess how the dispersion relation (1) (the law of propagation of Alfvén waves in an infinite volume of a semimetal or nonmagnetic insulator) is modified in going to mesoscopic samples of these materials.

The magnetoplasma response of a mesoscopic particle can be analyzed in the model of a magnetized and neutralized solid-state plasma, the motion of which is governed by the equations of magnetohydrodynamics:[9,10]

$$\frac{d\rho}{dt} + \rho\nabla\cdot\mathbf{V} = 0, \quad \rho\frac{d\mathbf{V}}{dt} = -\nabla W + \frac{1}{4\pi}(\mathbf{B}\cdot\nabla)\mathbf{B},$$

$$\nabla\cdot\mathbf{B} = 0, \quad \frac{\partial\mathbf{B}}{\partial t} = \nabla\times(\mathbf{V}\times\mathbf{B}), \tag{2}$$

where $d/dt = \partial/\partial t + (\mathbf{V}\cdot\nabla)$ is the substantive derivative, $\mathbf{V}$ is the velocity of the collective flow of the electron–hole plasma, $\mathbf{B}$ is the uniform magnetic induction inside the sample, and W is the hydromagnetic pressure. If it is assumed that the external perturbation does not give rise to local fluctuations of the density ($\delta\rho = 0$) or of the hydromagnetic pressure ($\delta\mathbf{W} = 0$), the linearized equations of magnetohydrodynamics, which admit the possibility of Alfvén wave propagation in the electron–hole plasma, take the form:[10]

$$\rho\frac{\partial\delta\mathbf{V}}{\partial t} - \frac{1}{4\pi}(\mathbf{B}\cdot\nabla)\delta\mathbf{B} = 0, \quad \nabla\cdot\delta\mathbf{B} = 0, \quad \nabla\cdot\delta\mathbf{V} = 0, \tag{3}$$

$$\frac{\partial\delta\mathbf{B}}{\partial t} - (\mathbf{B}\cdot\nabla)\delta\mathbf{V} = 0. \tag{4}$$

Here $\delta\mathbf{V}$ and $\delta\mathbf{B}$ are variations of the velocity and magnetic field, respectively, due to the external perturbation, and ρ is

understood to mean the equilibrium density of charge carriers. Scalar multiplication of Eq. (4) by $\delta\mathbf{V}$ and integration over the volume of the particle (here it is assumed that $\delta\mathbf{B}|_{r=R}=0$ on the surface of the particle) leads to the energy balance equation

$$\frac{\partial}{\partial t}\int_V \frac{\rho\delta V^2}{2}d\tau=\frac{1}{4\pi}\int_V \delta V_i B_k \frac{\partial \delta B_i}{\partial x_k}d\tau. \tag{5}$$

The variations of the flow velocity and magnetic induction are conveniently written in the form

$$\delta\mathbf{V}=\boldsymbol{\xi}(\mathbf{r})\dot{\alpha}(t), \quad \delta\mathbf{B}=\mathbf{b}(\mathbf{r})\alpha(t), \tag{6}$$

where $\xi(\mathbf{r})$ is the field of the instantaneous displacements and $\mathbf{b}(\mathbf{r})=(\mathbf{B}\cdot\nabla)\xi(\mathbf{r})$. The latter relation follows from Eq. (5) after $\delta\mathbf{B}$ given by relation (6) is substituted into it. Now substituting (6) into (4), the latter equation is transformed into an equation of normal oscillations:

$$M\ddot{\alpha}+K\alpha=0, \tag{7}$$

where M is the inertia and K is the stiffness of the Alfvén oscillations:

$$M=\int_V \rho\xi^2(\mathbf{r})d\tau, \quad \xi^2(\mathbf{r})=\xi_i(\mathbf{r})\xi_i(\mathbf{r}), \tag{8}$$

$$K=\frac{1}{4\pi}\int_V b^2(\mathbf{r})d\tau, \quad b^2(\mathbf{r})=B_k\frac{\partial\xi_i(\mathbf{r})}{\partial x_k}B_n\frac{\partial\xi_i(\mathbf{r})}{\partial x_n}. \tag{9}$$

It follows from the expressions obtained for M and K that in order to determine the natural frequencies of the Alfvén magnetoplasma modes one needs to know only the field of the instantaneous displacements $\xi(\mathbf{r})$, which is uniquely related by Eq. (6) to the variations of the velocity field $\delta\mathbf{V}(\mathbf{r},t)$.

From a physical standpoint the presence of a static magnetic field inside the magnetization is ordinarily treated as a background (magnetic jellium), the presence of which is responsible for its elastodynamic (elastic-like) behavior, in the sense that the ability of a continuous medium to support undamped transverse oscillations as well as longitudinal ones is a property inherent to an ideally elastic continuum. This similarity in the behavior of a magnetized plasma and an elastic medium gives us grounds for assuming that the displacement fields accompanying the natural Alfvén oscillations of an electron–hole plasma magnetized in a spherical volume can be described by the displacement fields arising in a spherical particle of an ideally elastic medium with elastic oscillations excited in it. On the basis of this observation, we use the solutions found in Ref. 13 for the equations of elastodynamics of a poloidal displacement field

$$\xi_p(r)=\frac{N_p}{l+1}(\nabla\times(\nabla\times\mathbf{r}))r^l P_l(\mu)=N_p\nabla r^l P_l(\mu),$$

$$N_p=1/(lR^{l-2}), \tag{10}$$

accompanying the spheroidal elastodynamic oscillations of a spherical particle, and also for the toroidal displacement field

$$\boldsymbol{\xi}_t(\mathbf{r})=N_t(\nabla\times\mathbf{r})r^l P_l(\mu), \quad N_t=1/(R^{l-1}), \tag{11}$$

arising in the torsional oscillations of a spherical particle of an elastic medium. Here $P_l(\mu)$ is a Legendre polynomial of multipole order l, and $\mu=\cos\theta$. The analogy discussed above explains the physical origin of the magnetoelastic restoring force in the Alfvén oscillations of an electron–hole plasma magnetized in a spherical volume: the collective displacements of the charge carriers under the influence of the external perturbation deforms the equilibrium magnetic field, giving rise to a stress which tends to restore the equilibrium configuration of the magnetic field.

To obtain concrete estimates we consider the case in which the external uniform magnetic field penetrating into the particle is directed along the x axis: $\mathbf{B}=(B,0,0)$. In a spherical coordinate system with a fixed polar axis, the components of this field inside the particle are of the form

$$B_r=(1-\mu^2)^{1/2}B\cos\phi, \quad B_\theta=\mu B\cos\phi,$$

$$B_\phi=B\sin\phi, \tag{12}$$

where $\mu=\cos\theta$. Substituting expressions (10), (11), and (12) into (8) and (9), we find that the frequencies $\omega^2=K/M$ (details of the calculations of the coefficients M and K are given in Ref. 14) of the natural poloidal and toroidal oscillations are given by

$$\omega_p^2=\frac{1}{2}\omega_A^2(l-1)^2\frac{2l+1}{2l-1}, \quad \omega_t^2=\frac{1}{2}\omega_A^2\frac{(l^3+1)}{l+1}\frac{2l+3}{2l-1}, \tag{13}$$

respectively, where

$$\omega_A^2=\frac{V_A^2}{R^2}=\frac{B^2}{4\pi\rho R^2} \tag{14}$$

is the fundamental, Alfvén frequency of the magnetoplasmon mode.

The spectral formulas (13) and (14) are the main result coming from the magnetic jellium model and express the physical content of the mesoscopic size effect that is expected in the response of a spherical particle of a semimetal or nonmagnetic insulator: at a fixed value of the field strength the frequency of the Alfvén magnetoplasmon mode falls off monotonically with increasing particle radius as $1/R$. This conclusion can serve as one of the main guideposts in the experimental search for the mesoscopic effect described here.

Let us conclude by given some concrete numerical estimates of the frequency of the magnetoplasmon mode for bismuth particles of micron size and smaller. The velocity of an Alfvén wave in bismuth cooled to $T=1.2$ K is $V_A\approx 10^9$ cm/s. Substituting this value into Eq. (13) and assuming that $R\sim 10^{-2}-10^{-4}$ cm, we find that the frequencies of the Alfvén oscillations lie in the interval $10^{11}-10^{13}$ Hz, which is completely accessible to measurement. This holds forth the hope that the above predictions can be checked in the near future.

This study was supported by INTAS under Grant INTAS-151.

[1] F. A. Buot, Phys. Rep. **234**, No. 2/3, pp. 73–174 (1993).
[2] G. F. Bertsch and R. A. Broglia, *Oscillations in Finite Quantum Systems*, Cambridge University Press, Cambridge (1994).
[3] S. I. Bastrukov, J. Mosc. Phys. Soc. **4**, 57 (1994).
[4] S. J. Buchsbaum and J. K. Galt, Phys. Fluids **4**, 1514 (1961).
[5] G. A. Williams, Phys. Rev. A **139**, A771 (1965).
[6] É. A. Kaner and V. G. Skobov, Usp. Fiz. Nauk **89**, 368 (1966) [*sic*] Adv. Phys. **17**, 605 (1968).
[7] P. M. Platzman and P. A. Wolf, *Waves and Interactions in Solid State Plasmas*, Academic Press, New York (1973) [Mir, Moscow (1973)].
[8] A. A. Abrikosov, *Principles of the Theory of Metals* [in Russian], Nauka, Moscow (1987).
[9] L. D. Landau and E. M. Lifshitz, *Electrodynamics of Continuous Media*, 2nd ed. (revised and enlarged, with L. P. Pitaevskii), Pergamon Press, Oxford (1984) [cited Russian original, Nauka, Moscow (1992)].
[10] S. Chandrasekhar, *Hydrodynamic and Hydromagnetic Stability*, Clarendon Press, Oxford (1961).
[11] A. C. Baynham and A. D. Boardman, Adv. Phys. **19**, 575 (1970).
[12] Yu. K. Pozhela, *Plasmas and Current Instabilities in Semiconductors* [in Russian], Nauka, Moscow (1977).
[13] S. I. Bastrukov, Phys. Rev. E **49**, 3166 (1994).
[14] S. I. Bastrukov and D. V. Podgainy, Phys. Rev. E **54**, 4465 (1996).

Translated by Steve Torstveit

Nonequilibrium surface ionization of water molecules in a high electric field in the presence of resonance absorption of near-infrared radiation

N. M. Blashenkov and G. Ya. Lavrent'ev

A. F. Ioffe Physicotechnical Institute, Russian Academy of Sciences, St. Petersburg
(Submitted June 27, 1997)
Pis'ma Zh. Tekh. Fiz. **23**, 22–25 (December 12, 1997)

The results of experiments undertaken to establish the connection between the current of ions desorbed from the surface in the presence of an electric field and the frequency of the infrared radiation incident on that surface are described. It is shown that resonance absorption of infrared radiation by adsorbed molecules increases the efficiency of the surface ionization process. © *1997 American Institute of Physics.* [S1063-7850(97)00412-6]

The phenomenon of nonequilibrium surface ionization was discovered in a study of the ionization of the products of the heterogeneous exothermic reaction of dissociation of acetone peroxide.[1] The measured values of the ion currents of the radicals formed in this reaction exceeded the equilibrium values of the currents calculated for them according to the theory of surface ionization by 6–7 orders of magnitude. As was shown in Ref. 2, such a strong increase in the ion current can be accounted for by vibrational excitation of the desorbing ions on account of the energy released in the course of the exothermic chemical reaction.

Consequently, upon the excitation of vibrational states of adsorbed molecules by infrared radiation the efficiency of nonequilibrium surface ionization of excited particles should increase. However, at the low emitter temperatures necessary for the formation of appreciable coatings, the lifetime of the adsorbate (τ^0 for neutrals and τ^+ for ions) can be much longer than the relaxation time τ^* of vibrational excitation on the surface. In order for the particles to have time to be desorbed while in excited states, it is necessary to decrease their lifetime on the surface. The lifetime of neutral particles cannot be changed under the given conditions. Unlike that of neutrals, however, the lifetime of ions formed from excited molecules by the nonequilibrium surface ionization mechanism can be decreased by lowering the Schottky barrier by applying an electric field to the surface, so that $\tau^+ < \tau^*$ (Ref. 3).

Thus in this paper we address the problem of establishing the relation between the current of ions desorbed from the surface in the presence of a high electric field and the variable frequency of the infrared radiation incident on the surface in the spectral region of the normal modes of the adsorbed molecules.

The adsorbate consisted of water molecules which had been admitted to a level of $\sim 10^{-6}$ torr into the surface-ionization field ion source of a static magnetic mass spectrometer, with a residual gas pressure of 10^{-9} torr. The ion emitter was an oxidized tungsten filament 5–10 μm in diameter. A voltage $U = -(0.5–20)$ kV was applied to an electrode coaxial with the tungsten emitter, producing an electric field at the emitter of 10^5 to 8×10^6 V/cm in the case of a smooth filament and up to 10^8 V/cm as the tungsten oxide scale grew on the filament.[4] The emitter was illuminated by monochromatic light with a wavelength varying from 1.6 to 2 μm from the MDR-23 monochromator of a KSVU-23 apparatus. The temperature of the emitter in the experiments was 350–400 K. The ions were detected in the pulse-counting mode. The spectrum was recorded in a sweep of the wavelength along the abscissa with a step of 20 nm, while the signal from the secondary electron multiplier of the mass spectrometer was applied to the ordinate axis through the computer of the KSVU-23 apparatus. In each run we first made a background scan (without the emitter illumination) and then a scan with the emitter illuminated. The working scan was the difference of the first and second scans. The statistics of the resulting spectrum amounts to 66 working scans.

Figure 1 shows the spectrum of the ion current for H_2O^+ ($m/e = 18$ u) as the wavelength of the illumination was swept from 1.6 to 2 μm. An excess of the current above the rms deviation is observed for $\lambda = 1.91–1.95$ μm. The closest eigenfrequencies of the water molecule to these wavelengths are the combination frequencies $(\nu_1 + \nu_2)^{-1} = 1.91$ μm and $(\nu_3 + \nu_2)^{-1} = 1.88$ μm (besides these frequencies this range also includes the fourth overtone $(4\nu_2)^{-1} = 1.63$ μm, but its excitation probability is very low). Here we have used the notation for parallel normal modes: skeletal $(\nu_1)^{-1} = 2.73$ μm, deformation $(\nu_2)^{-1} = 6.27$ μm, and for the perpendicular skeletal mode $(\nu_3)^{-1} = 2.66$ μm (Ref. 5).

Vibrations at the combination frequency $(\nu_3 + \nu_2)$ and at the fundamental frequency ν_3 are not excited on the surface if the symmetry axis of the adsorbed water molecules is perpendicular to the surface (this is the most probable position of the molecules, particularly in an electric field). The dipoles which vary parallel to the surface are not excited, since the corresponding component of the radiation incident on the metal surface is zero.[6] And this is precisely how the dipoles should vary in the perpendicular vibrations ν_3 for the orientation of the molecules described above.

It follows from what we have said that the observed band can be attributed to vibrations at the combination frequency $(\nu_1 + \nu_2)$. The width of the band in our spectrum is ~ 100 cm^{-1}, which agrees with the width of the band of an individual molecule. This means that the adsorbed molecules in our case are not bound by hydrogen bonds, i.e., they do

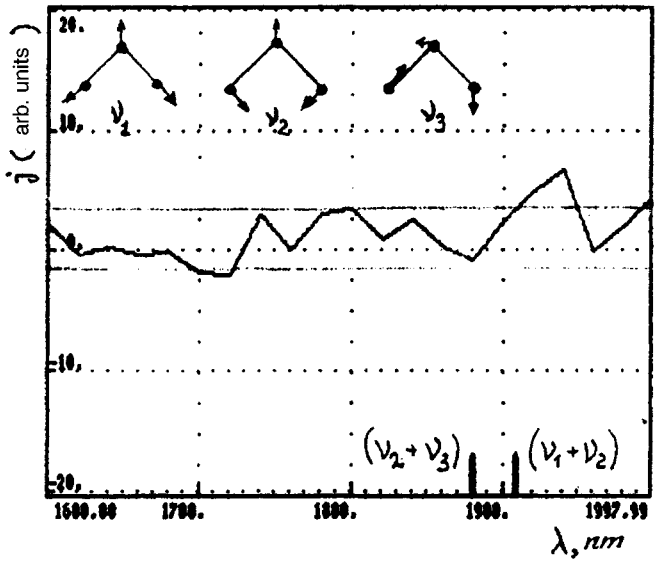

FIG. 1. Current j of desorbed H_2O^+ ions versus the wavelength λ of the radiation incident on the surface. The horizontal lines indicate the rms error. Top: the displacements of the atoms in the normal modes of the H_2O molecule. Bottom: the position of the combination frequencies along the abscissa.

not form a water film on the surface.[7] The shift of the absorption band to longer wavelengths by $\sim 130\ \mathrm{cm}^{-1}$ is indicative of the presence of a chemical shift which overlaps the dipole interaction of the adsorbed molecules.[6]

Thus the experiments confirm the hypothesis that the resonance absorption of infrared radiation by adsorbed molecules enhances the efficiency of surface ionization by the mechanism of nonequilibrium surface ionization. This, we believe, opens up prospects for new techniques of photodesorption infrared spectrometry for adsorption systems.

In closing we express our sincere gratitude to M. V. Knat'ko, V. I. Paleev, and N. D. Potekhina for helpful discussions.

[1] I. N. Bakulina, N. M. Blashenkov, G. Ya. Lavrent'ev, V. I. Paleev, and B. N. Shustrov, Pis'ma Zh. Tekh. Fiz. **1**, 170 (1975) [Tech. Phys. Lett. **1**, 81 (1975)].
[2] N. M. Blashenkov and G. Ya. Lavrent'ev, Pis'ma Zh. Tekh. Fiz. **14**, 1359 (1988) [Tech. Phys. Lett. **14**, 593 (1988)].
[3] N. M. Blashenkov and G. Ya. Lavrent'ev, Pis'ma Zh. Tekh. Fiz. **21**(24), 15 (1995) [Tech. Phys. Lett. **21**, 1000 (1995)].
[4] H. D. Beckey, *Principles of Field Ionization and Field Desorption Mass Spectrometry*, Pergamon Press, New York (1977), Vol. 61, p. 335.
[5] L. A. Gribov, *Introduction to Molecular Spectroscopy* [in Russian], Nauka, Moscow (1976).
[6] *Vibrational Spectroscopy of Adsorbates. Collected Works* [in Russian], Mir, Moscow (1984).
[7] Ya. S. Bobovich, Usp. Fiz. Nauk **162**(6), 81 (1992) [Sov. Phys. Usp. **35**, 481 (1992)].

Translated by Steve Torstveit

Using C_{60} molecules for deep carbonization of rhenium in ultrahigh vacuum

R. N. Gall', E. V. Rut'kov, A. Ya. Tontegode, and M. M. Usufov

A. F. Ioffe Physicotechnical Institute, Russian Academy of Sciences, St. Petersburg
(Submitted May 29, 1997)
Pis'ma Zh. Tekh. Fiz. **23**, 26–30 (December 12, 1997)

The adsorption of C_{60} molecules on the surface of a rhenium ribbon heated to 1800 K is investigated quantitatively. It is found that the C_{60} molecules are adsorbed without reflection and then dissociate, and the carbon formed in the process is dissolved in the bulk of the rhenium to the limit of solubility. Then a graphite monolayer forms on the rhenium surface, and the dissociation of the C_{60} molecules stops. It is shown that the C_{60} molecules can be used as an effective carbonizing object on metals in ultrahigh vacuum. © *1997 American Institute of Physics.* [S1063-7850(97)00512-0]

Among the various allotropic forms of carbon the C_{60} molecule has a distinctly low sublimation temperature and is extremely promising for use as an ultrahigh-vacuum carbonizing agent. In carbonization by C_{60} there are no extraneous atoms impinging on the surface as, for example, when hydrocarbons or CO molecules are used as the carbonizing agent. This purity is very important both in scientific experiments such as research on the properties of catalysts and on the mechanisms and prevention of corrosion, and also in technological applications, e.g., in metallurgy, in the growth of diamond films.

Unfortunately, there is extremely little information in the literature concerning the interaction of fullerene molecules such as C_{60} with the surfaces of metals at high temperatures. For example, it has been shown[1–4] that C_{60} molecules adsorbed on the surface of Ir or Re at room temperature retain their nature, and on heating to $T=800-1000$ K they dissociate on the surface of both these metals. The carbon that is liberated ''forgets'' how it got to the surface and behaves precisely as we have found previously for other sources of carbonization—it forms a graphite film on the surface of Ir (Ref. 5) and dissolves in the bulk in Re (Ref. 6). At the same time, it is not known whether adsorption at elevated temperatures, in particular, at the temperatures required for carbonization processes (1000–1600 K), leads to dissociation of the C_{60} molecules and the accumulation of carbon on the surface and in the bulk of the substrate or to reflection of the C_{60} molecules from the surface.

EXPERIMENTAL RESULTS

The experiments were done in the ultrahigh-vacuum ($p<10^{-10}$ Torr), high-resolution Auger spectrometer described in Ref. 7. The samples were rhenium ribbons with dimensions of $0.02\times1\times40$ mm, which were heated by the direct passage of an ac electrical current through them. An auxiliary Mo ribbon with dimensions of $0.02\times1\times40$ mm was used in some of the measurements. The temperature of the ribbons was measured by an optical micropyrometer.

Molecules of C_{60} were deposited on the surface of the rhenium ribbon, which was held at a temperature of 1800 K, from a Knudsen cell located ~3 mm from the surface of the ribbon, and the state of the adlayer was monitored by measuring the thermionic emission current by means of a special collector system with an antidynatron grid.[7] At no time during the experiment did the residual pressure in the apparatus exceed 1×10^{-9} Torr. The results are presented in Fig. 1. It was found that during the first ten minutes of deposition the emission current was almost constant, but a slight increase of the current (by ~20%) and growth of the resistance of the ribbon indicated that the carbon placed on the surface is actively dissolved in the bulk of the metal. At the twelfth minute of deposition the current increased sharply by two orders of magnitude and then stabilized, and the further deposition of fullerenes did not lead to any changes in the system.

The processes occurring here are similar to those which we observed previously in the carbonization of a rhenium ribbon in benzene vapor.[6] When the concentration of the carbon dissolved in the ribbon reached a level corresponding to the solubility limit, a graphite monolayer formed on the surface, blocking the further dissociation of the fullerene molecules. The work function of a graphite monolayer, $e\varphi=4.45$ eV, is significantly below that of rhenium coated with a surface carbide, $e\varphi=5.25$ eV, and this makes for a sharp increase in the thermionic emission current upon the formation of the graphite monolayer.

To confirm the physical picture developed above, the rhenium ribbon was heated to temperatures corresponding to the active desorption of carbon (2200–2300 K), and the desorption products, which were condensed on another, auxiliary molybdenum ribbon, were studied by Auger electron spectroscopy. It was found that carbon indeed does accumulate in the bulk of the rhenium ribbon, and on heating is desorbed in significant quantities (5–6 monolayers of carbon on an auxiliary ribbon located ~15 mm from the rhenium sample), while no extraneous impurities were detected among the desorption products.

To determine the total number of C_{60} molecules that have fallen on the surface of the rhenium ribbon in the carbonization process, we had to determine the flux density of the fullerene molecules emitted by the Knudsen cell. For this the flux of C_{60} molecules from the cell was directed onto the surface of an auxiliary Mo ribbon held at room temperature, and the number of adsorbed molecules was determined by Auger electron spectroscopy. As was shown in Refs. 2 and 3,

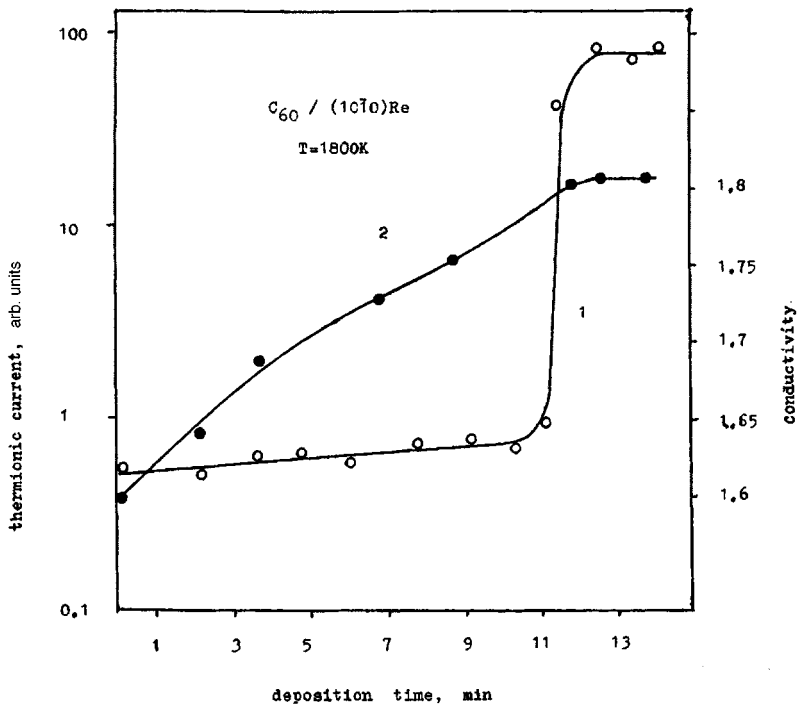

FIG. 1. Change in the thermionic current (*1*) and electrical resistance (*2*) of a rhenium ribbon as a constant flux of C_{60} molecules impinges on its surface. The ribbon is at a temperature $T=1800$ K.

for such measurements it is preferable to use not the growth of the carbon Auger signal but the screening of the Auger signal of the substrate (the intensity of the Mo Auger signal at $E=221$ eV). We also used a technique proposed in those papers[2,3] for estimating the concentration of C_{60} molecules in the adlayer.

According to the results of the measurements the flux density of C_{60} molecules from the cell, located ~ 22 mm from the surface of the auxiliary ribbon (it was not possible to place it any closer to the cell), was $\sim(2\pm 0.3)\times 10^{12}$ mol/cm^2 s. Assuming for our estimates that the emitted flux density falls off with distance as $\sim R^{-2}$, we can calculate the flux impinging on the surface of the rhenium ribbon; as we see, this density turns out to be $(22/3)^2\cdot 2\times 10^{12}$ mol/cm^2 s$=1.0\times 10^{14}$ mol/cm^2 s. Since each molecule contains 60 carbon atoms, the flux density of carbon to the surface is $\sim 6\times 10^{15}$ atoms C/cm^2. Let us now estimate the total amount of carbon dissolved in the ribbon. The solubility limit of carbon at the temperatures used is ~ 3 at.% (Ref. 8), the volume associated with each square centimeter of the surface for a ribbon 0.02 mm thick is 2×10^{-3} cm^3, and the density of rhenium atoms in the metal is 6.8×10^{22} atoms/cm^3 (Ref. 9). Then the limiting amount of carbon dissolved per square centimeter of ribbon is $2\times 10^{-3}\cdot(2-3)\times 10^{-2}\cdot 6.8\times 10^{22}=(3-4)\times 10^{18}$ atoms C/cm^2. At the same time, in the 12 minutes that it took for the carbonization to occur the number of carbon atoms impinging on the surface of the metal was $12\cdot 60\cdot 6\times 10^{15}$ atoms C/cm$^2=4\times 10^{18}$ atoms C/cm^2, which is very close to the limiting value estimated above. Even this rough estimate is convincing evidence that the fraction of the molecules that does not undergo dissociation on the surface in the high-temperature adsorption of C_{60} molecules is small and that these molecules are indeed not reflected from the surface but disassociate on it, making them a highly efficient carbonizing agent.

The authors are grateful to the Russian Government Program ''Fullerenes and Atomic Clusters'' for support of this study (Project No. 96134 ''Surface'') and to the KADIKS(R) company of St. Petersburg for furnishing equipment manufactured by them for the experiments.

[1] E. V. Rut'kov, A. Ya. Tontegode, and Yu. S. Grushko, JETP Lett. **57**, 724 (1993).
[2] N. R. Gall, E. V. Rut'kov, A. Ya. Tontegode, and M. M. Usufov, Mol. Mater. **7**, 187 (1996).
[3] E. V. Rut'kov, A. Ya. Tontegode, and M. M. Usufov, Phys. Rev. Lett. **74**, 758 (1995).
[4] E. V. Rut'kov, A. Ya. Tontegode, M. M. Usufov, and Yu. S. Grushko, in *Proceedings of the International Workshop on Fullerenes and Atomic Clusters*, Foundation for Intellectual Collaboration, St. Petersburg (1993), p. 92.
[5] N. A. Kholin, E. V. Rut'kov, and A. Ya. Tontegode, Surf. Sci. **139**, 155 (1984).
[6] N. R. Gall, S. N. Mikhailov, E. V. Rut'kov, and A. Ya. Tontegode, Surf. Sci. **191**, 185. (1987).
[7] E. Ya. Zandberg and N. I. Ionov, *Surface Ionization*, Israel Program for Scientific Translations, Jerusalem (1971), p. 54.
[8] E. E. Fromm and E. Gebhart, *Gase und Kohlenstoff in Metallen*, Springer-Verlag, Berlin (1976), p. 350.
[9] C. Kittel, *Introduction to Solid State Physics*, 5th ed., Wiley, New York (1976) [Nauka, Moscow (1978), p. 55].

Translated by Steve Torstveit

Shift of the emission lines of aluminum in a laser plasma generated on the surface of a solid target in the atmosphere

O. A. Bukin, E. N. Bol'shakova, É. A. Sviridenkov, N. V. Sushilov, A. Yu. Maĭor, and O. I. Kholodkevich

Pacific Oceanological Institute, Far Eastern Branch of the Russian Academy of Sciences, Vladivostok
(Submitted October 29, 1996; resubmitted April 1, 1997)
Pis'ma Zh. Tekh. Fiz. **23**, 31–35 (December 12, 1997)

Experiments designed to elucidate how the emission lines of the elements of a laser plasma are affected by the presence of the atmosphere are described. It is shown that the generation of a shock wave when the plasma flare is ignited on the surface of a target in the atmosphere leads to a shift of the center of the emission lines and to an increase in their intensity.
 [S1063-7850(97)00612-5]

The problem of the emission spectrum of a plasma flare on a target located in the atmosphere has been considered recently in connection with the development of analytical methods of laser spark spectroscopy of both solids[1] and liquids.[2–4] To heighten the contrast of the lines of the emission spectrum of the elements to be detected against the background of the continuous spectrum of the plasma flare, one uses laser radiation with a high power density, in excess of 10^9 W/cm^2, on the target surface. It is known[1] that at such intensities a shock wave arises in the atmosphere, causing additional heating of the erosion material coming off the target and also additional ionization of the atoms of the target and atmospheric gases. Thus the presence of a shock wave in the atmosphere can lead to an increase in the intensity of the emission lines on account of the additional heating and can give rise to a Stark shift on account of the enhancement of the local electric fields as a result of the additional ionization.

We have done experiments for the purpose of elucidating how the presence of the atmosphere affects the emission lines of the elements in a laser plasma. We investigated the emission spectra of a plasma flare generated by laser radiation on the surface of a solid target. A diagram of the experiment is shown in Fig. 1. A Nd:YAG laser with an output wavelength of 1.064 μm was used in the experiment; the use of a single gain cascade yielded an energy of laser radiation per pulse of up to 1 J at a duration (at half maximum) of the order of 15 ns. The laser radiation was focused by a lens with a focal length of 7 cm into an evacuable cell containing the target (an aluminum plate). A LiF crystal was used for Q switching. The emission spectrum was recorded using a double monochromator with a multichannel spectrum analyzer at the exit slit. The device gave a dispersion of 0.16 Å per element of the multichannel spectrum analyzer. The wavelength calibration of the spectrum was checked with a mercury lamp, the emission spectrum of which was recorded simultaneously with that of the plasma flare.

Figure 2a shows the spectrum of the plasma from the aluminum target when the cell was evacuated (pressure 10^{-1} Torr). The relative intensity of the spectral lines is plotted on the vertical axis, versus the wavelength in angstroms on the horizontal (in descending order). On the left is the calibration line of the mercury lamp at a wavelength of 4046 Å. To the right are the emission lines of aluminum at wavelengths of 3961 and 3944 Å.[5] The half-width of the lines is of the order of 1 Å and is due to the collisional broadening mechanism. Figure 2b shows the emission spectrum obtained at standard atmospheric pressure in the cell under otherwise identical conditions. The crosses in Fig. 2b indicate the positions of the emission lines of the aluminum atoms at a pressure of 10^{-1} torr. One sees that the Al emission lines are shifted toward the red region of the spectrum by an amount of the order of 1 Å. This shift was observed at a power density of the laser radiation on the target surface of over 10^9 W/cm^2 (the power densities were the same for the evacuated cell and the cell at standard pressure). The half-width of the emission line increased to 2 Å on going to standard pressure. Thus the broadening of the lines on going from the vacuum to a standard atmosphere is 1 Å, i.e., approximately equal to the shift of the line center, as is characteristic for a Stark mechanism.

The typical values of the density of target atoms and ions in the plasma at the given values of the power density of the laser radiation at the surface of the target are of the order of 10^{20} cm^{-3} (Ref. 6), which is higher than the density of atmospheric gases, so that it is difficult to attribute the shift and broadening of the line in the atmosphere to the interaction of the target atoms and ions with atmospheric gases. However, at such values of the radiation power density at the target surface the expansion of erosion material into the atmosphere gives rise to a supersonic radiational shock wave, which causes additional heating of the plasma.[1] Indeed, we detected a significant increase in the intensity of the Al emission lines on going from the evacuated cell to a standard atmosphere at the same values of the laser intensity. The increase in the intensity of the lines reached a factor of 22, which corresponds to an increase in the plasma temperature in the standard atmosphere by a factor of 19 in comparison with the temperature in the evacuated cell (the estimates were made from the ratio of the intensities of the same lines in vacuum and in the atmosphere on the assumption of thermodynamic equilibrium).[7] The ratio of the density of ions upon breakdown at the surface of the target in the atmosphere to the density of ions formed in the plasma flare when the target was in an evacuated cell was estimated from the broadening of the lines;[7] these estimates show that the energy of the ions is increased approximately 85-fold in comparison with the vacuum case. This should lead to a strong

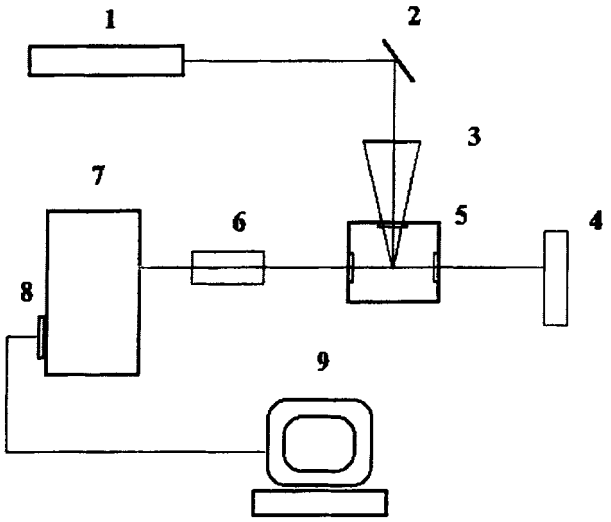

FIG. 1. Diagram of experimental apparatus: *1*—Nd:YAG laser and optical amplifier, *2*—mirror, *3*—focusing lens, *4*—mercury lamp, *5*—evacuable cell containing the target, *6*—objective, *7*—double monochromator, *8*—multichannel spectrum analyzer, *9*—computer.

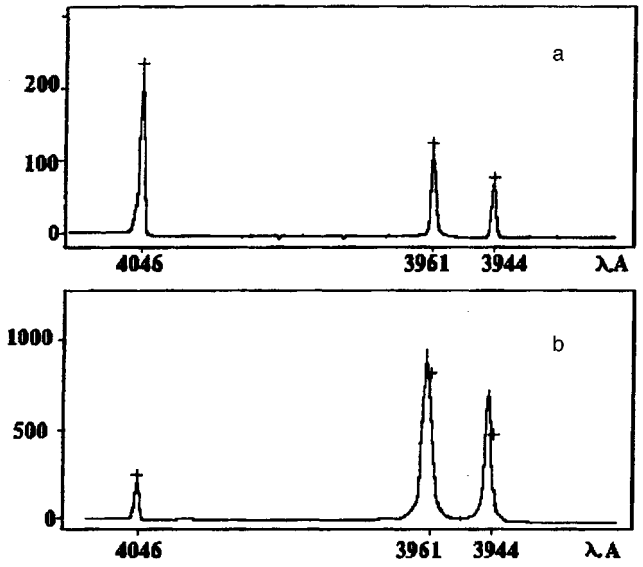

FIG. 2. Spectrum of the emission lines of Al: a—at a pressure of 10^{-1} Torr; b — at standard pressure.

increase in the local electric fields in which the emitting atoms are located and thus to a Stark shift of the emission lines, as was observed in the experiment.

Thus the onset of a shock wave in the excitation of a plasma flare on the surface of a target in the atmosphere can have at least two effects: a Stark shift of the line centers and an increased intensity of the emission lines on account of the additional heating by the shock wave.

[1] L. T. Sukhov, *Laser Spectrum Analysis* [in Russian], Nauka, Novosibirsk (1990).
[2] O. A. Bukin, A. N. Pavlov, N. V. Sushilov *et al.*, in *Proceedings of the Tenth All-Union Symposium on Laser and Acoustic Probing of the Atmosphere* [in Russian], Tomsk (1988), pp. 244–246.
[3] O. A. Bukin, A. N. Pavlov, and N. V. Sushailov, Zh. Prikl. Spektrosk. **52**, 736 (1990).
[4] D. V. Vlasov, A. M. Prokhorov, and D. Yu. Tsipenyuk, Kvantovaya Élektron. (Moscow), **18**, 1234 (1991) [Sov. J. Quantum Electron. **21**, 1120 (1991)].
[5] A. N. Zaĭdel', V. K. Prokof'ev, S. M. Raĭskiĭ *et al.*, *Tables of Spectral Lines*, Nauka, Moscow (1977).
[6] I. A. Bufetov, S. B. Kravtsov, and V. B. Fedorov, Kvant. Elektron. (Moscow) **23**, 535 (1996).
[7] S. É. Frish, *Optical Spectra of Atoms* [in Russian], Fizmatgiz, Moscow (1963).

Translated by Steve Torstveit

Nonlinear surface waves with allowance for the saturation effect

L. V. Fedorov and K. D. Lyakhomskaya

T. G. Shevchenko Pridnestrov State–Corporate University
(Submitted May 8, 1997)
Pis'ma Zh. Tekh. Fiz. **23**, 36–39 (December 12, 1997)

It is shown that for a medium with the dielectric function given by the expression $\varepsilon=\varepsilon_1+(\varepsilon_2-\varepsilon_1)\tanh(E^2/E_s^2)$, where ε_1 and ε_2 are constants and E_s is the saturation field, there is a threshold value of the power density at which a nonlinear surface wave can be excited. © *1997 American Institute of Physics.* [S1063-7850(97)00712-X]

Investigation of the properties of nonlinear surface waves is a topical problem in integrated optics. The properties of these waves have been studied for Kerr media whose refractive indices contain a term quadratic in the field.[1–3] For non-Kerr nonlinear media, however, it is necessary to obtain the refractive index from first principles, using the constitutive relations. In a number of studies[4,5] the properties of nonlinear surface waves have been studied with allowance for the saturation effect inherent to a system of two-level atoms. In Ref. 6 a simple nonlinearity was used, for which it was possible to obtain exact analytical solutions for the structure of the field and the dispersion relation. Saturation effects can also be modeled with other dielectric functions.

We have studied the properties of nonlinear surface waves propagating along a plane interface between two media, one of which is nonlinear. The dielectric function of the nonlinear medium is given by the expression

$$\varepsilon=\varepsilon_1+(\varepsilon_2-\varepsilon_1)\tanh(E^2/E_s^2), \quad z\geqslant 0, \tag{1}$$

where ε_1 and ε_2 are constants and E_s is the saturation field. The function (1) exhibits the saturation effect, since it varies from ε_1 to ε_2 as the amplitude of the field is increased from zero to infinity. We assume that the wave propagates along the x axis and that the electric and magnetic field vectors are oriented as shown in the inset to Fig. 1. Using Maxwell's equations, we obtain the following wave equations for the linear and nonlinear media, respectively:

$$\frac{d^2E}{dz^2}=\chi^2E, \quad \chi^2=k^2-\varepsilon_0\frac{\omega^2}{c^2}, \quad z\leqslant 0, \tag{2}$$

$$\frac{d^2E}{dz^2}=\left(q^2-(\varepsilon_2-\varepsilon_1)\,\frac{\omega^2}{c^2}\tanh(E^2/E_s^2)\right)E,$$

$$q^2=k^2-\varepsilon_1\frac{\omega^2}{c^2}, \quad z\geqslant 0. \tag{3}$$

We have found the solutions for the profiles of the electric field of the wave in the regions $z\geqslant 0$ and $z\leqslant 0$. In the nonlinear medium the field profile has a maximum, and

$$\int_{E_m/E_s}^{E/E_s}\frac{dy}{\sqrt{(n^2-\varepsilon_1)y^2-(\varepsilon_2-\varepsilon_1)\ln\cosh y^2}}=k_0z,$$

$$0\leqslant z\leqslant z_m, \tag{4}$$

$$\int_{E_x/E_s}^{E/E_s}\frac{dy}{\sqrt{(n^2-\varepsilon_1)y^2-(\varepsilon_2-\varepsilon_1)\ln\cosh y^2}}=k_0(z-z_m),$$

$$z_m\leqslant z\leqslant\infty, \tag{5}$$

where the position z_m of the maximum of the profile is given by the formula

$$\int_{E_0/E_s}^{E_m/E_s}\frac{dy}{\sqrt{(n^2-\varepsilon_1)y^2-(\varepsilon_2-\varepsilon_1)\ln\cosh y^2}}=k_0z_m,$$

$$k_0=\frac{\omega}{c}. \tag{6}$$

Here E_0 is the field amplitude at the interface between the two media and is determined from the continuity condition for the tangential component of the field at the interface, which results in the formula

$$(\varepsilon_0-\varepsilon_1)\,\frac{E_0^2}{E_s^2}=(\varepsilon_2-\varepsilon_1)\ln\cosh\frac{E_0^2}{E_s^2}. \tag{7}$$

The power density transported by the wave in the propagation direction is given by the expression

$$\frac{P}{P_0}=\frac{n\omega_0}{\omega}\left\{\frac{E_0^2/E_s^2}{\sqrt{n^2-\varepsilon_0}}+2F(E_m/E_s)-F(E_0/E_s)\right\}, \tag{8}$$

where

$$F(x)=\int_0^x\frac{\sqrt{y}\,dy}{\sqrt{(n^2-\varepsilon_1)y-(\varepsilon_2-\varepsilon_1)\ln\cosh y}},$$

$$P_0=\frac{c^2E_s^2}{16\pi\omega_0},$$

and ω_0 is the frequency of the transition responsible for the creation of the nonlinear function (1).

Numerical calculations for the dispersion relation of the propagating wave and the position of the maximum of the field profile were carried out for the following parameter values:

$$\varepsilon_0=2.4336, \quad \varepsilon_1=2.4025, \quad \varepsilon_2=2.56.$$

Figure 1 shows the dispersion relation, i.e., the dependence of the normalized power density on the effective refractive index of the composite medium. It is seen that a solution of equation (8) exists (a wave is excited) if $P>P_{\min}$. For the given values of the parameters one gets

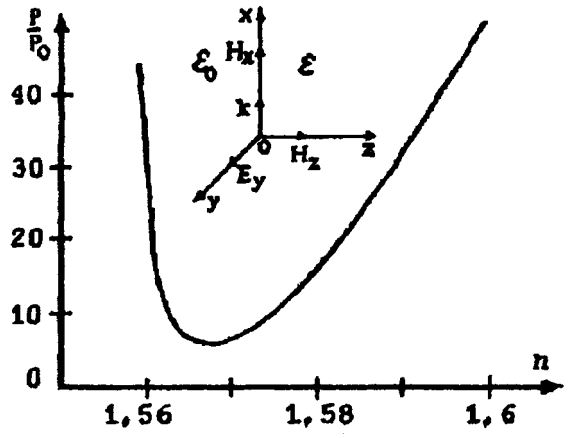

FIG. 1. Plot of the normalized power density P/P_0 versus the effective refractive index n of the medium.

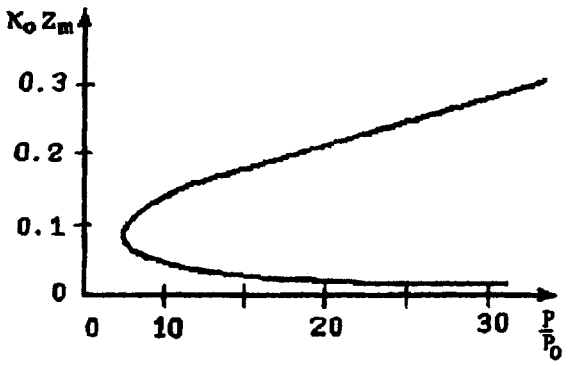

FIG. 2. Plot of the position $k_0 z_m$ of the maximum of the field profile in the nonlinear medium versus the normalized power density P/P_0.

$(P/P_0)_{\min}=7.286$ at $n=1.566$. For $P>P_{\min}$ each value of the normalized power density corresponds to two different values of the effective refractive index. For $n\to 1.56$ and $n\to 1.6$ the power density increases without bound, i.e., it is practically impossible to excite an electromagnetic wave with these values of n.

Figure 2 shows a plot of the position of the maximum of the field profile versus the normalized power density. It is seen that corresponding to each value of the normalized power density there are two different values of the maximum of the field profile, so that each value of the normalized power density corresponds to two different values of the effective refractive index.

Thus a medium with dielectric function (1) is characterized by a threshold value of the power density at which a nonlinear surface wave can be excited. For power densities below the threshold value such nonlinear surface waves do not exist. The results for the dielectric function (1) correlate with the results of Ref. 6, where a dielectric function that changed abruptly at a certain value of the field was used.

[1] N. N. Akhmediev, Zh. Éksp. Teor. Fiz. **84**, 1907 (1983) [Sov. Phys. JETP **57**, 1111 (1983)].
[2] M. Y. Yu, Phys. Rev. A **28**, 1855 (1983).
[3] V. M. Agranovich, V. S. Babichenko, and V. Ya. Chernyak, JETP Lett. **32**, 512 (1980).
[4] E. S. Kiseleva and P. I. Khadzhi, Opt. Spektrosk. **62**, 468 (1987) [Opt. Spectrosc. **62**, 279 (1987)].
[5] P. I. Khadzhi and E. S. Kiseleva, Zh. Tekh. Fiz. **57**, 395 (1987) [Sov. Phys. Tech. Phys. **32**, 242 (1987)].
[6] P. I. Khadzi and L. V. Fedorov, Zh. Tekh. Fiz. **61**(5), 110 (1991) [Sov. Phys. Tech. Phys. **36**, 564 (1991)].

Translated by Steve Torstveit

Application of Mel'nikov's method for estimating the efficacy of external signals on complex nonlinear systems with strange attractors

V. V. Afanas'ev, Yu. E. Pol'skiĭ, and V. S. Chernyavskiĭ

Kazan State Technical University
(Submitted June 11, 1997)
Pis'ma Zh. Tekh. Fiz. **23**, 40–45 (December 12, 1997)

Mel'nikov's method is used as a criterion for determining the condition for the onset of stochastization in nonlinear dynamical systems with strange attractors. Analytical conditions for the onset of stochastization in Duffing systems and Lorenz systems are obtained, from which one can synthesize a control signal ensuring the required behavior of the system. A mathematical experiment is carried out which confirms the correctness of the theoretical analysis.
 [S1063-7850(97)00812-4]

Complex nonlinear dynamical systems with strange attractors support qualitatively different processes: regular and stochastic. Controlling the behavior of a nonlinear dynamical system with a strange attractor is an important problem. It is known that control can be effected by small resonance signals matched with the internal properties of the dynamical system. The goal of this study is to estimate the efficacy of external influences on the behavior of a dynamical system with a strange attractor on the basis of the qualitative criterion of Mel'nikov's method.

The most widely used method of investigating processes occurring in dynamical systems with strange attractors is computer simulation. At the same time, it is of interest to explore analytical methods that would permit determination of the conditions for transitions of the system from one regime to another. There is a known analytical method due to Mel'nikov whereby one can determine the conditions for the onset of stochastization in systems which are close to being Hamiltonian systems[2] from the criterion for the onset of stochasticity in the neighborhood of a separatrix in the presence of dissipation in a nonlinear dynamical system.[3] Mel'nikov's method is based on an analytical, perturbation-theory calculation of the distance D between the separatrices of the system under analysis. A sign-varying nature of D means that the motion in the given region is chaotic.[2,3] Consequently, for determining the conditions for a transition of the system from a regular to a stochastic regime it is necessary to assess whether D changes sign.

It is known that the behavior of a Lorenz dynamical system

$$\dot{x}=\sigma(y-x),$$

$$\dot{y}=rx-y-xz,$$

$$\dot{z}=xy-bz \tag{1}$$

near points of unstable equilibrium (c_1 and c_2, with coordinates $\pm x_0=\pm y_0=\pm\sqrt{b(r_0-1)}$, $z_0=r_0-1$) can be written in the form of Duffing's equation with an anharmonic periodic right-hand side.[4]

For a Duffing nonlinear dynamical system with an arbitrary right-hand side $\gamma(t)$,

$$\ddot{x}-\varepsilon\delta\dot{x}-x+x^3=\gamma(t), \tag{2}$$

in the case when an additive external control signal $\beta(t)$ is used, the splitting D, according to Mel'nikov's method, is of the form

$$D=\sqrt{2\pi}\sum_{n=1}^{\infty}\operatorname{ch}^{-1}(\pi n\Omega/2)(-n\Omega a_n\sin(n\Omega t_0)+n\Omega b_n\cos(n\Omega t_0))+4\delta/3, \tag{3}$$

where a_n and b_n are the Fourier expansion coefficients of the function

$$\alpha(t)=\gamma(t)+\beta(t),$$

with $\gamma(t)$ being the right-hand side of Duffing's equation and $\beta(t)$ the internal control signal acting on the dynamical system.

It follows from expression (3) that the main influence on the onset of stochastization in a Duffing dynamical system acted on by external periodic influences comes from the first harmonics $\gamma(t)$ and $\beta(t)$, since the denominator $\cosh(\pi n\Omega/2)$ increases sharply with increasing coefficient n. Therefore, to eliminate stochastization one can use harmonic control signals $\beta(t)$ even in the case of an anharmonic $\gamma(t)$. The most effective signals here are the quasiresonance, $\Omega\cong\omega_{kb}$, and the inertial, $\Omega\geqslant\omega_{kb}$ (ω_{kb} is a quasi-resonance frequency of the system).[1]

It should be noted that the change in sign of the splitting D, as can be seen from Eq. (3), also depends on the phase relations between the harmonic components $\gamma(t)$ and $\beta(t)$; upon a change in the phasing both regularization and stochastization of the dynamical systems can occur.

In the case of a periodic modulation of the parameter r of a Lorenz system in the form $r=r_0+r(t)$, we obtain from Eq. (1)

$$\ddot{x}-x\sigma(r_0-1)+x^3\sigma/b=-\dot{x}(\sigma+1+x^2/b)+\alpha(t), \tag{4}$$

where $\alpha(t)=\sigma x[\dot{z}/b+r(t)]$, and r_0 is the constant component of r.

By analogy with the Duffing equation considered above we can conclude that for eliminating the stochastic regime in a Lorenz system one can use a harmonic signal $r(t)$ with a

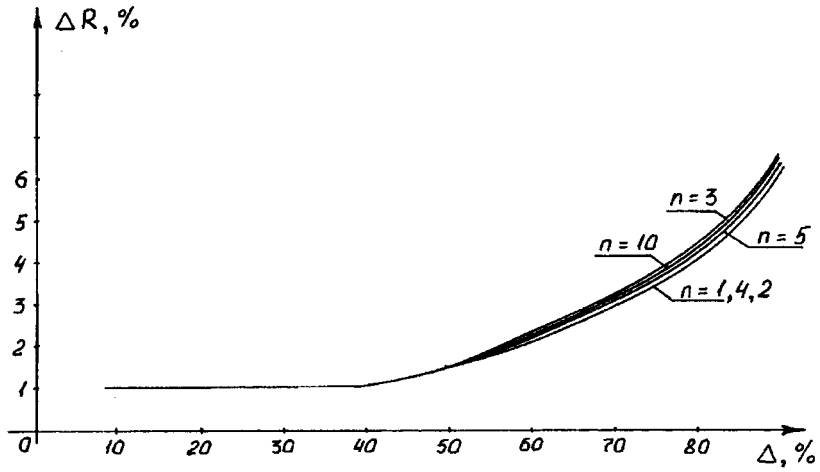

FIG. 1. Relationship between the initial deviation Δ of the system from the points c_1 and c_2 and the value of the minimum amplitude ΔR of the control signal necessary to ensure the elimination of dynamical chaos in the Lorenz system for different values of the parameter n of the control signal.

frequency $\Omega \cong \omega_{kb}$ and a suitable phase shift; here the quasiresonance frequency ω_{kb} can be estimated from the analytical formula obtained in Ref. 1.

The phase shift of the control signal $r(t)$ in the Lorenz system describing the dynamics of processes occurring in lasers[5] has a clear physical meaning. Indeed, to ensure stability of the output it is necessary to increase the pump power of the laser upon a decrease in the amplitude of the field oscillations in the laser and to lower the pump power upon an increase in the amplitude of the oscillations. And because the parameter r is proportional to the pump intensity,[5] the modulation of r should be done with allowance for the change in amplitude of the field oscillations (the variable x) and the number of particles of the medium which interact with the radiation (the variable z).

As the phased control signal acting on the parameter r we propose to use a signal of the type

$$r(t) = r_0 + \Delta R Q,$$
$$Q = Q_1 \quad \text{for} \quad z \geqslant r_0 - 1,$$
$$Q = Q_2 \quad \text{for} \quad z < r_0 - 1, \tag{5}$$

where Q is a train of pulses of unit amplitude with positive (Q_1) and negative (Q_2) polarity and with a reciprocal duty factor (period-to-duration ratio) of 2 and a repetition rate $n\omega_{kb}$.

The efficacy of the proposed control signal was estimated by a statistical simulation of the behavior of a Lorenz system with the characteristic parameters $r_0 = 28$, $\sigma = 10$, $b = 8/3$ (Ref. 3) and a function $r(t)$ of the form (5). In the Lorenz system in the absence of a control signal, dynamical chaos sets in and a strange attractor appears. We investigated the relationship between the initial deviation of the system Δ from the points c_1 and c_2 and the value of the minimum amplitude ΔR of the control signal necessary to effect the elimination of dynamical chaos in the Lorenz system for different values of the parameter n of the control signal. The results of the experiment are presented in Fig. 1. It was found that the minimum necessary value of ΔR depends to a significant degree on the initial deviation Δ of the system and is practically independent of the number n of the harmonic. This is in good agreement with the conclusion, which follows from Eq. (3), that the behavior of the dynamical system is mainly influenced by the first harmonic of the control signal. Indeed, as n in Eq. (5) varies, so does the form of $r(t)$, but there is little effect on the envelope $r(t)$ with the frequency ω_{kb}, and it is this envelope, as we have shown in this study, that has the decisive influence on the behavior of the dynamical system. It is seen from Fig. 1 that the use of a control signal (5) with a modulation index of the order of 7% can eliminate dynamical chaos in the Lorentz system at an initial deviation Δ from the points c_1 and c_2 of up to 90%; this indicates that the use of such a signal would be highly effective for controlling the behavior of the dynamical system.

Thus the proposed form of the quasi-resonance control signal provides an efficient means of controlling the behavior of dynamical systems with strange attractors.

CONCLUSIONS

1. The qualitative criterion of Mel'nikov's method can be used to analyze the behavior of dynamical systems with strange attractors in the presence of external influences.

2. A study of the behavior of the nonlinear dynamical system with a strange attractor by the Mel'nikov method has shown that quasi-resonance signals are highly effective in controlling the behavior of the system. When a quasi-resonance signal is used, one must take into account the phase relations between the internal stochastizing influence $\gamma(t)$ and the external control signal $\beta(t)$ acting on the dynamical system.

3. A mathematical simulation of the behavior of a Lorenz system showed that the use of the proposed signal acting on the parameter r of the Lorenz system with a modulation index of several percent can ensure the establishment of a regular regime in a system which, in the absence of a control signal, is found in a stochastic regime. The initial relative deviation of the system from the state of unstable equilibrium here can reach 90%, which indicates that the proposed form of control signal is highly efficient.

[1] V. V. Afanas'ev and Yu. E. Pol'skiĭ, Pis'ma Zh. Tekh. Fiz. **15**(18), 86 (1989) [Sov. Tech. Phys. Lett. **15**, 741 (1989)].
[2] V. K. Mel'nikov, Tr. Mosk. Matem. Obshchestva, Vol. 12 (1963).
[3] A. J. Lichtenberg and M. A. Lieberman, *Regular and Stochastic Motion*, Springer-Verlag, New York (1983) [Russian transl., Mir, Moscow (1984)].
[4] V. V. Afanas'ev and Yu. E. Pol'skiĭ, Pis'ma Zh. Tekh. Fiz. **17**(8), 57 (1991) [Sov. Tech. Phys. Lett. **17**, 299 (1991)].
[5] A. N. Oraevskiĭ, Kvantovaya Elektron. (Moscow) **8**, 130 (1981) [Sov. Tech. Phys. Lett. **11**, 71 (1981)].

Translated by Steve Torstveit

Detection of nitrogen dioxide by means of a gold film in a surface-plasmon resonance scheme

P. I. Nikitin, A. A. Beloglazov, A. N. Grigorenko, A. I. Savchuk, P. M. Anokhin, and J. D. Wright

Institute of General Physics, Russian Academy of Sciences, Moscow
(Submitted July 14, 1997)
Pis'ma Zh. Tekh. Fiz. **23**, 46–51 (December 12, 1997)

It is demonstrated that nitrogen dioxide can be detected by means of a gold film in a surface-plasmon resonance scheme. The sensor response is reversible at room temperature and permits detection of nitrogen dioxide down to concentrations of the order of 1 ppm. © *1997 American Institute of Physics.* [S1063-7850(97)00912-9]

The method of surface-plasmon resonance was used in Refs. 1–3 to detect the reversible interaction of microimpurities (4–10 ppm) of nitrogen dioxide (NO_2) in air by means of gold films. The effect was detected from the change in the resonance peak of the photosignal for films on silicon lattices and from the minimum of the reflection for films on glass substrates. The response had a high selectivity and was absent for a number of other gases and vapors (methane, dichloromethane, ethanol). The size of this response is on a par with the analogous response for phthalocyanine films deposited on gold. The latter are conventionally used in combination with gold in surface-plasmon resonance schemes[4] as materials sensitive to oxides of nitrogen, but the possibility of a sensor effect for gold itself had not been considered prior to the appearance of Refs. 1–3. In the present paper we show for the first time that the interaction of NO_2 with gold can be used to create NO_2 sensors, and we analyze possible mechanisms for this interaction.

A diagram of the experiment is shown in Fig. 1. Gold films 40–50 nm thick were deposited at a rate of 2–5 nm/s by an electron-beam technique on a cleaned glass substrate in a diffusion-pump vacuum of 10^{-6} Torr. Surface plasmons were excited by radiation of wavelength 633 nm by the Kretschmann method[5] on the surface of gold in a flow of dry air containing 10 ppm NO_2 or pure dry air at room temperature. The reflected signal was recorded as the angle of incidence was scanned or for a fixed position close to the resonance minimum of the reflection. The films had a reflection minimum at the 3–11% level with a resonance half-width of 1.5–2.4°.

In the initial position of the reflection minimum, the signal increased when the mixture containing NO_2 was admitted and then slowly recovered when pure air was admitted (Fig. 2a). The time required for the response to reach saturation was 1–1.5 h, and the time for recovery of the signal was 6–8 h (the latter is an order of magnitude shorter in air with a relative humidity of 60%; Refs. 1–3). The response and recovery signals of newly deposited films also contained a faster component varying over times of the order of 10 s. The response was always accompanied by a shift of the resonance curve (of up to 0.2°) to larger angles of incidence (Fig. 2b), with a slight increase in the level of the minimum (by not more than 0.3% of the level of total reflection). Such a shift explains the different signs of the response detected[1–3] for different initial detunings relative to the minimum.

The behavior of the signal was similar in character for several tens of samples prepared at different laboratories. Although the amplitude of the response varies substantially from one film to another, the cycles of response and recovery for each sample was reproduced to good accuracy, so that this effect can be used to make NO_2 sensors. The surfaces of the gold films were studied under a scanning tunneling microscope, which did not reveal any features that would lead to different amplitudes of the response (the large-scale structure was qualitatively the same for all the samples; Fig. 3). The films were continuous, without breaks, and consisted of grains 10–20 nm in size in the plane of the film and had deeply penetrating and ramified grain boundaries.

Such a structure is typical for gold films on different substrates (see Ref. 6 and the references cited therein).

Let us examine the possible mechanisms for the observed reversible interaction, using a macroscopic model of surface-plasmon resonance in a multilayer system. One of these mechanisms involves a change in the properties of the gold surface, and the other a decrease in the volume density of conduction electrons on account of their binding to the electron-acceptor molecules NO_2.

Using the Drude model of an electron gas, one can easily estimate that the observed shift of the resonance curve (see Fig. 2c) corresponds to a 5% decrease in the density of conduction electrons in the gold film (the data of Ref. 7, where

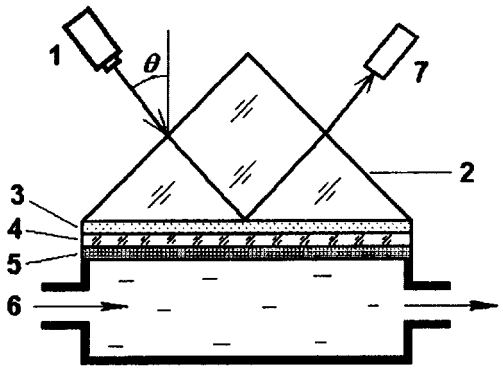

FIG. 1. Diagram of the measurements: *1* — helium–neon laser, *2* — glass prism, *3* — immersion fluid, *4* — glass substrate, *5* — gold film, *6* — chamber with gas flow, *7* — photodetector; θ is an angle to be measured.

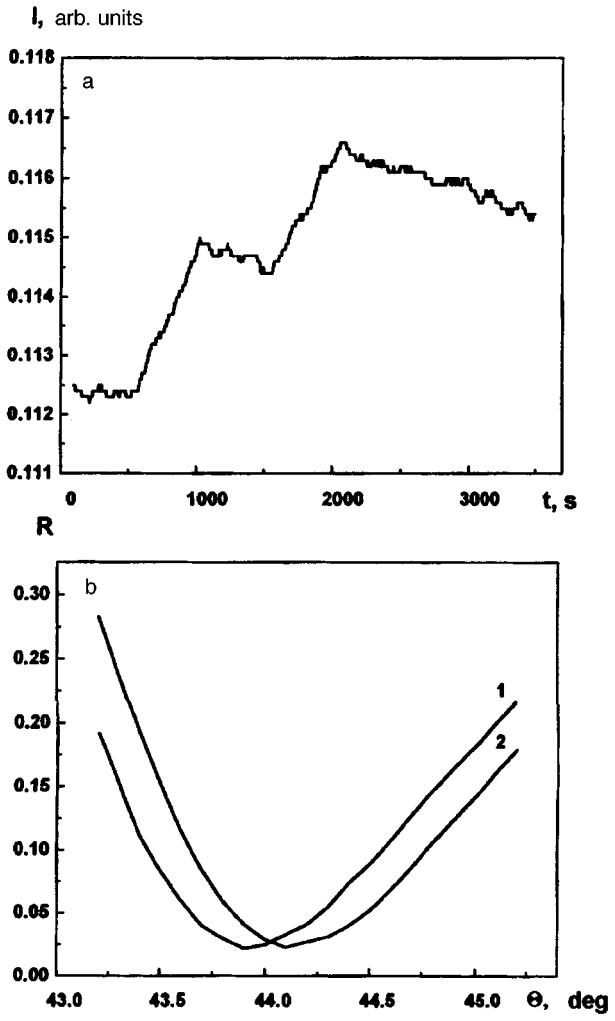

FIG. 2. The behavior of the reflected signal: a—at a fixed adjustment to the initial position of the resonance minimum; a mixture of dry air with 10 ppm NO_2 is admitted at the times $t=500$ s and $t=1500$ s, and pure dry air is admitted at the times $t=1000$ s and $t=2000$ s; b—as a function of the angle of incidence near the resonance minimum: *1* — in pure dry air, *2* — in dry air with 10 ppm NO_2, at an exposure time of 3000 s.

films were prepared under similar conditions, were used in the calculation). However, the experiment showed that the resistance of a film exposed to NO_2 remained unchanged to within 1%. In addition, a decrease in the electron density leads to a broadening of the resonance and to an increase in the minimum reflection level. On the basis of the observed increase in the minimum reflection level (see Fig. 2b), one can place a bound of 0.3% on the decrease in the conductivity of the film. This result agrees with the reported[8] reversible increase in the resistance of 0.1% in thin (10–60 nm) gold films exposed to NO.

Thus the shift of the resonance curve should be attributed to a change in the surface properties of the gold film on interacting with NO_2. As an extremely simple model we can propose the formation of a thin, uniform surface layer. A calculation shows that an insulating layer 1.4–0.9 nm thick, with a refractive index of 1.4–1.8, can give the observed shift. At room temperature nitrogen dioxide exists mainly in the dimer form N_2O_4, which is a transparent liquid with a boiling temperature of 20.6°C and a molecular size of around 0.3 nm; it can be adsorbed (can condense) in several molecular layers,[9] and the extended surface of the film (Fig. 3) is substantially greater than the effective thickness of the adsorbed layer. Therefore, the formation of a surface layer with the indicated parameters is quite likely.

The question of the extent to which the proposed model corresponds to the actual processes occurring on the surface in the presence of adsorbates from the air must be answered by deeper studies on the microscopic level. The reversible sensor response is presumably due to the adsorption/desorption of NO_2 and N_2O_4 molecules, and the adsorption forces are due to their high electron affinity. These forces cannot be dipolar, since the effect is absence for dichloromethane and ethanol, and the dipole moment of their molecules is five times greater than that of NO_2 (the N_2O_4 molecule is centrosymmetric and is not dipolar). The extended surface of the film (Fig. 3), with a large number of pores

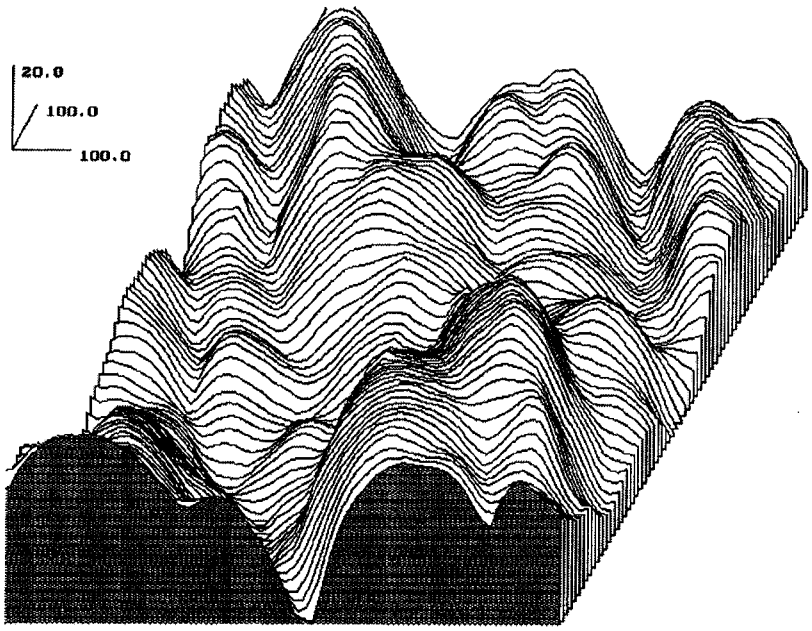

FIG. 3. Image of the surface of a gold film obtained by means of a scanning tunneling microscope; the image has been smoothed to eliminate noise spikes. The scales in the three dimensions are indicated in angstroms.

between grains, creates conditions for strong adsorption with processes of volume filling of micropores and layered filling of mesopores through capillary condensation.[9] The filling of the pores by a condensate of N_2O_4 can decrease the intergrain and overall conductivity of the film by decreasing the density of conduction electrons and/or their relaxation time in inelastic scattering on grain boundaries. For a surface-plasmon resonance it is equivalent to an increase in the effective thickness of the adsorbed layer. The sharp decrease in the recovery time of the signal in moist air may be due to a reaction of N_2O_4 with water vapor.

In summary, we have demonstrated the possibility of detecting nitrogen dioxide by means of a gold film in a scheme of surface-plasmon resonance and have considered the possible mechanisms for the observed reversible response. This effect is promising for applications in sensors in view of its large magnitude and reproducibility and the possibility of rapid recovery of the signal, e.g., by using moist air or a heating pulse.

This study was supported by the Russian Fund for Fundamental Research, under Grant No. 95-02-04372.

[1] P. I. Nikitin, A. A. Beloglazov, and M. V. Valeiko *et al.*, Preprint No. 8 [in Russian], Institute of General Physics, Russian Academy of Sciences, Moscow (1996).
[2] P. I. Nikitin, A. A. Beloglaszov, and M. V. Valeiko *et al.*, in *Proceedings Eurosensors X*, Leuven, Belgium, September 8–11, 1996, p. 51.
[3] P. I. Nikitin, A. A. Beloglazov, and M. V. Valeiko, Sens. Actuators B **38(13)**, 53 (1997).
[4] J. D. Wright, A. Cado, and S. J. Peacock, Sens. Actuators B **29(1-3)**, 108 (1995).
[5] E. Kretschmann, Z. Phys. **241**, 313 (1971).
[6] M. A. George, Q. C. Bao, and I. W. Sorensen, J. Vac. Sci. Technol. A **8**, 1491 (1990).
[7] B. Johnson and R. W. Christy, Phys. Rev. B **6**, 4370 (1972).
[8] K. Toda, K. Ochi, and I. Sanemasa, Sens. Actuators B **32(1)**, 15 (1996).
[9] *Chemical Encyclopedia* [in Russian], Sov. Éntsiklopediya, Moscow (1988), Vol. 1, pp. 54, 94.

Translated by Steve Torstveit

Some physical properties of an Al_2O_3–SiC–TiC composite

B. I. Smirnov, V. I. Nikolaev, and Yu. A. Burenkov

A. F. Ioffe Physicotechnical Institute, Russian Academy of Sciences, St. Petersburg

J. L. Routbort and K. C. Goretta

Argonne National Laboratory, Argonne, Illinois 60439-4838, USA
(Submitted August 13, 1997)
Pis'ma Zh. Tekh. Fiz. **23**, 52–58 (December 12, 1997)

Ceramic samples obtained by hot pressing from a mixture of Al_2O_3 with admixtures of 23 vol.% TiC powder and 30.9 vol.% SiC whisker crystals are investigated experimentally. The resistivity of the material is measured at temperatures of 4.2–300 K, the infrared reflection spectra are recorded in the region 400–4200 cm^{-1}, and the temperature dependence of the Young's modulus is investigated at temperatures up to 1300 K. As a result it is it is shown that the conductivity and optical reflection of the high-strength composite have a semimetallic character, which is due to the titanium carbide particles contained in it. © *1997 American Institute of Physics.* [S1063-7850(97)01012-4]

Research on the physical and mechanical properties of ceramic-based composites is of great scientific and practical interest. This is primarily because these materials have high strength and viscosity together with a high resistance to high-temperature creep.[1–5] On the other hand, the presence of these properties leads to significant technological difficulties in the fabrication of items and their mechanical processing. Producing such materials with a sufficiently high electrical conductivity could eliminate these difficulties by permitting the use of electrospark cutting and, in the fabrication of cutting instruments, electrospark sharpening. It turns out that such a combination of physical and mechanical properties can be found, in particular, in a composite based on Al_2O_3 with admixtures of TiC and β-SiC whisker crystals (AlSiTi).[6] At the same time, there is practically no information in the literature about the physical properties (and the nature of the conductivity) of AlSiTi composites.

The goal of the present study was to investigate certain physical properties of AlSiTi and compare them with data on the microstructure.

The material investigated (Crystaloy 2311EDX) was made by Industrial Ceramic Technology, Inc. from an Al_2O_3 powder with an admixture of 23.0 vol.% TiC powder and 30.9 vol.% β-SiC whisker crystals having a length of 50 μm. The density of the composite after hot pressing was

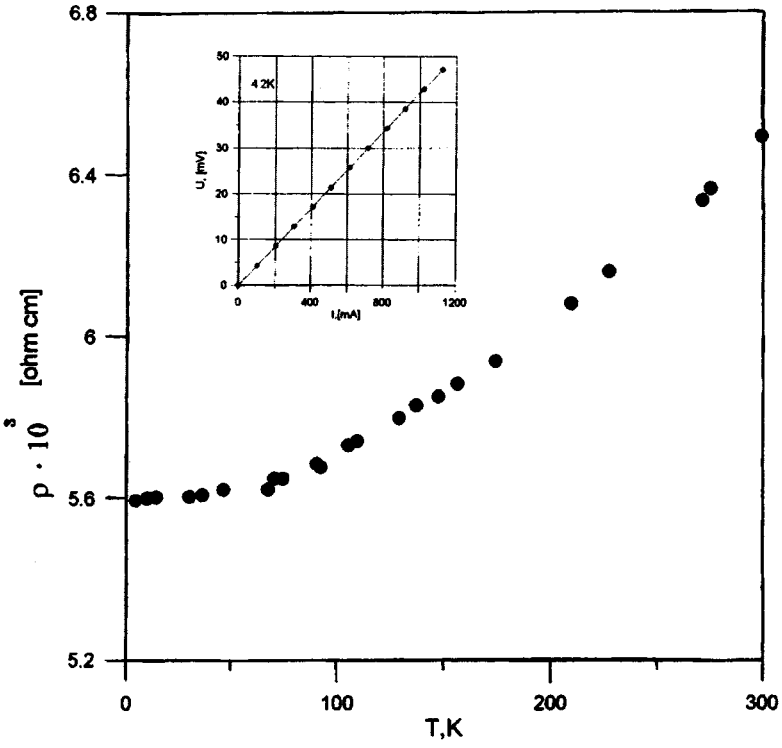

FIG. 1. Temperature dependence of the resistivity of the AlSiTi composite. The inset shows the current–voltage characteristic of the sample at 4.2 K.

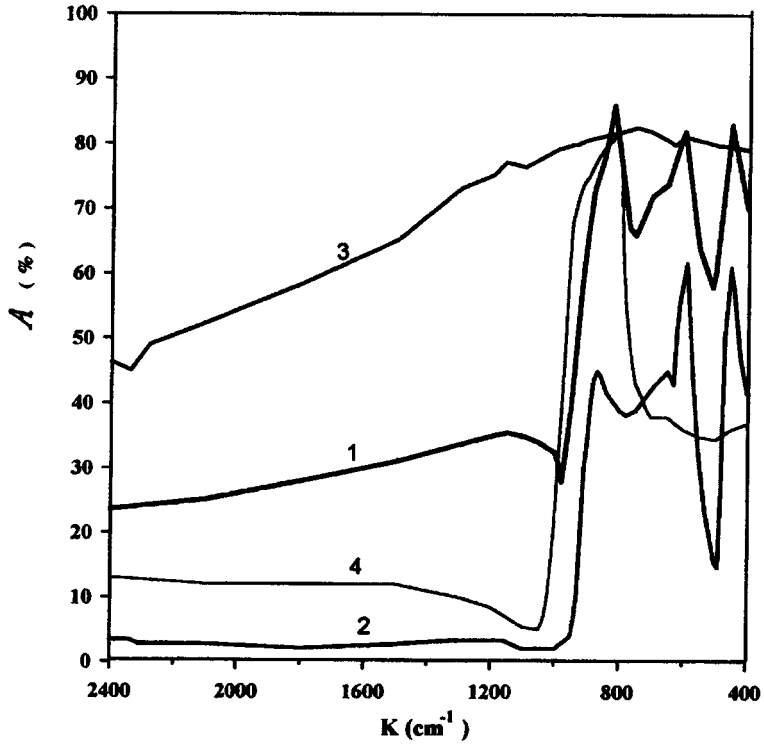

FIG. 2. Infrared reflection spectra for ceramic samples of AlSiTi (*1*), Al_2O_3 (*2*), and TiC (*3*) and a β-SiC single crystal (*4*).

$d = 3.915$ g/cm^2, which is around 99% of the theoretical density.

The dc resistance measurements were done by the four-probe method. Potential contacts were deposited on the face of the sample ($2.5 \times 2.5 \times 15$ mm) by the rubbing in of indium. The current contacts were clamped. Measurements were made in the temperature interval 4.2–293 K in a helium cryostat, the temperature of which was regulated by an Oxford ITC4 controller.

The infrared reflection spectra were investigated in the wave-number range $K = 4200$–400 cm^{-1} on an IKS-29 spectrometer operating in a two-beam arrangement.

The Young's modulus E was determined by a resonance method under electrical excitation of longitudinal vibrations

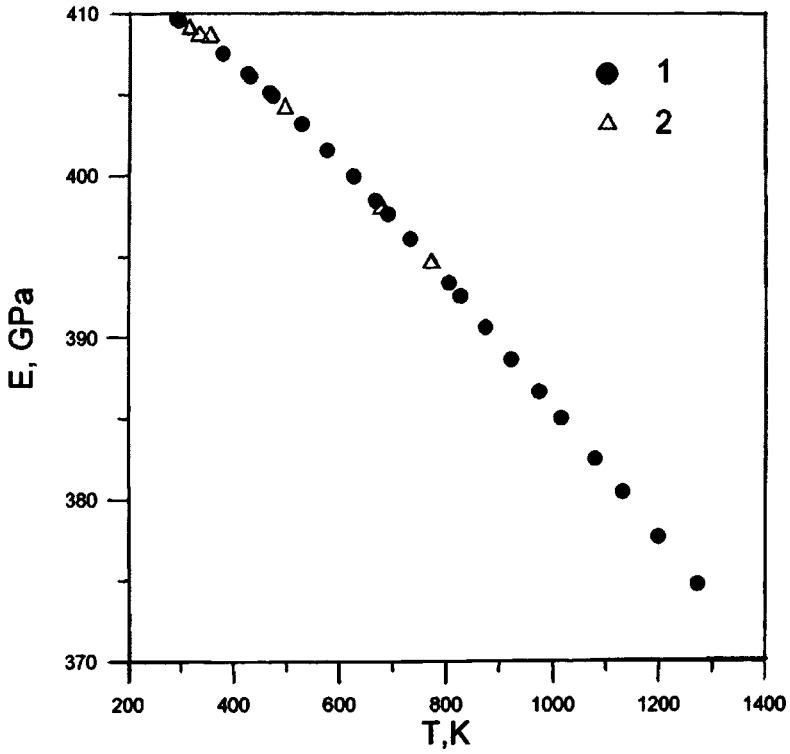

FIG. 3. Temperature dependence of the Young's modulus of AlSiTi on heating (*1*) and cooling (*2*) of the sample.

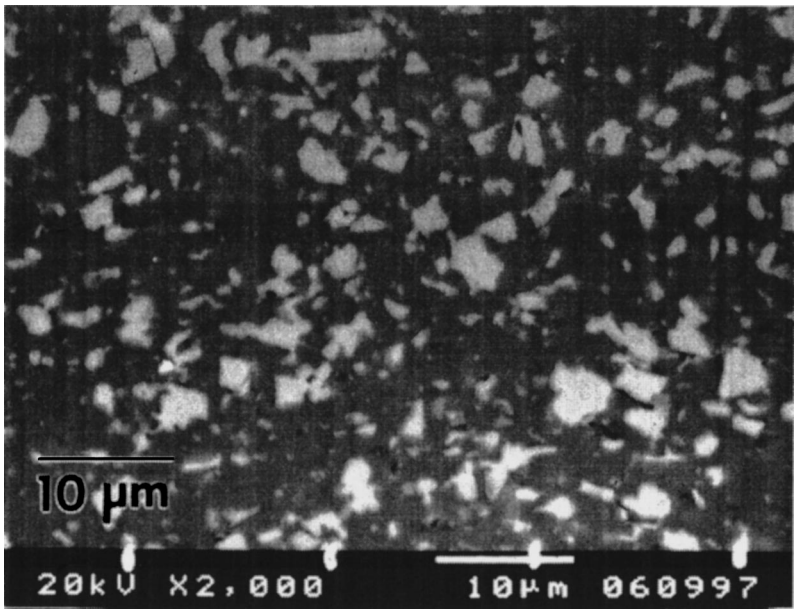

FIG. 4. Microstructure of the AlSiTi composite under a scanning electron microscope. The bright regions correspond to TiC particles.

in the sample.[7] The value of E was calculated from the data on the resonance frequency f as $E=4dl^2f^2n^{-2}$, where l is the length of the sample and n is the number of the harmonic that is excited (in our case $n=1$). Samples with dimensions of $2.4\times2.4\times24.5$ mm were cut out for the acoustic measurements. The density d was determined by hydrostatic weighing at room temperature. The experiments were done in the temperature interval 290–1300 K in a helium-filled chamber. A detailed description of the apparatus and procedure for measuring f is given in Ref. 8.

The structural studies were done with a scanning electron microscope (SEM) and x-ray diffractometer.

The results of the electrical measurements are presented in Fig. 1. The inset shows the current–voltage characteristic of AlSiTi at 4.2 K, which implies that the resistance of the sample and contacts is of an Ohmic character. The temperature dependence of the resistivity ρ, also shown in Fig. 1, has a metal-like character, although the resistivity of AlSiTi ($\sim6\times10^{-3}$ $\Omega\cdot$cm) is several orders of magnitude higher than in metals. We note that ρ decreases practically linearly as the temperature is lowered from 300 to 120 K, after which the decrease slows abruptly. The overall change in ρ between 300 and 4.2 K is around 12%. A similar change in ρ in the interval 77–300 K has been observed in TiC samples, although, granted, the absolute value of ρ at 300 K in that case was 6×10^{-5} $\Omega\cdot$cm.[9]

Figure 2 shows the infrared reflection spectra at room temperature for ceramic samples of AlSiTi, Al_2O_3, and TiC and for β-SiC single crystals. A comparison of the spectra shows that the reflectivity from ceramic AlSiTi in the region of large wave numbers is determined by its titanium carbide component, since only TiC can give the ceramic a high level of reflectivity outside the wavelength region of lattice reflection. Meanwhile, the characteristic infrared spectrum of the ceramic in the region of small wave numbers is indicative of a large content of crystalline Al_2O_3. The infrared data on the composition of the ceramic are in good agreement with the results of scanning electron microscopy and x-ray structural analysis, which showed a high percent content of the pure components TiC and Al_2O_3 in the composite. At the same time, the presence of several weak reflections which cannot be assigned to any of the components is evidence of possible chemical reactions between them during sintering.

Figure 3 shows data on the temperature depend of the Young's modulus of AlSiTi. It is seen that the dependence is nonlinear in the region 290–800 K but for $T>800$ K there is a linear decrease of E with temperature. At room temperature the Young's modulus of AlSiTi is $E=409.6$ GPa, which is somewhat smaller than the values for the main elements of the matrix of the composite: Al_2O_3 ($E_{[0001]}=470$ GPa) and TiC ($E=460$ GPa).[10,11]

Thus the experimental results indicate that the conductivity of the AlSiTi composite is of a semimetallic character and is due to the presence of titanium carbide in it. According to the SEM data the TiC powder particles maintain their integrity in the hot pressing process, and they have an average size of ≈5 μm (Fig. 4). In this situation the average conductivity of the composite is most likely determined by percolation effects.

The authors are grateful to A. S. Zubrilov for doing the optical measurements, to I. N. Zimkin for the x-ray study of the samples, and to Prof. W. C. Williams for providing the TiC samples.

This study was done with the support of NATO (High Technology Grant GRG/N960793) and the USA Department of Energy (Contract W-31–109–Eng–38).

[1] A. G. Evans and D. B. Marshall, Acta Metall. **37**, 2567 (1989).
[2] H. T. Lin and P. F. Becher, J. Am. Ceram. Soc. **73**, 1378 (1990).
[3] J. P. Singh, K. C. Goretta, J. L. Routbort, D. S. Kuppermann, and J. F. Rhodes, Adv. Ceram. Mater. **3**, 357 (1988).
[4] J. L. Routbort, K. C. Goretta, A. R. Dominguez–Rodriguez, and A. de Arellano-Lopez, J. Hard Mater. **1**, 221 (1990).
[5] A. R. de Arellano-Lopez, A. Dominguez–Rodriguez, K. C. Goretta, and J. L. Routbort, J. Am. Ceram. Soc. **76**, 1425 (1993).
[6] J. J. Sculdies, Compos. Manuf. **8**(4), 1 (1992).

[7] H. J. McSkimin, in *Physical Acoustics*, Vol. 1 (edited by W. P. Mason), Academic Press, New York (1964), p. 271.
[8] Yu. A. Burenkov, S. P. Nikanorov, and A. V. Stepanov, Izv. Akad. Nauk SSSR, Ser. Fiz. **35**, 525 (1971).
[9] W. S. Williams, Science **152**, 34 (1966).
[10] L. Wang, M. R. Wixom, and L. T. Thompson, J. Mater. Sci. **29**, 534 (1994).
[11] M. P. Shaskol'skaya (Ed.), *Acoustic Crystals* [in Russian], Moscow (1992), p. 294.

Translated by Steve Torstveit

Angular momentum of the fields of a few-mode fiber. III. Optical Magnus effect, Berry phase, and topological birefringence

A. V. Volyar and T. A. Fadeeva

Simferopol State University
(Submitted June 13, 1997)
Pis'ma Zh. Tekh. Fiz. **23**, 59–67 (December 12, 1997)

It is shown that, on the one hand, the evolution of the angular rotation of the lines of nodes of the CP_{11} mode is a manifestation of the optical Magnus effect in a few-mode fiber with a parabolic refractive index profile, and, on the other hand, the additional phase $\gamma_b = \pm \delta\beta_{21} z$ in CV and IV vortices is the Berry topological phase, which arises as a result of the cyclic change in the orientations of the orthogonal axes of dislocations. The splitting of the propagation velocities of orthogonal circularly polarized CV^+ and IV^- modes in an LV vortex in a parabolic fiber is a manifestation of the phenomenon of topological birefringence of a few-mode fiber. The azimuth of the linear polarization of a vortex undergoes continuous angular rotation. In an optical fiber with a stepped index profile the CP_{11} mode forms circularly polarized edge dislocation over lengths which are multiples of half the beat length, and over lengths which are odd multiples of the quarter beat length it forms linearly polarized fields with a purely screw dislocation. This transformation of edge and screw dislocations can be regarded formally as conversion of the polarizational angular momentum into orbital angular momentum. The conversion of angular momentum is a reflection of the dynamical unity of the optical Magnus effect and the Berry topological phase in the fields of a few-mode fiber. [S1063-7850(97)01112-9]

The problem of the change in angular orientation of the ray trajectory of a local transverse mode in a few-mode optical fiber upon a change in the direction of circulation of the polarization of the initial mode (the optical Magnus effect) was first touched upon in Ref. 1. In terms of physically observable quantities the optical Magnus effect has been interpreted as polarizational rotation of wave caustics[2] or of the speckle pattern of the radiation field.[3]

According to Zel'dovich and Liberman,[1] the optical Magnus effect is the inverse effect of accumulation of Berry topological phase, in accordance with the mechanical principle that the action is equal to the reaction.

As we know, the Berry phase has a purely quantum topological character and is the result of a cyclic adiabatic variation of the parameters of the Hamiltonian in configuration space.[4] In optics the Berry topological phase has been known as the Rytov effect[5] of rotation of the plane of polarization of a local transverse mode propagating along a nonplanar ray trajectory (cyclic variation of the direction of the wave vector). The transformation of the Berry topological phase in multimode fibers has been studied in Refs. 6 and 7. Although in their early papers[8,9] Fedorov and Imbert[10] had shown that a finite electromagnetic plane wave should undergo a lateral shift (or in curvilinear spaces, an angular rotation), which is of a purely electromagnetic nature, Liberman and Zel'dovich[11] attached a topological interpretation to the optical Magnus effect. In their opinion the topological character of this effect derives from the spin–orbit interaction of the ensemble of photons propagating in an inhomogeneous medium. The topological nature of the effect is also reflected in the combined influence of the Magnus effect and Berry phase, which causes topological birefringence of an inhomogeneous medium.[12,13] In few-mode fibers it is no longer possible to use ray theory, and a light wave is not purely transverse. Therefore, both the optical Magnus effect and the Berry topological phase in these system do not have an obvious representation.

The goal of the present study was to investigate the features of the optical Magnus effect, Berry topological phase, and the topological birefringence of mode combinations of few-mode fibers with stepped and parabolic profiles of the refractive index.

1. Let us first consider the propagation of a circularly polarized CP_{11} mode[14] in a few-mode fiber with a parabolic refractive index profile. In such a fiber the polarizational corrections to the propagation constants of the TE_{01} and TM_{01} modes are equal to each other ($\delta\beta_2 = \delta\beta_4$). Expressions for the electric and magnetic fields of the $CP_{11}^{\pm,e}$ mode, for example, can be written in the form[14,15]

$$\mathbf{e}_t(\mathrm{CP}_{11}^{\pm,e}) = \hat{\mathbf{e}}^{\pm}\cos(\varphi - \sigma\delta\beta_{21} z) F_1 \exp(i\beta' z),$$

$$e_z = i\frac{\sqrt{2\Delta}}{V}(G_1^- \exp\{i(\beta_1 z + \sigma 2\varphi)\} + G_1^+ \exp\{\mathbf{i}\beta_2 z\}),$$

$$\mathbf{h} = -in_{co}\sqrt{\frac{\varepsilon_0}{\mu_0}}\,\mathbf{e}, \qquad (1)$$

where $\delta\beta_{21} = (\delta\beta_2 - \delta\beta_1)/2$ is the difference of the polarization corrections of the TE_{01} and HE_{21} modes, $\tilde{\beta}' = \tilde{\beta} + (\delta\beta_1 + \delta\beta_2)/2$ (here $\tilde{\beta}$ is the propagation constant of the mode with $|l| = 1$ in the scalar approximation, the superscript e designates an even mode, and the $\pm$ sign indicates the direction of circular polarization (the helicity $\sigma = \pm 1$).

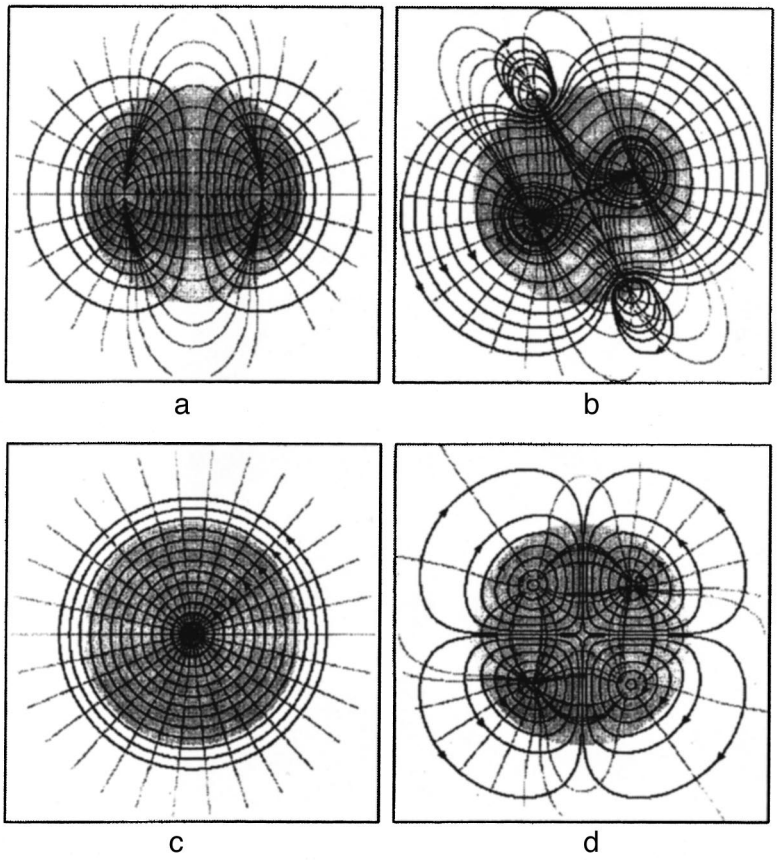

FIG. 1. Pattern of the ''field lines'' of the transverse Poynting vector $\mathbf{P}_t$ for the $CP_{11}^{+,e}$ mode of a stepped-index fiber: a — $\Delta\beta z=0$, b — $\Delta\beta z=\pi/4$; c — $\Delta\beta z=\pi/2$; d — pattern of lines for the LP_{11} mode (the dark lines are the ''field lines'' of $\mathbf{P}_t$, the gray lines are lines of constant pseudopotential).

Using the results of Part I of this series of papers, we write an expression for the transverse components of the Poynting vector and the z component $\mathbf{M}_z$ of the angular momentum of the even mode $CP_{11}^{\pm,e}$ mode as

$$P_\varphi=-2\sigma KF_1(G_1^+ + G_1^-)\cos^2(\varphi-\sigma\delta\beta_{21}z),$$

$$P_r=-\sigma KF_1(G_1^+ - G_1^-)\sin 2(\varphi-\sigma\delta\beta_{21}z),$$

$$\mathbf{M}_z=\rho P_\varphi/c^2, \quad K=a_1^2/2\sqrt{\frac{\varepsilon_0}{\mu_0}}n_{co}\frac{\sqrt{2\Delta}}{V}. \tag{2}$$

Figure 1a shows the pattern of the ''field lines'' and lines of constant pseudopotential for the transverse components $\mathbf{P}_t$ of the Poynting vector. The Magnus effect in these fields is manifested as a rotation of the axis of an edge dislocation according to the equation $\varphi-\sigma\delta\beta_{21}z=\pi/2$ for an even mode and $\varphi-\sigma\delta\beta_{21}z=0$ for an odd mode. The axis of the dislocation of a right-circularly polarized mode is rotated counterclockwise, while that of a left-circularly polarized mode is rotated clockwise.

One can see from expressions (1) and (2) and from Refs. 16 and 17 that the physical manifestation of the angular momentum is due to the helicity σ of the wave. In this case the angular rotation φ of the axis of a dislocation is associated with a flux density of the polarizational angular momentum $\mathbf{M}_s$ (which should not be confused with the spin vector $\mathbf{S}$ of the photon ensemble),[21] which is related to the motion of the maxima of the intensity of the CP mode along a helical trajectory. In each transverse cross section of the fiber the angular momentum density due to the Magnus effect will be zero, although only the flux of the angular momentum density tensor $g_{\nu\mu}$ vanishes in the entire volume of the fiber:[18]

$$\operatorname{div} g_{\nu\mu}=0. \tag{3}$$

2. Let us study the transformation of the angular momentum density in the process of formation of linearly polarized LV vortices from CP modes. Composing the CV and IV vortices from two CP modes: $CV_{\pm 1}^{+}\Rightarrow CP_{11}^{+e}\pm iCP_{11}^{\pm,0}$, $IV_{\mp 1}^{\pm}\Rightarrow CP_{11}^{\pm,e}\mp iCP_{11}^{\pm,0}$, we obtain for the electric field[19]

$$\mathbf{e}_t(CV_{\pm 1}^{+})=\hat{\mathbf{e}}^{+}\exp\{\pm i\varphi\}F_1(R)\exp\{i(\tilde{\beta}'-\delta\beta_{21})z\},$$

$$\mathbf{e}_t(IV_{\mp 1}^{+})=\hat{\mathbf{e}}^{+}\exp\{\mp i\varphi\}F_1(R)\exp\{i(\tilde{\beta}'+\delta\beta_{21})z\}. \tag{4}$$

For this field the Magnus effect does not appear in explicit form. In fact, for the sum of fields which are phase shifted by $\pi/2$ relative to each other and have mutually orthogonal axes of the edge dislocations and rotate at a constant rate, a purely screw dislocation is created. However, for this field there arises an additional phase equal to $\psi_b=-\delta\beta_{21}z$ for the CV vortex and $\psi_b=\delta\beta_{21}z$ for the IV vortex. In its structure this phase corresponds to the Berry topological phase[4] caused by a cyclic variation of the direction of the orthogonal axes of the edge dislocations of the CP^e and CP^o modes. The difference of the Berry topological phase of the vortices is equivalent to the difference of the phase velocities of the waves. The splitting of the phase velocities of orthogonal circularly polarized waves in multimode fibers on account of the combined influence of the optical Magnus effect and the Berry topological phase has been given the name topological bire-

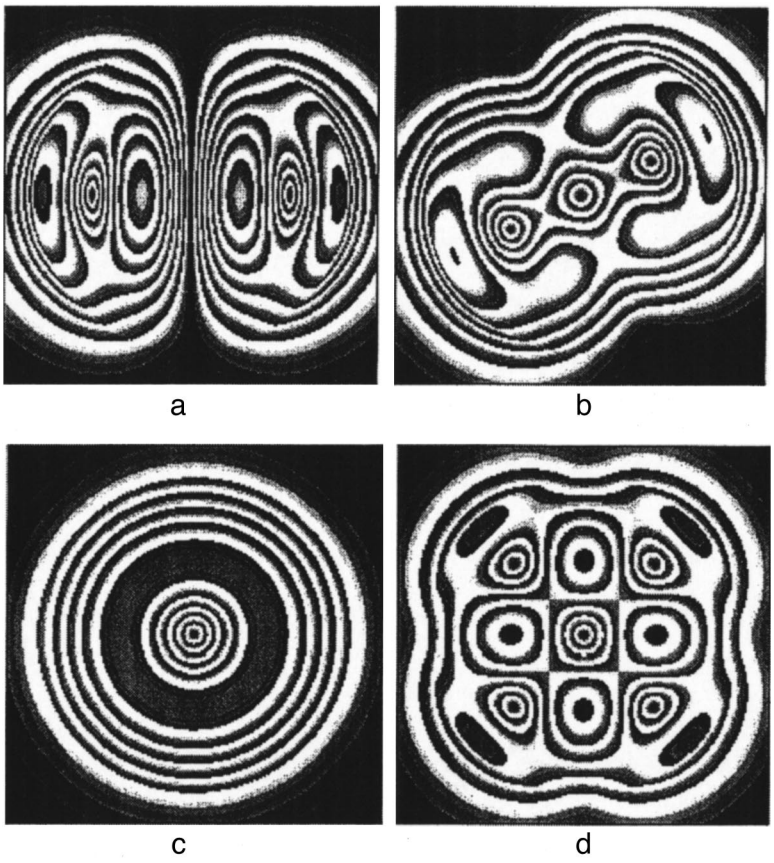

FIG. 2. Level lines $|\mathbf{P}_t| = \text{const}$ for the $CP_{11}^{+,e}$ mode: a — $\Delta\beta z = 0$; b: $\Delta\beta z = \pi/4$; c — $\Delta\beta z = \pi/2$; d — level lines for the LP_{11} mode.

fringence by the present authors.[12,13] The difference of the propagation constants of IV_{+1}^{-} and CV_{+1}^{+} vortices in a fiber with parameters $\rho_0 = 3.5$ μm, $V = 3.6$, $n_{co} = 1.475$ is $2\delta\beta_{21} = 3.50$. Then the value of the topological birefringence is $\Delta n = n^+ - n^- \approx 3.6 \times 10^{-7}$, which is an order of magnitude larger than the results of Ref. 12.

In a parabolic fiber the topological birefringence characterizes the evolution of a linearly polarized LV vortex. This vortex is created as as result of the interaction of all four types of CP modes, e.g.:

$$\mathrm{LV}_{+1}^{x,y} \rightarrow (\mathrm{CP}_{11}^{+,e} + i\mathrm{CP}_{11}^{+,o}) \pm (\mathrm{CP}_{11}^{-,e} + i\mathrm{CP}_{11}^{-,o}) \rightarrow \mathrm{CV}_{+1}^{+} \pm \mathrm{IV}_{+1}, \quad (5)$$

$$\mathbf{e}_t(\mathrm{LV}_1^x) = (\hat{\mathbf{x}}\cos\delta\beta_{21}z + l\hat{\mathbf{y}}\sin\delta\beta_{21}z) \times F_1 \exp\{il\varphi\}\exp\{i\beta' z\}, \quad (l = \pm 1). \quad (6)$$

It follows from expression (6) that the uniformly linearly polarized transverse electric field of an LV vortex undergoes a change of azimuth of the linear polarization $\psi_{\mp} = \pm\delta\beta_{21}z$ which depends on the sign of the topological charge l. This rotation of the linear polarization of the field of an LV vortex is the waveguide analog of the Rytov effect.[5]

The angular momentum and the components of the transverse Poynting vector for an LV vortex in a parabolic fiber can be written in the form

$$P_\varphi = lKF_1(G_1^+ - G_1^-), \quad P_r = 0, \quad M_z = \rho P\varphi/c^2. \quad (7)$$

Since the field of an LV vortex is linearly polarized, the formation of the angular momentum will involve the participation of only the orbital part of the angular momentum, by a mechanism involving the topological charge l.

The rotation of the linear polarization (6) of an LV vortex gives rise to a flux of the angular momentum density tensor, so that condition (3) holds in every volume of the fiber. Unfortunately, in a stepped-index fiber the LV vortex is unstable, and its formation is part of the process of propagation of a CP mode.

3. The phenomenon of rotation of the axis of an edge dislocation (optical Magnus effect) and the rotation of the plane of polarization of the field (Berry topological phase) combine in a single wave process the evolution of a CP mode in a fiber with a stepped refractive index profile. In such a fiber the field of an IV vortex is unstable.[19] As was shown in Ref. 19 and in Part II of the present series of papers, the propagation of an IV vortex in a stepped fiber can be represented as the transfer of energy between the partial vortices $\hat{\mathbf{e}}^+ F_1(R)\exp\{-i\varphi\}$ and $\hat{\mathbf{e}}^- F_1(R)\exp\{+i\varphi\}$. When the energy from the first partial vortex has been transferred completely to the second ($\Delta\beta z = \pi/2 + m\pi$), the fields of the CV and IV vortices, adding together with identical topological charges but with orthogonal polarizations, form an LV vortex. Owing to the differences of the propagation constants of the partial vortices the azimuth of the linear polarization of the vortex will rotate by an angle $\psi = l\delta\beta_{21}z$ ($\lambda = \sigma$).[14] If $\Delta\beta z = m\pi$, then the addition of vortices with identical polarizations but different topological charges will produce a purely edge circularly polarized dislocation, the axis of which is rotated by an angle $\varphi = \sigma\delta\beta_{21}z$.

We calculated the pattern of the ''field lines'' of the Poynting vector $\mathbf{P}_t$ and lines of equal pseudopotential for the $CP_{11}^{+,e}$ mode of a stepped-index fiber (we have omitted the analytical expressions for the components of the Poynting vector on account of their unwieldy form). Figure 1 and 2 show the distribution of the ''field lines'' and modulus of the transverse vector $\mathbf{P}_t$ in different cross sections of the fiber. The transition from a field with a circularly polarized edge dislocation to a field with a linearly polarized screw dislocation is characterized by a changeover from the polarizational part of the angular momentum density to the orbital part.[20] Since a change from $\mathbf{M}_s$ to $\mathbf{M}_l$ occurs on account of a phase shift $\Delta\beta z=\pi/4$, this process can be called conversion of the angular momentum. It should be noted that the difference $\mathbf{M}_s-\mathbf{M}_l\neq 0$ and the momentum defect $\Delta\mathbf{M}$ should be converted to a mechanical torque on the fiber. Figures 1d and 2d show for comparison the analogous patterns for the linearly polarized LP_{11} mode for $\delta\beta_{21}z\neq m\pi/2$. It is seen from the figure that the vector $\mathbf{P}_t$ contains four vortices.

The topological birefringence and angular momentum conversion are indicative of the dynamical unity of the optical Magnus effect and the Berry topological phase in the fields of a few-mode fiber, having their origin in the mode dispersion of the fields of optical waveguides.

[1] B. Ya. Zel'dovich and V. S. Liberman, Kvantovaya Elektron. (Moscow) **17**, 580 (1990) [Sov. J. Quantum Electron. **20**, 427 (1990)].
[2] A. V. Volyar, S. N. Lapaeva, and V. I. Myagkov, Pis'ma Zh. Tekh. Fiz. **18**(8), 53 (1993) [Tech. Phys. Lett. **18**, 261 (1993)].
[3] A. V. Dugin, B. Ya. Zel'dovich, N. D. Kundikova, and V. S. Liberman, JETP Lett. **53**, 197 (1991).
[4] M. Berry, Proc. R. Soc. London, Ser. A **392**, 40 (1984).
[5] S. M. Rytov, Dokl. Akad. Nauk SSSR **28**, 263 (1938).
[6] B. Ya. Zel'dovich and A. A. Esayan, Kvantovaya Elektron. (Moscow) **15**, 235 (1988) [Sov. J. Quantum Electron. **18**, 149 (1988)].
[7] A. V. Bolyar, N. V. Kukhtarev, S. N. Lapaeva, and N. N. Leĭfer, Pis'ma Zh. Tekh. Fiz. **17**(3), 1 (1991) [Sov. Tech. Phys. Lett. **17**, 459 (1991)].
[8] F. I. Fedorov, Dokl. Akad. Nauk SSSR **105**, 465 (1955).
[9] F. I. Fedorov, Zh. Prikl. Spektrosk. **27**, 580 (1972).
[10] Ch. Imbert, Phys. Rev. D **5**, 787 (1972).
[11] V. S. Liberman and B. Ya. Zel'dovich, Phys. Rev. A **46**, 5199 (1992).
[12] A. V. Volyar, Yu. N. Mitsaĭ, B. I. Myagkov, and T. A. Fadeeva, Pis'ma Zh. Tekh. Fiz. **20**(3), 48 (1994) [Tech. Phys. Lett. **20**, 111 (1994)].
[13] A. V. Volyar, A. V. Gnatovskiĭ, and S. N. Lapaeva, Ukr. Fiz. Zh. **37**, 1468 (1992).
[14] A. V. Volyar, T. A. Fadeeva, and Kh. M. Reshitova, Pis'ma Zh. Tekh. Fiz. **23**(5), 14 (1997) [Tech. Phys. Lett. **23**, 175 (1997)].
[15] A. W. Snyder and J. D. Love, *Optical Waveguide Theory*, Methuen Inc., New York (1984) [Radio i Svyaz', Moscow (1987)].
[16] R. A. Bet, Phys. Rev. **50**, 115 (1936).
[17] L. Allen, M. W. Beijersbergen, R. J. Spreeuw, and J. P. Woerdman, Phys. Rev. A **45**, 8185 (1992).
[18] A. A. Sokolov, *Introduction to Quantum Electrodynamics* [in Russian], GIFML, Moscow (1958).
[19] A. V. Volyar, T. A. Fedeeva, and Kh. M. Reshitova, Pis'ma Zh. Tekh. Fiz. **23**(5), 70 (1997) [Tech. Phys. Lett. **23**, 198 (1997)].
[20] M. W. Beijersbergen, L. Allen, II, E. L. O. van der Veen, and J. P. Woerdman, Opt. Commun. **96**, 123 (1993).
[21] N. N. Bogoliubov and D. V. Shirkov, *Introduction to the Theory of Quantized Fields*, 3rd ed., Wiley, New York (1980) [Russian original, Nauka, Moscow (1976)].

Translated by Steve Torstveit

Thickness of the damaged layer along the track made by a high-energy ion in polyimide

A. I. Vilenskiĭ, B. V. Mchedlishvili, V. A. Klyuev, and Yu. P. Toporov

Institute of Crystallography, Russian Academy of Sciences, Moscow;
Institute of Physical Chemistry, Russian Academy of Sciences, Moscow
(Submitted September 3, 1997)
Pis'ma Zh. Tekh. Fiz. **23**, 68–71 (December 12, 1997)

The thickness of the damaged layer along a particle track in polyimide is estimated by the method of thermally stimulated exoelectron emission and found to be ~30 nm. © *1997 American Institute of Physics.* [S1063-7850(97)01212-3]

The process of pore formation and development in polymer track membranes is determined by the degree of structural damage of the polymer and the thickness of the damaged layer around the tracks formed by high-energy ions irradiating the polymer. Here it is very important to determine the thickness of the damaged layer not only for the technology of track membranes but also from the standpoint of general radiation materials science on account of the change in the properties of materials accompanying irradiation. At the same time, the determination of the thickness of the damaged layer is an extremely complex experimental problem.

In Ref. 1 the thickness of the damaged layer in polyimide along the tracks created by argon, krypton, and tungsten ions was estimated on the basis of data on the kinetics of etching of pores in the film. It was found that irradiation causes complete destruction of the polymer in the region where a high-energy ion passes (with a radius of up to 5 nm), and low-molecular products are formed (these are detected by infrared spectroscopy). Around this zone a region with an altered structure of the polymer forms, extending to 35 nm.

However, since there is no sharp transition between the etch rate of the polymer with the altered structure and the etch rate of the unirradiated polymer (possibly in part because of swelling of the polymer in the etchant), it is hard to determine the extent of the damaged layer precisely.

Therefore, in the present study we have attempted to estimate the thickness of the damaged layer along a track in polyimide by a different method, viz., the method of thermally stimulated exoelectron emission. The essence of the technique used is as follows.

The temperature dependence of the intensity of electron exoemission (the so-called ''glow curves'') of polyimide films were taken on a standard apparatus[2] in a vacuum of 10^{-4} Torr before and after the films were subjected to a flux of high-energy ions. The preliminary activation of the films was done in the plasma of a corona discharge in air. The experiments showed that after the irradiation by high-energy ions the character of the glow curve of a film was altered: new peaks appeared due to electron emission from parts of the film where the structure was damaged.

Then the damaged material around the tracks was etched with a specially chosen etchant.[3] In the course of the etching we periodically measured the thermally stimulated exoelectron emission currents from the film. When the character of the glow curve from the irradiated film matched that of the initial film, the thickness of the etched layer at that time was taken to be the thickness of the damaged layer.

The thickness of the etched layer of the polymer was determined from the diameter of the pores on a Tesla BS-340 scanning electron microscope and also by a hydrodynamic method.[4]

As an example, Fig. 1 shows the glow curves of the

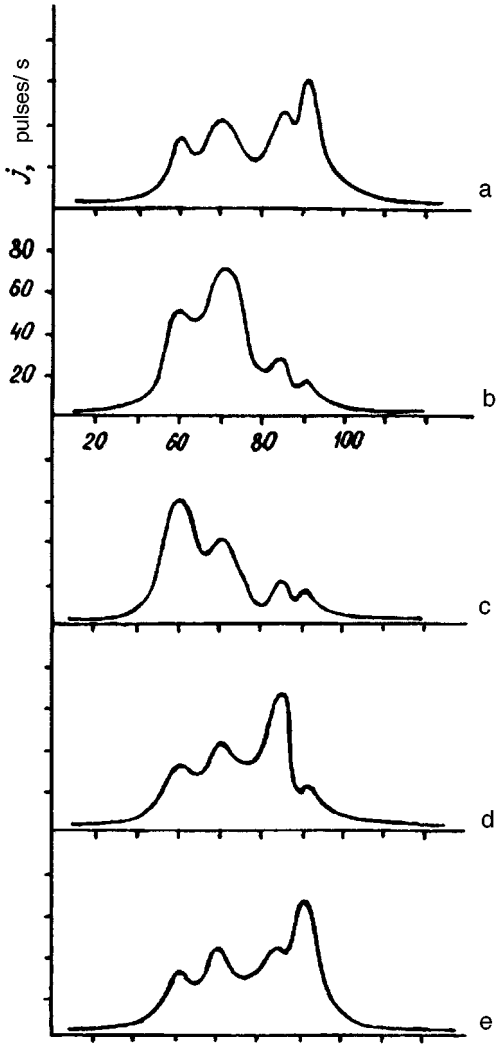

FIG. 1. Glow curves of the thermally stimulated exoelectron emission of an initial polyimide film (a), of a film irradiated by argon atoms (b), of the irradiated film after etching for 10 min (c), 60 min (d), and 200 min (e) in a 30% solution of hydrogen peroxide.

thermally stimulated exoelectron emission of the initial polyimide film (a) and of the same film after irradiation by argon atoms (1 MeV per nucleon at a fluence of 10^7–10^8 cm^{-2}) (b), after etching for 10 min (c), 60 min (d), and 200 min (3) in a 30% solution of hydrogen peroxide. It is seen from the figure that the character of curves (b) and (d) is completely identical, so that one can say that the entire layer of damaged polyimide is etched away after 200 min. Electron microscope studies and hydrodynamic measurements gave a value of the order of 60 nm for the diameter of the pores in the film after a 200-min etch.

Thus the thickness of the damaged layer around a track in polyimide, as determined by thermally stimulated exoelectron emission, is found to be $\sim$30 nm, which is close to the data obtained in Ref. 1 and adds to their reliability.

[1] A. I. Vilenskiĭ, N. G. Markov, V. A. Oleĭnikov *et al.*, Khim. Vys. Energ. **28**, 507 (1994).
[2] V. S. Kortov, A. I. Slesarev, and V. V. Rogov, *Exoemission Monitoring of the Surfaces of Items After Processing* [in Russian], Naukova Dumka, Kiev (1986).
[3] A. I. Vilenskiĭ, V. A. Oleĭnikov, I. V. Kuptsova *et al.*, Khim. Vys. Energ. **28**(4), 326 (1994).
[4] A. I. Vilenskiĭ, V. A. Oleĭnikov, B. V. Mchedlishvili *et al.*, Khim. Vys. Energ. **26**(4), 12 (1992).

Translated by Steve Torstveit

On the nature of the luminescence centers in epitaxial films of zinc telluride

K. V. Solov'ev, B. V. Lisovoĭ, and Yu. A. Mironchenko

Kherson Industrial Institute
(Submitted May 5, 1997)
Pis'ma Zh. Tekh. Fiz. **23**, 72–76 (December 12, 1997)

The luminescence properties of zinc telluride films are studied experimentally. The chemical nature of the luminescence centers of ZnTe epitaxial films is established. © *1997 American Institute of Physics.* [S1063-7850(97)01312-8]

Analysis of published data on the luminescence properties of thin films of zinc telluride shows differences in the results obtained by different authors. For example, in Refs. 1 and 2 the luminescence in ZnTe thin films grown on sapphire is attributed to intrinsic defects or to the presence of uncontrolled impurities. In Ref. 3 a series of luminescence bands was observed in epitaxial films grown by vapor-phase epitaxy (VPE). The chemical nature of the luminescence centers was not investigated in detail. There is practically no information about the properties of ZnTe epitaxial films grown by liquid-phase epitaxy (LPE). The discrepancy of the results as to the position of the bands and the nature of the emission centers suggest that the recombination centers are of a complex nature stemming from the tendency of defects to associate and from the formation of intrinsic defects on account of the self-compensation effect.

The ZnTe epitaxial films investigated in the present study were grown by LPE on single-crystal substrates of ZnSe in an atmosphere of purified hydrogen. The luminescence spectrum of the undoped ZnTe epitaxial films at 77 K exhibited a single band of luminescence with a maximum at around 0.76 μm and a half-width of 0.3 eV (curve *1* in Fig. 1). For comparison, curve *1* in Fig. 2 shows the typical spectral characteristic of undoped ZnTe single crystals. Characteristic bands with maxima in the regions around 0.564, 0.66, and 0.76 μm are observed. Both for the epitaxial films and for the single crystals there is a characteristic absence of luminescence in the edge region of the spectrum, with $\lambda_{max}=0.525$ μm at 77 K. This is indicative of the presence of a large concentration of deep centers of radiative recombination in zinc telluride, both in the epitaxial films and in the single crystals. The presence of such defects in semiconductors ordinarily prevents the appearance of edge luminescence. In studies undertaken to obtain information about the nature of the radiative recombination centers in ZnTe epitaxial films it was found that the luminescence vanished almost completely after processing in saturated Zn vapor or in a Zn melt (curve *2* in Fig. 1). No additional photoluminescence bands arose in other parts of the spectrum. For comparison, curve *2* in Fig. 2 shows the emission spectrum of ZnTe single crystals after annealing under analogous conditions. Annealing leads to suppression of the luminescence bands with $\lambda_{max}=0.564$ and 0.76 μm, while the intensity of the luminescence in the 0.66 μm region remains essentially unchanged.

The change in the spectral distribution of the photoluminescence of ZnTe epitaxial films after annealing in saturated tellurium vapor is illustrated by curve *3* in Fig. 1. It is found that after such a heat treatment a new luminescence band with $\lambda_{max}=1.1$ μm arises, while the emission with $\lambda_{max}=0.76$ μm is suppressed. A similar annealing of single-crystal ZnTe samples suppresses all three luminescence bands obtained in the initial state and, just as in the epitaxial films, gives rise to a luminescence band with a maximum in the infrared part of the spectrum (curve *3* in Fig. 2).

The results described above permit making certain conjectures as to the nature of the defects responsible for the observed bands. When samples are heat treated in liquid zinc or saturated zinc vapor the density of zinc vacancies decreases as they are filled by zinc atoms. The significant de-

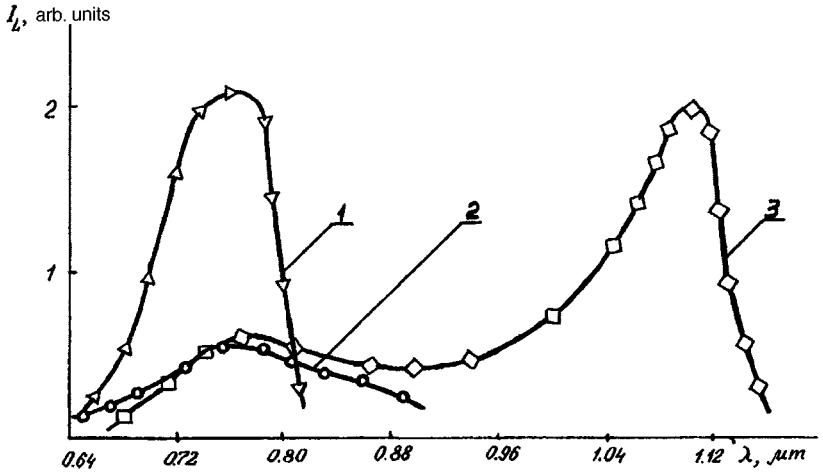

FIG. 1. Photoluminescence spectra of undoped zinc telluride epitaxial films at 77 K: *1* — initial epitaxial film; *2* — epitaxial film after heat treatment in saturated vapor or molten zinc; *3* — epitaxial film after heat treatment in saturated tellurium vapor.

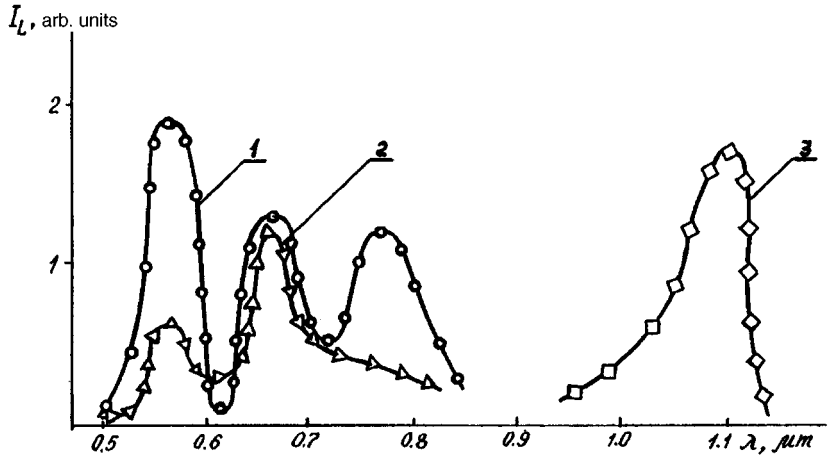

FIG. 2. Photoluminescence spectra of undoped zinc telluride single crystals at 77 K: *1* — initial single crystal; *2* — single crystal after heat treatment in saturated vapor or molten zinc; *3* — single crystal after heat treatment in saturated tellurium vapor.

crease in the intensity of the luminescence in the 0.56 and 0.76 μm regions indicates that vacancies are involved in the formation of the defects responsible for these bands.

The results on the luminescence in the 0.76 μm region for epitaxial ZnTe films show the characteristic features of the band indicated above. For example, after annealing in saturated zinc vapor the luminescence in the 0.76 μm region vanishes, the position of the maximum of this luminescence is practically independent of the temperature of the sample and the intensity of the exciting light, the illuminance–exitance characteristics are close to linear, and the temperature dependence of the intensity of this band is not described by a simple exponential law with an appreciable activation energy. This behavior is characteristic for the so-called self-activated luminescence bands, which have also been observed in other II–VI compounds.[4] The experimental results are suggestive of intracenter radiative transitions which occur between the ground state and an excited state of the complex acceptor $[V_{zn}^{--}-D_{zn}^{+}]^{-}$ and which are describable by a model of configuration coordinates.

The position of the band in the 0.66 μm region for ZnTe single crystals corresponds to luminescence due to recombination of nonequilibrium carriers at the isovalent defect O_{Te} (Refs. 5 and 6). The luminescence of oxygen was not observed in the epitaxial films. This is because of the technological conditions in the growth of the epitaxial films. The increase in the photoluminescence intensity of ZnTe epitaxial films in the 1.1 μm region after heat treatment in saturated tellurium vapor can be accounted for by the appearance of intrinsic defects in the crystal lattice of ZnTe. Indeed, such a heat treatment of both the films and single crystals give rise to stoichiometric tellurium on account of the unidirectional deviation of the homogeneity region of the compound to the side of excess Te. Here the formation of intrinsic defects Te_i can occur.[7] In II–VI compounds interstitial atoms of Te, like those of other chalcogenides, form acceptor levels which are displaced from the upper edge of the valence band by 0.1–0.15 eV and act as centers of radiative recombination.

The luminescence with $\lambda_{max}=1.1$ μm is subject to temperature quenching with an activation energy of 0.12 eV. Here the luminescence can be observed only at low temperatures (below 150 K). This confirms the finding that the luminescence center is located near the band edge and is in good thermal interaction with the band.

Photomicrographs of ZnTe epitaxial films in the as-grown state and after annealing in saturated Te vapor reveal the presence of some tiny inclusions which look like dark spots. Similar results were obtained for the ZnTe single crystals. It has been established that these inclusions are accumulations of excess tellurium.[8] Near these dark microinclusions there is practically no photoluminescence — they are obviously surrounded by regions of efficient nonradiative recombination.[9] It is apparently for this reason that the integrated luminescent intensity of ZnTe epitaxial films and single crystals decreases after annealing in tellurium. At the same time one observes an increase in the dark conductivity and extrinsic photosensitivity after heat treatment of the epitaxial films in saturated tellurium vapor.

In summary, a comprehensive investigation of the luminescence properties of zinc telluride epitaxial films in comparison with the analogous properties of ZnTe single crystals, including a study of heat treatment in media which alter the stoichiometry, has revealed the chemical nature of the luminescence centers in ZnTe epitaxial films.

[1] É. A. Senokosov, V. G. Stoĭkova, and A. N. Usatyĭ, Izv. Akad. Nauk SSSR, Ser. Fiz. **1**, 69-71 (1983).
[2] É. A. Senokosov, V. G. Stoĭkova, and A. N. Usatyĭ, and M. V. Chukichev, Sov. Phys. Semicond. **18**, 700 (1984).
[3] A. V. Tsurkan and S. P. Medvetskiĭ, Zh. Prikl. Spektrosk. **41**, 726 (1984).
[4] D. D. Nedeoglo and A. V. Simashkevich, *Electrical and Luminescent Properties of Zinc Selenide* [in Russian], Shtiintsa, Kishinev (1984), p. 86.
[5] B. V. Lisovoĭ and I. I. Ponomarenko, Zh. Tekh. Fiz. **64**(8), 190 (1994) [Tech. Phys. **39**, 852 (1994)].
[6] C. B. Norris, J. Appl. Phys. **53**, 5172 (1982).
[7] D. Bensahel, M. Dupuy, and I. C. Pfisher, Phys. Status Solidi A **55**, 211 (1979).
[8] P. J. Dean, J. Lumin. **21**, 75 (1979).
[9] N. Magnea, D. Bensahel, and I. C. Pfisher, Solid State Commun. **29**, 35 (1979).

Translated by Steve Torstveit

Monte Carlo calculation of the low-temperature mobility of two-dimensional electrons in a quantum well in a selectively doped GaAs-based heterostructure

V. M. Borzdov, S. G. Mulyarchik, and A. V. Khomich

Belorussian State University, Minsk
(Submitted December 30, 1996)
Pis'ma Zh. Tekh. Fiz. **23**, 77–83 (December 12, 1997)

The feasibility of Monte Carlo calculations of the mobility of two-dimensional electrons in a square quantum well in GaAs/AlGaAs heterostructures in a low electric field $E=100$ V/m is demonstrated and results are presented for temperatures of 4.2 and 77 K. The dependence of the mobility on the width of the potential well and on the surface density of charge carriers is determined. © *1997 American Institute of Physics.* [S1063-7850(97)01412-2]

The transport of two-dimensional (2D) electrons in the quantum wells of selectively doped GaAs-based heterostructures has been studied, and very intensively, for quite some time now. Since heterostructures of this kind are now finding wide use in modern integrated electronics, such studies are acquiring practical importance in addition to purely theoretical interest. For temperatures and electric fields in the ranges in which several lower energy subbands are populated the Monte Carlo technique is known to be an efficient method for studying transport processes in quasi-2D semiconductor structures (see, e.g., Refs. 1–5). At the same time, we know of no Monte Carlo calculations of the electron mobility in selectively doped GaAs heterostructures in the case of low temperatures, low electric fields, and degeneracy of the 2D electron gas, when only the lowest subband is populated by electrons and the so-called quantum limit is realized.

In the present paper we demonstrate the feasibility of using the Monte Carlo method to calculate the mobility μ of 2D electrons in square quantum wells in GaAs/spacer-layer/AlGaAs heterostructures in a low electric field $E=100$ V/m and we present results of such a calculation for temperatures of 4.2 and 77 K, showing the dependence of μ on such parameters as the width L of the potential well and the surface density N_s of charge carriers. Here it was assumed that all the conduction electrons are found in the lowest subband, with a bottom energy of E_0 (Ref. 6).

The average mobility μ was calculated on the assumption that the average drift velocity $v_{\rm dr}$ of the electrons is related linearly with the electric field E (Ref. 7), and scattering on background and remote impurity centers and on the surface roughness of the semiconductor was taken into account.

The theoretical analysis of impurity scattering of 2D electrons in square quantum wells has been the subject of a number of papers, among which Refs. 8–10 deserve special mention. Here we have used the results of Ref. 10 in calculating the intensities for impurity scattering.

The scattering intensity for 2D electrons on an ionized impurity can be written in the general form

$$W_I=\frac{m^*}{\hbar^3\pi}\int_0^{\pi}\frac{z^2e^4B(q)}{(2\varepsilon_0\varepsilon_s)^2[q+SH(q)]^2}\,d\theta, \tag{1}$$

where m^* is the effective mass of the electron, which is equal to $0.067m_0$, where m_0 is the mass of a free electron, e is the electron charge, $\hbar$ is the reduced Plank's constant, ε_0 is the permittivity of free space, ε_s is the dielectric constant of the medium ($\varepsilon_s=12.9$ for the GaAs/AlGaAs system),[1] ze is the ion charge, $q=2k\sin\theta/2$, k is the modulus of the electron wave vector, θ is the scattering angle, and S is the screening parameter, which has the form[10]

$$S=\frac{e^2m^*}{2\varepsilon_0\varepsilon_s\pi\hbar^2}\,\frac{1}{1+\exp[(E_0-E_f)/k_bT]}. \tag{2}$$

In Eq. (2) k_b is Boltzmann's constant and T is the temperature. In the present study it was assumed that $E_0=0$ and that the Fermi energy is given by $E_f=\pi\hbar^2N_s/m^*$. Explicit expressions for the form factor $H(q)$ and for the form factors for a background impurity B_{Ib} and for a remote impurity B_{Ir} are given in Ref. 10 (where a mistake made in Ref. 8 has been corrected).

The electron wave function $\psi(z)$, where the direction of z is from the heterointerface into the interior of the GaAs layer, is written

$$\psi(z)=\sqrt{\frac{2}{L}}\sin\left(\frac{\pi z}{L}\right),\quad 0\leqslant z\leqslant L, \tag{3}$$

where L is the width of the square potential well.

The scattering intensity on surface roughness was calculated for the formula[9,11]

$$W_{sr}=\frac{\pi^4\hbar\Delta^2\Lambda^2}{2m^*L^6}\int_0^{2\pi}\frac{\exp(-q^2\Lambda^2/4)}{[1+SH(q)/q]^2}\,d\theta, \tag{4}$$

where Δ is the average height of the asperities on the surface and Λ is the average distance between them.

To determine the current values of the scattering angle θ, which must be randomly chosen for each scattering event from the distributions $P(\theta)d\theta\propto B(q)d\theta/[q+SH(q)]^2$ and $P(\theta)d\theta\propto\exp(-q^2\Lambda^2/4)d\theta/[1+SH(q)/q]^2$, we used the sampling method of Ref. 12. For the choice of final states we took into account the fact that both the impurity scattering and the scattering on the surface roughness occur by elastic scattering mechanisms.

The low-temperature mobility of the 2D electron gas was calculated by the single-particle Monte Carlo method, since the scattering intensities and their angular distributions

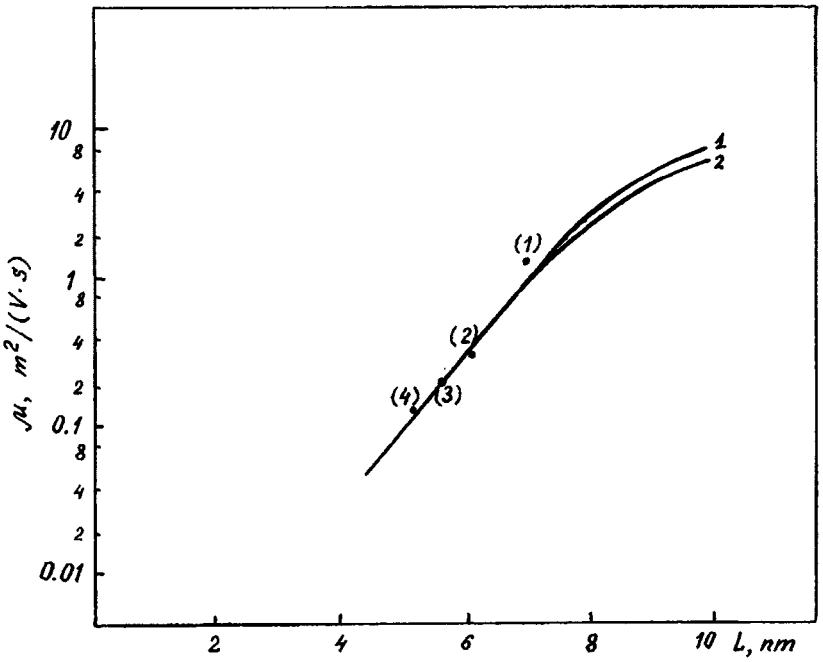

FIG. 1. Dependence of the electron mobility μ on the width L of the quantum well: *1* — $T=4.2$ K, *2* — $T=77$ K. The values of the other parameters used in the calculation are given in the text. The points are the experimental data of Ref. 11.

were such that for a sufficiently large number N of collisions ($N>10^5$) there occurs a stable convergence of the electron energy to a definite value for a specified electric field E. The necessity of providing a large selection volume N stems from the fact that the accuracy of the Monte Carlo method is known to fall off with decreasing temperature, since the electron drift velocity becomes small compared to the thermal speed.[12] In addition, because the electron gas is degenerate under the conditions studied, the Pauli exclusion principle was taken into account by including in the overall algorithm of the simulation a procedure (which was proposed in Ref. 13 for degenerate semiconductors) in which the occupancy of an electron state is checked after each scattering event selection.

Using the above algorithm, we calculated the dependence of the mobility μ on the parameters L and N_s for a quantum well in the structure GaAs/AlAs/$Al_{03}Ga_{07}As$. Figure 1 shows the results of a calculation of $\mu(L)$ at the temperatures $T=4.2$ K and $T=77$ K in an electric field $E=100$ V/m. The surface electron density N_s was taken as $N_s=3\times10^{15}$ m^{-2}, the volume densities of background and remote impurities were taken as $N_{Ib}=10^{20}$ m^{-3} and $N_{Ir}=10^{24}$ m^{-3}, the thicknesses of the spacer layer and doped layer were $l_{sp}=6$ nm and $l_d=80$ nm, respectively, and the other parameters were $\Delta=0.4$ nm and $\Lambda=11$ nm. Also shown for comparison are the experimental data of Ref. 11, which were obtained by measuring the Hall mobility at $T=4.2$ K for the same parameters N_{Ir}, l_{sp}, and l_d at four

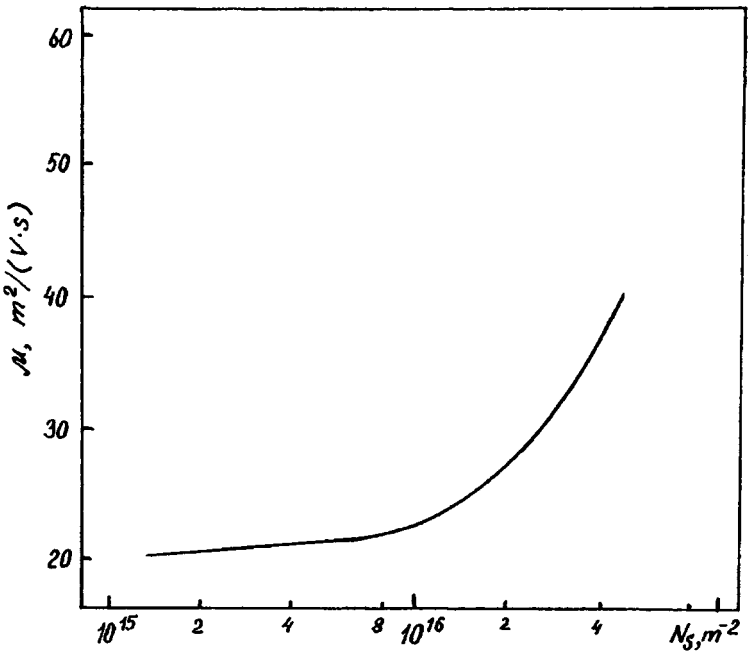

FIG. 2. Dependence of the electron mobility μ on the surface electron density N_s. The values of the parameters used in the calculation are given in the text.

points: $N_{s1}=4.3\times10^{15}$ m^{-2} (point *1*), $N_{s2}=1.9\times10^{15}$ m^{-2} (*2*), $N_{s3}=3.2\times10^{15}$ m^{-2} (*3*), and $N_{s4}=3.1\times10^{15}$ m^{-2} (*4*) for a quantum well with the same structure. The good agreement seen in Fig. 1 between the experimental data and the calculated curve for the chosen values of the parameters Δ and Λ indicates that the numerical model used is sufficiently realistic for the transport processes that occur in the quantum well under study. The slight decrease in the mobility when the temperature is raised from 4.2 to 77 K is due to the slight decrease in the screening parameter S according to Eq. (2) and to the corresponding increase in the overall intensity of the scattering of the 2D electrons in accordance with Eqs. (1) and (4).

We note that in Ref. 11 the experimental points *1*, *2*, *3*, and *4* were approximated by straight lines with the parameters $\delta=0.283$ nm, $\Lambda_1=5$ nm, and $\Lambda_2=7$ nm on the assumption that the dominant scattering mechanism in the well under discussion is scattering on the roughness of one interface. However, as the authors of Ref. 11 themselves noted, such an approximation is valid only for narrow wells with $L<6$ nm. Since in the present paper we are taking into account impurity scattering as well as scattering on interfacial roughness, the approximating curves *1* and *2* in Fig. 1 differ markedly from straight lines for values $L>6$ nm, and the adjustable parameter Λ is larger than the values used in Ref. 11.

As a second example, Fig. 2 shows $\mu(N_s)$ calculated for a GaAs/undoped-AlGaAs/AlGaAs well at $T=4.2$ K and $E=100$ V/m for the parameters $L=10$ nm, $N_{Ib}=10^{22}$ m^{-3}, $N_{Ir}=2\times10^{24}$ m^{-3}, $l_{sp}=10$ nm, $l_d=50$ nm, $\Delta=0.3$ nm, and $\Lambda=6$ nm. The monotonic increase in the mobility with increasing N_s can be explained by a corresponding increase in the Fermi energy E_f and, hence, of the screening parameter S, and this ultimately decreases the electron scattering intensity and increases the electron mobility.

Thus we have demonstrated that the Monte Carlo method can be used efficiently to calculate the mobility of a degenerate 2D electron gas at low temperature in a quantum well of a selectively doped GaAs-based heterostructure under conditions corresponding to the electrical quantum limit. The main advantage of this approach is the possibility of including any number of important scattering processes in the overall algorithm of the simulation, regardless of the complexity of their model description, and of obtaining numerical estimates of the mobility and other kinetic parameters characterizing the transport of 2D electrons under these conditions.

[1] K. Yokoyama and K. Hess, Phys. Rev. B **33**, 5595 (1986).
[2] M. Al-Mudares and B. K. Ridley, J. Phys. C **19**, 3179 (1986).
[3] N. Z. Vagidov and V. M. Ivashchenko, Ukr. Fiz. Zh. **37**, 781 (1992).
[4] M. V. Fischetti and S. E. Laux, Phys. Rev. B **48**, 2244 (1993).
[5] V. M. Borzdov, M. M. Vrubel', O. G. Zhevnyak, and F. F. Komarov, Pis'ma Zh. Tekh. Fiz. **21**(7), 69 (1995) [Tech. Phys. Lett. **21**, 272 (1995)].
[6] M. Shur, *GaAs Devices and Circuits*, Plenum Press, New York (1987) [Russian transl., Mir, Moscow (1991)].
[7] P. K. Basu, Appl. Phys. Lett. **48**, 350 (1977).
[8] J. Lee, H. N. Spector, and V. K. Arora, J. Appl. Phys. **54**, 6995 (1983).
[9] A. Gold, Phys. Rev. B **35**, 723 (1987).
[10] J. L. Thobel, L. Baudry, F. Dessenne, M. Charef, and R. Fauquembergue, J. Appl. Phys. **73**, 233 (1993).
[11] H. Sakai, T. Noda, M. Hirakawa, M. Tanaka, and T. Matsusue, Appl. Phys. Lett. **51**, 1934 (1987).
[12] C. Jacoboni and L. Reggiani, Rev. Mod. Phys. **55**, 645 (1983).
[13] S. Bosi and C. Jacoboni, J. Phys. C **9**, 315 (1976).

Translated by Steve Torstveit

Observation of large-scale hydrodynamic structures in a vortex tube and the Ranque effect

V. A. Arbuzov, Yu. N. Dubnishchev, A. V. Lebedev, M. Kh. Pravdina, and N. I. Yavorskiĭ

Institute of Thermal Physics, Siberian Branch of the Russian Academy of Sciences, Novosibirsk
(Submitted July 30, 1997)
Pis'ma Zh. Tekh. Fiz. **23**, 84–90 (December 12, 1997)

The existence of large-scale structures in the form of a vortical double helix in a swirling Ranque flow is observed for the first time. The structure of the vortical double helix is visualized in real time by the method of Hilbert bichromatic filtering. The experimental result is interpreted on the basis that the most probable physical mechanism for the spatial energy separation in the gas flow (i.e., for the so-called Ranque effect) is viscous heating of the gas in a thin boundary layer at the walls of the vortex chamber and the adiabatic cooling at the center owing to the formation of an intense vortex braid near the axis. © *1997 American Institute of Physics.* [S1063-7850(97)01512-7]

The Ranque effect is a surprising phenomenon that has been known for a very long time,[1] but it has still not been given an adequate physical explanation. The main puzzle in the Ranque effect is the mechanism for the onset of a substantially nonuniform distribution of the stagnation enthalpy in a strongly swirled gas flow. Actually, over short times of the order of 0.1 s there occurs a significant redistribution of thermal energy in space, and one is dealing with an actually operative Maxwell's demon. There have been many attempts to explain this phenomenon,[2–4] but they are all quite far from reality. It is well known that sufficient conditions for constancy of the stagnation enthalpy are as follows (the Bernoulli theorem): 1) the flow must be steady, 2) the forces of viscous friction in the gas (liquid) must be inconsequential, 3) the heat exchange between fluid particles must be negligible. It should be said that the violation of the steady flow condition does not in itself cause spatial separation of the heat content, since a simple permutation of the fluid particles without a corresponding exchange of energy between them does not alter the enthalpy. Nevertheless, nonsteady flow models give good quantitative agreement with experiment as to the kinematics of the flow.[3] Attempts to take viscous forces into account were undertaken in Refs. 2 and 4. It has become the accepted point of view that the process of energy separation is effected by some sort of heat engine in the flow.[2,5] It should be noted that this hypothesis is inconsistent with the assumption that the process is adiabatic, which holds to good accuracy on large scales of the flow.

At the present time there are sufficient grounds for assuming that large-scale vortex structures play a fundamental role in the Ranque effect[6] and, in particular, in the operation of the hypothesized heat engine. To elucidate the role of these structures we have attempted to make an experimental observation of the hydrodynamic structures in a Ranque vortex tube.

We assembled an apparatus for visualizing the large-scale structures in an aerodynamic flow. The method of color Hilbert visualization of the phase fields of the optical density of swirling flows was used, with provisions for compensating the optical distortions due to the stationary temperature gradients.[7] A working model of the visualizer was built, with a field of view 100 mm in diameter. The optical signal was detected by a fast video camera and sent to a data processing system based on a personal computer for determination of the structural and kinematical parameters of the process under study.

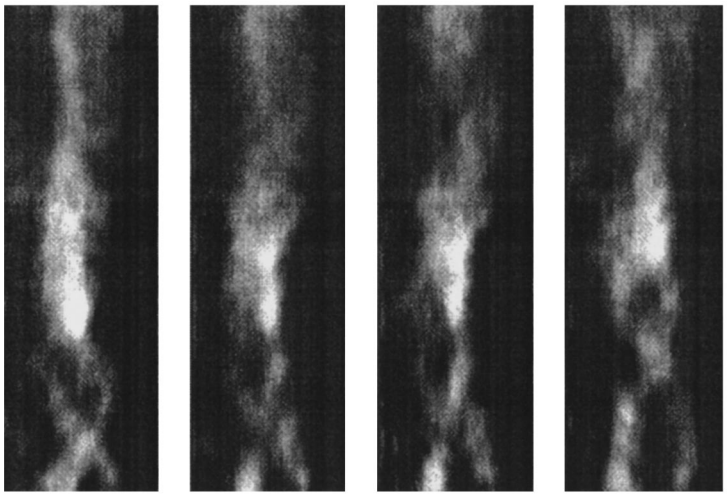

FIG. 1. Visualization of large-scale vortex structures in the form of a double helix. The exposure time of each frame is 250 μs. What is visualized is the gradient of the phase field of the optical density. The pressure at the inlet to the channel is 0.6 MPa, the total air flow rate is 4.5×10^{-2} kg/s; the change in temperature at the ''cold'' and ''hot'' outlets is 33.9 and 1.6 K, respectively; the ratio of the flow rate at the ''cold'' outlet to the total flow rate is 0.26; the adiabatic cooling efficiency is 0.3.

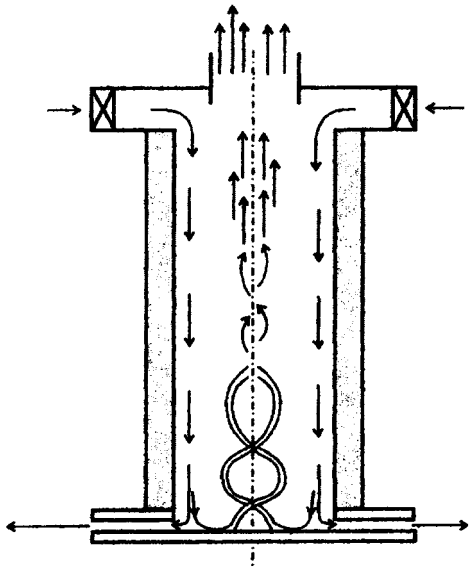

FIG. 2. Diagram of the flow in a Ranque vortex tube.

As the object of study we chose a vortex channel of square cross section with transparent walls, in which a swirling flow, similar to the flow in a Ranque tube, was arranged. At the ''cold'' end air was swirled in a slotted swirler. The ''hot'' end was made in the form of a radial diffuser.

The gradient of the phase field of the optical density in the transverse and longitudinal directions of the vortex channel was visualized in real time with a minimum exposure time of 250 μs in various dynamical regimes.

We established the existence of large-scale structures, with lifetimes an order of magnitude longer than the exposure time. We observed for the first time a vortical double helix (Fig. 1) which is nucleated at the flat end surface around the peripheral hot air outlet and then propagates along the longitudinal axis, repeatedly reclosing and breaking up. In the midsection of the device one can make out only individual fragments of this structure. We detected the rotational motion of the vortical helix. The presence of helical structure is evidence of an intense return current along the axis of the flow. As has been shown by calculations of a similar type of flow,[8] the streamlines can be represented schematically in the following way (Fig. 2). A strongly swirled flow from the swirler moves along the walls of the tube, and then a small part of the flow (hot air) leaves the device, while the majority of the flow is directed toward the center, significantly increasing the vorticity (by virtue of of conservation of the circulation of the velocity along a contracting contour lying perpendicular to the axis of the flow), and that is what causes the vortical double helix. It should be noted here that the vortical helix occupies the central part of the device and does not appreciably affect the viscous boundary layer at the wall. Under our conditions the Reynolds number Re is 10^5 or slightly higher, and the thickness δ of the boundary layer is around 1 mm. After this the air along the axis moves in the reverse direction and exits through openings in the swirler (cold air).

At an overall pressure drop of 4–5 atm the flow velocity of the gas in the vortex tube is tens of meters per second (up to 80 m/s). At a width of the tube of 3.4 cm and a length of up to 1 m, the residence time of a particle in the tube should not exceed 0.1 s (the longitudinal velocity is not over 10 m/s). Measurements show that the drop of the stagnation temperature at the exit from the vortex tube is 14 K. It is easy to calculate that in order for a stagnation temperature difference of 14 K to arise in 0.1 s it is necessary to have a drop in the air temperature of the order of 20 000 K (!) over a distance of around 4 cm (the transverse size of the tube). In actuality it would be hard to expect temperature drops of more than 100 K inside the tube; these would arise mainly on account of adiabatic cooling and heating of the gas. It is easy to find the characteristic size over which a heating of the air by 14 K will occur at a temperature difference of 100 K. It comes to around 1 mm. Thus in order for a heat engine to be operating, it would be necessary to have local temperature gradients of the order of 10^5 K/m in the system. The actual physical model must in turn explain how such large thermal loads arise in the flow. One can propose the following four mechanisms of energy separation in a hydrodynamic flow as being the most likely: 1) in the breakup of the large-scale vortex structure, a large number of small-scale (1 mm) localized vortices of high intensity are formed, and over the characteristic dimensions of these vortices there is convective energy exchange between the fluid particles and a subsequent separation of these particles on large spatial scales; 2) there is a substantial barothermal conductivity effect (i.e., the transfer of heat owing to a pressure gradient) in the hydrodynamic system; 3) one must take into account the heat exchange between the gas and the walls of the vortex tube; 4) heating of the gas due to viscous dissipation of kinetic energy plays an important role.

In order for the first mechanism to be realized it is necessary that the vortex structure break up all the way to very small scales over short hydrodynamic times. In principle this can happen if the phenomenon of vortex breakdown, i.e., decay of the vortex, is present in the hydrodynamic system. However, the question arises as to the mechanism of the separation that would cause the colder particles to collect at the center of the chamber and the hotter particles at the periphery. On the other hand, the phenomenon of barothermal conductivity (the second mechanism) has been studied very little. To all appearances it is insignificant in ordinary process of heat and mass transfer. In any case one cannot expect that the corresponding kinetic coefficient will be much higher than the ordinary thermal conductivity. The third mechanism, thermal contact of the gas flow with the surrounding walls, requires a more detailed examination.

We note first of all that the Prandtl number for air is around 0.7, so that the thickness of the thermal boundary layer will be approximately of the same order of magnitude as the hydrodynamic boundary layer, i.e., around 1 mm. Thus we see that the main thermal load can be concentrated in a viscous boundary layer. Further, the velocity of the gas in the boundary layer is considerably lower than the velocity of the main flow, so that the time of thermal contact of the air particles with the wall is several times greater than the estimate of 0.1 s. It follows that in order to have a substantial

change in the temperature of the gas the temperature drop between the wall and the gas may be only a few tens of degrees. The effect of heat exchange with the wall has been observed experimentally by other investigators,[2] but it has not been directly linked to thermal processes in the boundary layer.

In the boundary layer an intense dissipation of kinetic energy occurs, which can strongly heat the gas over characteristic times of a few tenths of a second. Let us estimate the amount of viscous heating. We have

$$\frac{\Delta T}{\tau} \cong \frac{\nu}{2c_p}\left(\frac{\partial v_i}{\partial x_j}+\frac{\partial v_j}{\partial x_i}\right)^2 \cong \frac{\nu}{2c_p}\frac{u^2}{\delta^2} \cong \frac{T}{2}\frac{u^2}{c_pT}\frac{\nu}{\delta^2}$$

$$\cong \frac{T}{2}\frac{u^2}{c_pT}\frac{u}{25l} \cong \frac{T}{2}\mathrm{M}^2\frac{u}{25l}, \qquad (1)$$

where T is the absolute temperature of the air at the entrance to the device ($\sim$300 K), τ is the residence time of a particle in it ($\sim$0.1 s), M is the Mach number ($\mathrm{M}^2\sim 0.1$), u is a characteristic velocity ($\sim$100 m/s), l is a characteristic dimension ($\sim$4 cm), and $\delta = 5l/\mathrm{Re}^{1/2}$ is the thickness of the boundary layer. It follows that the increase in the stagnation temperature of the air owing to viscous heating can amount to around 150 K if one neglects heat exchange of the gas of the boundary layer with the walls of the vortex tube and with the turbulent swirling flow outside the boundary layer. As we have said, in our experiments the increase in the stagnation temperature was around 14 K, which is an order of magnitude lower than the estimate and is indicative of very intense heat exchange between the boundary layer and the main turbulent gas flow, which, like heat exchange with the wall, has a deleterious influence on the Ranque effect. Thus we see that taking the viscous heating of the gas into account in principle solves the problem of the energy separation. We should add that in our experiments the dimensions of the gap through which the hot air escaped were varied. It was found that the maximum effect was achieved when the width of the gap was equal to the thickness of the boundary layer, which confirms the conclusion made above.

In addition to heating of the gas, an important element of the Ranque effect is the cooling of the main flow to appreciable negative temperatures. This could be explained if the region near the axis of the flow is a zone of rarefaction substantially greater than that which would arise as a result of the rotational motion of the gas due to the near-wall jet flows emerging from the swirler. This is possible if there is an intense vortex structure at the center of the tube, as we have in fact observed experimentally. The presence of a region of high concentration of vorticity near the axis causes a significant lowering of the pressure in it and, hence, adiabatic cooling of the gas moving outside the boundary layer. As a result the gas temperature falls off significantly in the paraxial region, as is indeed attested to by the emergence of cold gas through the central opening in the swirler.

On the basis of what we have said, we can conclude that the most likely physical mechanism responsible for the spatial energy separation in the gas flow (the Ranque effect) is viscous heating of the gas in a thin boundary layer at the walls of the vortex chamber and the adiabatic cooling of the gas at the center on account of the formation of an intense vortex braid near the axis; in this paper we have observed this structure for the first time.

This study was supported by the Russian Fund for Fundamental Research.

[1] G. L. Ranque, J. Phys. Radium **14**, 1125 (1933).
[2] A. P. Merkulov, *Vortex Effect and Its Application in Technique* [in Russian], Mashinostroenie, Moscow (1969).
[3] S. V. Alekseenko and V. L. Okulov, Teplofiz. Aéromekh. **3**(2), pp. 101–138.
[4] M. A. Gol'dshtik, *Vortex Flows* [in Russian], Nauka, Novosibirsk (1981).
[5] R. G. Deissler and M. Perlmutter, Int. J. Heat Mass Transf. **1**, 173 (1959).
[6] S. V. Lukachev, Inzh.-Fiz. Zh. **41**, 784 (1981).
[7] V. A. Arbuzov and Yu. N. Dubnistchev, Opt. Laser Technol. **23**, 118 (1991).
[8] N. I. Yavorskiĭ and M. V. Bashkatov, Zh. Tekh. Fiz. **66**(4), 45 (1996) [Tech. Phys. **41**, 320 (1996)].

Translated by Steve Torstveit

Excitation of a quasi-plane shear wave by a surface acoustic source producing normal stresses

A. P. Kiselev, E. Krylova, and L. Yu. Fradkin

Institute of Mechanical Engineering Problems, Russian Academy of Sciences, St. Petersburg, Russia; South Bank University, London, U.K.

(Submitted March 24, 1997)
Pis'ma Zh. Tekh. Fiz. **23**, 91–94 (December 12, 1997)

The generation of elastic volume waves by a source which is widely used in acoustic flaw detection is considered. This source produces normal stresses at the boundary of an elastic solid. The source is large compared to the wavelength of the waves that are launched. The possibility of exciting a shear wave with a plane front in the near zone is established, and an estimate of its intensity is made. © *1997 American Institute of Physics.*
[S1063-7850(97)01612-1]

The fronts of the volume waves excited by an acoustic source producing in-phase oscillations of the normal stress at the boundary of an isotropic and homogeneous elastic solid are illustrated in Fig. 1. These are the familiar[1–3] longitudinal and shear edge waves, bow waves, quasi-plane longitudinal, and quasi-plane shear waves, the wave front of the last-named being shown by a dashed line. Here we point out the possibility that such a wave exists, elucidate the mechanism for its generation, and estimate its intensity.

1. The essence of the matter at hand can be grasped from an analysis of a two-dimensional linear model in the case of a process which is harmonic in time. The displacement $\mathbf{u}(x,z)e^{-i\omega t}$ of an elastic half space in the plane (x,z) is described by the equation

$$\frac{1}{k^2}\nabla(\nabla\cdot\mathbf{u})-\frac{1}{\varkappa^2}\nabla\times(\nabla\times\mathbf{u})+\mathbf{u}=0,\quad z>0, \tag{1}$$

where k and $\varkappa$ are the wave numbers of the longitudinal and shear waves. The source is modeled by specifying the tangential and normal stresses at $z=0$ in the form $\sigma_{xz}=0$ and

$$\sigma_{zz}=\begin{cases} p(x)e^{-i\omega t}, & |x|\leqslant L,\\ 0, & |x|>L, \end{cases} \tag{2}$$

where $p(x)$ is the distribution of the amplitude of the load on the source. The process is independent of the coordinate y. Particular attention has historically been paid to the case $p=\text{const}$.

2. We express the solution of our problem in terms of the solution $\mathbf{G}(x-\xi,z)$ of the classical Lamb problem, where at the point $x=\xi$ of the boundary one specifies a point vertical load $p(x)=\delta(x-\xi)$. Clearly

$$\mathbf{u}(x,z)=\int_{-L}^{L}\mathbf{G}(x-\xi,z)p(\xi)d\xi. \tag{3}$$

The shear part of $\mathbf{G}$ (we are not interested in the longitudinal part) has the form[4]

$$\mathbf{G}^S(x-\xi,z)=\nabla\times(\mathbf{e}_y\psi), \tag{4}$$

where $\mathbf{e}_y$ is the unit vector along the y axis, and $\psi=\psi(x-\xi,z)$ is the corresponding transverse potential. For the shear field $\mathbf{u}^S$ of the source we have

$$\mathbf{u}^S=\nabla\times(\mathbf{e}_yI),\quad I=\int_{-L}^{L}\psi(x-\xi,z)p(\xi)d\xi. \tag{5}$$

3. At a depth of several wavelengths, $\varkappa z\gg 1$, one has[4] at observation angles θ which are not too large (specifically, subcritical)

$$\psi(x-\xi,z)=\frac{\exp(i\varkappa r)}{\sqrt{r}}g(\theta)\left(1+O\left(\frac{1}{\varkappa r}\right)\right). \tag{6}$$

Here $r=\sqrt{(x-\xi)^2+z^2}$, $\sin\theta=x\xi/r$, and $g(\theta)$ is the directional pattern of the shear wave. At first we require only the property (which follows from the symmetry of the Lamb problem) that the directional pattern vanishes beneath the source,

$$g(0)=0. \tag{7}$$

4. We consider a source which is long compared to the shear wavelength, $\varkappa L\gg 1$. We will address the most interesting case for flaw detection, that of the near field of the source:

$$(\varkappa L)^2\gg\varkappa z\gg 1. \tag{8}$$

The contribution to the integral (5) from the rapidly oscillating function ψ comes from the ends of the interval $\xi=\pm L$ (they describe edge waves) and also from the point of stationary phase, $\xi=x$, provided that it lies within the interval. In accordance with the standard method of stationary phase, we expand the integrand in the neighborhood of the stationary point as

$$\psi(x-\xi,z)\approx\frac{\exp(i\varkappa z)}{\sqrt{z}}g\left(\frac{\eta}{z}\right)p(x+\eta)\exp\left(i\varkappa\frac{\eta^2}{2z}\right), \tag{9}$$

$$\eta=\xi-x.$$

As a consequence of Eq. (7) the contribution of the stationary point in leading order is zero. Moreover, for the case of constant p it can be shown that it vanishes in all orders, since in the higher terms of the expansion refining Eq. (6) the amplitude is odd in η, while the phase is even. 5. We now assume that the load is not constant along the source. Near

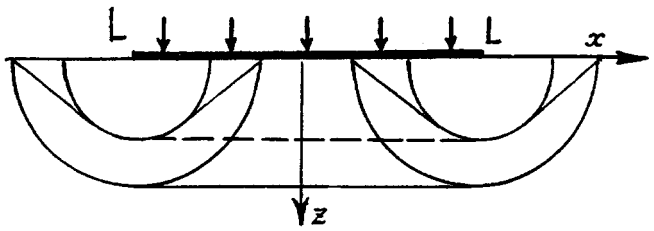

FIG. 1.

the stationary point one has $p(x+\eta)\approx p(x)+\eta p'(x)$, and the contribution of the stationary point is due to the term quadratic in η, which is equal to

$$\frac{\exp(i\varkappa z)}{z\sqrt{z}}g'(0)p'(x)\eta^2\exp\left(i\varkappa\frac{\eta^2}{2z}\right). \tag{10}$$

It follows from the explicit expression for the directional pattern[4] that

$$g'(0)=\frac{\exp\left(-\frac{i\pi}{4}\right)}{\sqrt{2\pi}\mu}\frac{2k}{\varkappa\sqrt{\varkappa}}, \tag{11}$$

where μ is the shear modulus. Using a modification of the method of stationary phase for the case of an amplitude function having a zero of multiplicity two at the stationary point,[5] we obtain, after some manipulations, the following expression for the corresponding wave field:

$$\mathbf{u}^{S,\text{plane}}\approx\frac{2k}{\mu\varkappa^3}p'(x)\exp(i\varkappa z)\mathbf{e}_x, \tag{12}$$

where $\mathbf{e}_x$ is a unit vector along the x axis. Expression (12), which was obtained for points lying beneath the source, has the phase of a plane shear wave traveling downward.

We note that the frequency dependence of the field (12) contains an additional factor of $(i\omega)^{-1}$ in comparison with that for a longitudinal quasi-plane wave. Therefore, in the nonsteady-state case its time dependence is the integral of the time dependence in the longitudinal wave.

6. Thus the onset of a quasi-plane shear wave is due to the spatial nonuniformity of the vertical stress produced by the source at the boundary. Analysis of nonconstant p is important in connection with the fact that for suppression of edge waves, which constitute noise in flaw detection, it is advisable to use apodization, i.e., to produce stresses that vanish at the edges of the source. In that case a shear wave with a plane wave front, like that discussed above, necessarily arises.

This work was begun during a visit of the first author at the South Bank University, London, with the support of the Korolev Society, and was continued with the support of INTAS–RFBR Grant 95-0012.

The authors are grateful to B. Bridge for a stimulating discussion.

[1] J. P. Weight J. Acoust. Soc. Am. **81**, 815 (1987).
[2] X. M. Tang, M. N. Toksöz, and C. H. Cheng J. Acoust. Soc. Am. **87**, 1894 (1990).
[3] H. Djelouah and J. C. Baboux J. Acoust. Soc. Am. **92**, 2932 (1992).
[4] M. E. Ewing, W. S. Jardetsky, and F. Press, *Elastic Waves in Layered Media*, McGraw-Hill, New York (1957).
[5] M. V. Fedoryuk, *Saddle-Point Method* [in Russian], Nauka, Moscow (1977).

Translated by Steve Torstveit

Determination of the parameters of atmospheric gas clouds by radar methods at frequencies in the rotational spectrum

V. A. Ivanchenko and V. V. Nikolaev

Scientific-Research Institute of Mechanics and Physics at the N. G. Chernyshevskiĭ State University, Saratov
(Submitted July 16, 1997)
Pis'ma Zh. Tekh. Fiz. **23**, 1–5 (December 26, 1997)

An analysis is made of a method of determining the parameters and coordinates of atmospheric gas clouds radar systems which can measure the attenuation of electromagnetic radiation power at a resonant absorption frequency. A possible technical application of these systems is indicated. This approach to the problem of controlling and monitoring the state of the atmosphere can describe the propagation dynamics of contamination in real time, which is extremely important for ensuring safety in regions liable to chemical contamination. After suitable development, the proposed method may provide the basis for remote monitoring by radar techniques and in principle, may also be used to study various types of nonreflecting objects possessing the property of resonant absorption. © *1997 American Institute of Physics.* [S1063-7850(97)01712-6]

In many industrialized countries there is currently a need to search for new methods and facilities for ecological monitoring of the state of the near-Earth atmosphere. This is a particularly pressing problem in areas of oil and gas extraction, chemical factories, areas where dangerous and poisonous substances are stored and reprocessed, and also in regions liable to radioactive contamination.[1]

The state of the atmosphere is normally monitored using sensors requiring physical contact whose principal disadvantages include a short dynamic range, limited response time, and the need to develop expensive large-scale computer and communication networks when this equipment is used to monitor large areas.

In many respects, remote and especially radar methods of ecological monitoring are free from these shortcomings.[2,3] Here we consider a possible method of determining the parameters and coordinates of atmospheric gas clouds using an active radar method. This method can provide a real-time description of the propagation dynamics of contamination, which is required to predict the ecological consequences of uncontrolled releases of harmful substances.

In conventional radar methods, electromagnetic radiation reflected from the object being studied is used as the source of information. In principle, gas clouds may not reflect radiation. However, it is possible to construct radar systems which utilize the property of resonant absorption of millimeter radiation at frequencies in the rotational spectrum of the gas. These systems require reference reflectors (reference points) positioned at the boundaries of the area being monitored. Thus, the probe radiation reaches the receiving antenna of the radar station after passing twice through the gas cloud (see Fig. 1).

To solve this problem it is assumed that the gas cloud possesses symmetry relative to the axis perpendicular to the Earth's surface and its concentration distribution obeys the law

$$n(r)=\begin{cases} n_0\theta(r), & r\leqslant R, \\ 0 & r>R, \end{cases} \tag{1}$$

where θ is the distribution function, r is the distance from the axis of symmetry, R is the radius of the cross section of the gas cloud in the plane parallel to the Earth's surface (which characterizes the size of the gas cloud), and n_0 is the gas concentration at the center $(r=0)$. The absorption spectrum of the gas is also known.

Using the basic radar formula[4] and assuming that the directional radiation flux is attenuated as a result of absorption both in the atmosphere and in the gas cloud, we can write

$$\mu(f,\varphi)=\chi_a(D-d)+\int_0^d \chi(f,x)dx, \tag{2}$$

where μ is a function having the form

$$\mu(f,\varphi)=\ln\left(\frac{\sqrt{G_0S_0SP_0}}{4\pi D^2\sqrt{P}}\right),$$

f is the radiation frequency, χ_a and χ are the absorption coefficients of the atmosphere and the contaminant gas, respectively, P_0 is the radiation power of the station, P is the reflected signal power on entry to the receiving antenna, S is the effective scattering area of the reference point, S_0 and G_0 are the effective area and the coefficient of directionality of the transmitting antenna. The angle φ as well as the distances d and D are as shown in Fig. 1.

Since the absorption coefficient is proportional to the gas concentration[4]

$$\chi(f,r)=\sigma(f\ )n(r), \tag{3}$$

formula (2) with allowance for formulas (1) and (3) may be reduced to the form

$$\mu(f,\varphi)=\chi_a(D-d(\varphi,\varphi_0,R,R_0))+n_0\sigma(f\ )F(\varphi,\varphi_0,R,R_0), \tag{4}$$

where R_0, φ_0 are the coordinates of the center of the gas cloud,

$$d(\varphi,\varphi_0,R,R_0)=2R\ \sin(\psi), \tag{5}$$

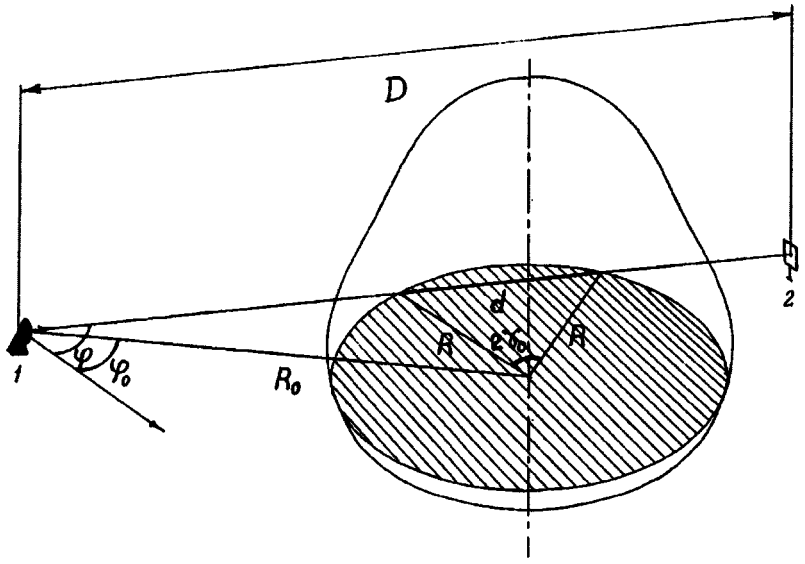

FIG. 1. Principle for determination of the parameters of atmospheric gas clouds: *1*—radar station and *2*—reference point.

$$\psi = \arccos\left(\frac{R_0}{R}\sin(\varphi-\varphi_0)\right), \tag{6}$$

$$F(\varphi,\varphi_0,R,R_0) = 2[R_0\sin(\varphi-\varphi_0)]\int_0^{\psi}\theta\left(R\frac{\cos(\psi)}{\cos(\gamma)}\right)\frac{d\gamma}{\cos^2(\gamma)}. \tag{7}$$

Thus, the unknowns φ_0, R_0, n_0, and R are found from a system of four equations written for four independent determinations of the angle φ:

$$\{\mu(f,\varphi_i) = \chi_a(D-d(\varphi_i,\varphi_0,R,R_0)) + n_0\sigma(f)F(\varphi_i,\varphi_0,R,R_0)\}_{i=\overline{1,4}}.$$

If the radiation frequency of the radar station transmitter can be tuned, the number of determinations of the angle φ can be halved. In this case, the parameters and coordinates of the gas cloud are determined from:

$$\{\mu(f_i,\varphi_j) = \chi_a(D-d(\varphi_j,\varphi_0,R,R_0)) + n_0\sigma(f_i)F(\varphi_j,\varphi_0,R,R_0)\}_{i,j=1,2}.$$

If no data are available on the distribution of the gas concentration, the values of R, R_0, and φ_0 can be determined using three values for φ and the known dependence

$$\frac{\partial\mu(f,\varphi)}{\partial f} = n_0\frac{\partial\sigma(f)}{\partial f}F(\varphi,\varphi_0,R,R_0)$$

using the system of three equations

$$\left\{\mu(f,\varphi_i) = \chi_a(D-d(\varphi_i,\varphi_0,R,R_0)) + \sigma(f)\frac{\partial\mu(f,\varphi_i)}{\partial f}\left[\frac{\partial\sigma(f)}{\partial f}\right]^{-1}\right\}_{i=\overline{1,3}},$$

and then estimating the average gas concentration $\overline{n}$

$$\overline{n} = \frac{1}{3}\sum_{i=1}^{3}\left\{\frac{\partial\mu(f,\varphi_i)}{\partial f}\left[\frac{\partial\sigma(f)}{\partial f}d(\varphi_i,\varphi_0,R,R_0)\right]^{-1}\right\}.$$

Formulas (4)–(7) can then be used to reconstruct the distribution function θ.

In most cases, tuning the transmitter frequency of the radar station in the short-wavelength part of the millimeter range presents appreciable difficulties. Thus, the problem may be solved by using the broadening Δf of the energy spectrum of short radio pulses (at half power), which for rectangular pulses has the form

$$W(f) = \frac{A^2}{4\pi^2\tau}\left[\frac{\sin(\pi\tau(f-f_0))}{f-f_0} - \frac{\sin(\pi\tau(f+f_0))}{f+f_0}\right]^2,$$

where A and f_0 are the amplitude and filling frequency, and τ is the pulse length. For instance, for hydrogen sulfide we find $f_0 = 168.7$ GHz, $\Delta f \approx 884$ MHz ($\tau = 1$ ns), and $\Delta f \approx 177$ MHz ($\tau = 5$ ns).

To conclude, these results demonstrate that it may be possible to construct radar systems to determine the coordinates, size, and concentration of atmospheric gas clouds which exhibit resonant absorption.

[1] S. P. Kalenichenko, Bezopasnost' Zhizned. No. 13, 51 (1994).
[2] E. Shanda, *Physical Principles of Remote Probing* [Russ. transl., Nedra, Moscow, 1990].
[3] V. V. Bogorodskiĭ and A. I. Kozlov, *Microwave Radiometry of the Earth's Atmosphere* [in Russian], Gidrometeoizdat, Moscow (1985).
[4] M. A. El'yashevich, *Atomic and Molecular Spectroscopy* [in Russian], Fizmatgiz, Moscow (1962).
[5] *Radio Engineering Systems*, edited by Yu. M. Kazarinov [in Russian], Vysshaya Shkola, Moscow (1990).

Translated by R. M. Durham

Influence of variations in the angular rotational velocity of a spacecraft on thermal convection under conditions of weightlessness

Yu. A. Polovko and V. S. Yuferev

A. G. Ioffe Physicotechnical Institute, Russian Academy of Sciences, St. Petersburg
(Submitted July 11, 1997)
Pis'ma Zh. Tekh. Fiz. **23**, 6–13 (December 26, 1997)

Unlike the conventional approach where it is assumed that liquid motion under conditions of weightlessness is caused by vibrations or residual quasisteady-state microaccelerations, the present paper examines convection caused by variations in the angular rotational velocity of a spacecraft. It is shown that although the level of microaccelerations caused by variations in the angular rotational velocity is extremely low for the Shuttle spacecraft, Mir space station, and unmanned spacecraft, of the order of 0.1–1 μg, the ensuing convection and nonuniformity in the impurity distribution during crystal growth may be very appreciable. © *1997 American Institute of Physics.* [S1063-7850(97)01812-0]

According to current thinking, the driving force for convection under conditions of weightlessness in the absence of any free liquid surface is a buoyancy force generated by the microacceleration vector. This vector characterizes the resultant effect of various forces and at an arbitrary point P in the spacecraft connected rigidly to its structure, may be calculated using the formula[1]

$$\mathbf{g}=\mathbf{R}\times\dot{\Omega}+(\Omega\times\mathbf{R})\times\Omega+\Omega_*^2(3(\mathbf{e}_r\cdot\mathbf{R})\mathbf{e}_r-\mathbf{R})-\mathbf{g}_v\,. \quad (1)$$

Here $\mathbf{R}$ is the position vector of point P relative to the spacecraft center of mass, Ω is the vector of the absolute angular velocity of the spacecraft, where the dot indicates differentiation with respect to time t, Ω_* is the orbital frequency, $\mathbf{e}_r$ is the unit vector in the ''center of Earth-spacecraft center of mass'' direction, and $\mathbf{g}_v$ is the vector of the microacceleration caused by nongravitational forces (vibrations, atmospheric resistance, and so on). The first two terms in formula (1) are associated with the motion of the spacecraft relative to its center of mass and the third is associated with the nonuniformity of the Earth's gravitational field. In this formulation of the problem the action of the microgravitational field obviously vanishes if there is no density gradient in the liquid. However, the action of microgravitation is in fact more complex. The rotation of the spacecraft produces two forces: a centrifugal force $\rho(\Omega\times\mathbf{R})\times\Omega$ and an inertial force $\rho(\dot{\Omega}\times\mathbf{R})$ caused by variations in the angular velocity of the spacecraft (ρ is the liquid density). The centrifugal force is a potential force and thus, when there are no density gradients in the liquid, this force will only contribute to the pressure, without inducing liquid motion whereas when density gradients do exist, this force will bring the liquid into motion by means of a buoyancy force. However, the inertial force $\rho(\dot{\Omega}\times\mathbf{R})$ is not a potential force and thus cannot be completely incorporated in the pressure. This force will induce liquid motion even in the absence of a buoyancy force. Thus, for an arbitrary rotation of the spacecraft the force acting on a nonuniformly heated liquid under conditions of orbital flight (neglecting the nonuniformity of the Earth's gravitational field) may be written as

$$\mathbf{F}=\mathbf{F}_b+\mathbf{F}_i+\mathbf{F}_c\,, \quad (2)$$

where $\mathbf{F}_b=\rho_0(\mathbf{g}_v+\Omega\times(\Omega\times\mathbf{R})+\dot{\Omega}\times\mathbf{R}_0)\beta_T(T-T_0)$ is the buoyancy or Archimedes force, $\mathbf{F}_i=-\rho_0(\dot{\Omega}\times\mathbf{r})$ is the inertial force caused by the nonuniform rotation of the container, and $\mathbf{F}_c=-2\rho_0(\Omega\times\mathbf{u})$ is the Coriolis force. In these expressions, β_T is the volume coefficient of thermal expansion of the liquid, T is the liquid temperature, T_0 is the temperature at some fixed point inside the container, $\mathbf{R}_0$ is the position vector of this point relative to the center of mass of the spacecraft, $\mathbf{r}=\mathbf{R}-\mathbf{R}_0$ is the position vector connecting this point with an arbitrary point inside the container, and $\mathbf{u}$ is the velocity vector of the liquid motion. It can be seen that only the buoyancy force $\mathbf{F}_b$ has an integer dependence on the vector $\mathbf{g}$ whereas the forces $\mathbf{F}_i$ and $\mathbf{F}_c$ are determined by the angular acceleration and the angular velocity of the spacecraft. It should also be stressed that the action of the force $\mathbf{F}_i$ cannot be reduced to the action of some equivalent buoyancy force. From this it follows that not only the microacceleration vector $\mathbf{g}$ but also the vector of the angular rotational velocity of the spacecraft Ω must be used for the characteristic of the microgravitational field of an orbiting space station.

So far, experts on the physics of liquids and the modeling of crystal growth under conditions of weightlessness have mainly focused their attention on the study of convection under the action of vibrations (g-jitter) and residual microaccelerations, while the action of the force $\mathbf{F}_i$ has been neglected. Here we propose to examine the convection of a liquid under the influence of the nonuniform rotation of the spacecraft. It will be shown subsequently that this convection may be very appreciable although the variations in the angular velocity of the spacecraft are fairly small.

The magnitude of the angular velocity and its variations depend very much on the flight conditions and the orientation of the spacecraft. When an orbiting station has a constant orientation in a geocentric coordinate system, the angular rotational velocity of the station is generally zero. In practice, however, the orientation of a space station is only maintained to within a few tens of minutes of arc and for this reason the angular velocity exhibits deviations from zero with an amplitude of the order of 10^{-5}–10^{-4} s^{-1}. Under

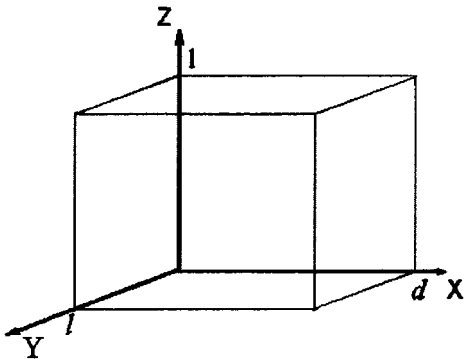

FIG. 1. Schematic of region studied.

different flight conditions, the average angular velocity is nonzero and its modulus is of the order of magnitude of the orbital frequency, i.e., the angular rotational velocity of the station about the Earth.

In order to demonstrate the significance of this correction, we consider the motion of an incompressible liquid in a rectangular three-dimensional cavity with rigid walls, shown in Fig. 1. The following quantities, the height h, Ω_0^{-1}, $\Omega_0 h$, $\rho\Omega_0^2 h^2$, Ω_0, $\Omega_0^2 h$, and ΔT are taken as the scales of length, time, velocity, pressure, angular rotational velocity, microacceleration, and temperature, respectively. In the Boussinesq approximation, the equations of motion of the liquid may be written in the following dimensionless form:

$$\frac{\partial \mathbf{u}}{\partial t}+\mathbf{u}\cdot\nabla\mathbf{u}=\mathrm{Ek}\nabla^2\mathbf{u}-\nabla p-2\Omega\times\mathbf{u}-\frac{\partial\Omega}{\partial t}\times\mathbf{r}$$
$$+\mathrm{GrEk}^2\left(\frac{d\Omega}{dt}\times\mathbf{R}_0+\Omega\times(\Omega\times(\mathbf{R}_0+\mathbf{r}))T,\right.$$
$$\nabla\cdot\mathbf{u}=0,$$
$$\frac{\partial T}{\partial t}+\mathbf{u}\cdot\nabla T=\frac{\mathrm{Ek}}{\mathrm{Pr}}\nabla^2 T, \qquad (3)$$

where $\mathrm{Ek}=\nu/\Omega_0 h^2$, $\mathrm{Gr}=\beta\Delta T\Omega_0^2 h^4/\nu^2$, and $\mathrm{Pr}=\nu/a$ are the Ekman, Grasshof, and Prandtl numbers, respectively, and ν and a are the kinematic viscosity and the thermal diffusivity of the liquid.

The boundary conditions for the system (3) were defined as

$$\mathbf{u}=0 \quad \text{for } z=0,1, \quad x=0,d \quad \text{and } y=0,l,$$
$$T=0 \quad \text{for } z=0 \quad \text{and} \quad T=1 \quad \text{for } z=1,$$
$$\frac{\partial T}{\partial x}=0 \quad \text{for } x=0;d \quad \text{and} \quad \frac{\partial T}{\partial y}=0 \quad \text{for } y=0;l. \qquad (4)$$

As initial conditions, it was assumed that no convective motion occurred before time $t=0$. Numerical integration of the problem (3)–(4) was performed using a method proposed in Ref. 2, which was generalized to the three-dimensional case.

We analyzed the convection which occurs under the influence of real variations in the angular velocity of a spacecraft. Examples of such variations are shown in Fig. 2 for the manned Mir-Shuttle complex (Fig. 2a) and for an unmanned spacecraft (Fig. 2b). The dependences of the dimensionless components of the angular velocity were calculated by V. V. Sazonov who kindly supplied us with this data. Here and subsequently the scale of Ω_0 was taken as $0.001\ \mathrm{s}^{-1}$. The method of determining these velocities was described in detail in Refs. 1 and 3. The flight of the Mir-Shuttle complex took place in the gravitational orientation regime. In this case, the modulus of the angular velocity of the complex is similar to the angular velocity of its rotation about the Earth ($\approx 0.001\ \mathrm{s}^{-1}$), and the amplitude of the angular velocity variations and the angular accelerations are fairly small: of the order of $10^{-4}\ \mathrm{s}^{-1}$ and $10^{-7}\ \mathrm{s}^{-2}$, respectively. These values of the angular acceleration and the amplitude of the angular velocity variations are typical of heavy spacecraft flying in this regime. However, satellites of lower mass, flying in lower orbits, may rotate considerably faster and with larger variations in the angular velocity (Fig. 2b).

It follows from formula (2) that the ratio between the buoyancy force $\mathbf{F}_b$ and the inertial force $\mathbf{F}_i$ is given by $|\mathbf{F}_i|/|\mathbf{F}_b|\approx|\mathbf{r}|/\beta\Delta T|\mathbf{R}_0|$, where $|\mathbf{R}_0|$ is the distance between the liquid container and the center of gravity of the spaceship. The latter was taken to be constant in the calculations $R_{0x}=R_{0y}=R_{0z}=60$, whereas $\beta\Delta T$ varied. The maximum of the modulus of the convective velocity $u_{\max}$ was taken as a measure of the convection rate. It was also assumed that $\mathbf{g}_v=0$, i.e., residual microaccelerations and vibrations (g-jitter) were neglected. The results of calculations of the maximum convection velocity which could occur in a cubic cavity under the influence of variations in the angular velocity of the Mir-Shuttle complex are plotted in Fig. 3. The case

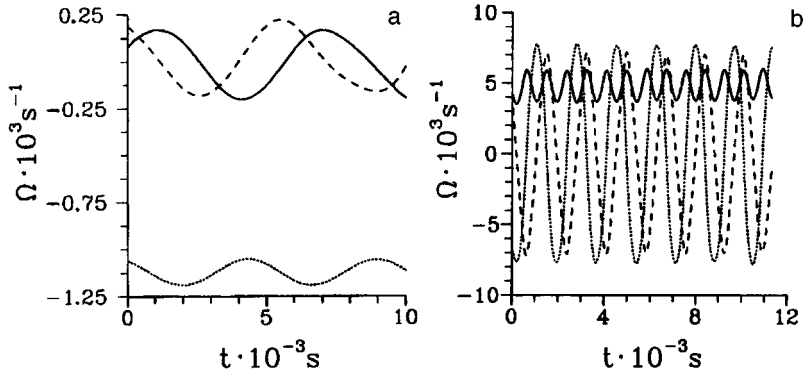

FIG. 2. Angular velocity of spacecraft versus time: a—Mir-Shuttle complex, b—unmanned spacecraft. Solid curves—Ω_x, dashed curves—Ω_y, and dots—Ω_z.

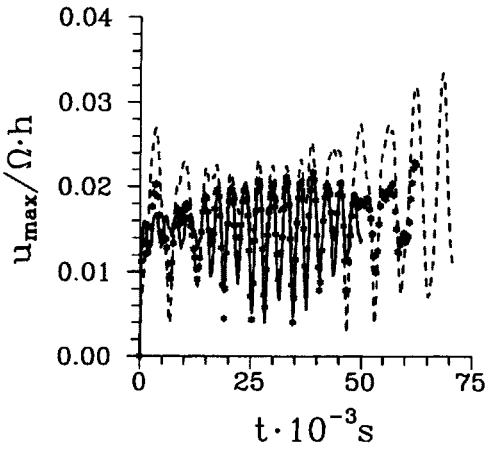

FIG. 3. Variation of the maximum convection velocity of a liquid in a cubic container as a function of time under the influence of angular velocity variations of the Mir-Shuttle complex. Ek=0.1, Pr=0.01, $\beta\Delta T=0$—continuous curve, 0.001—asterisks, 0.003—dashed curve.

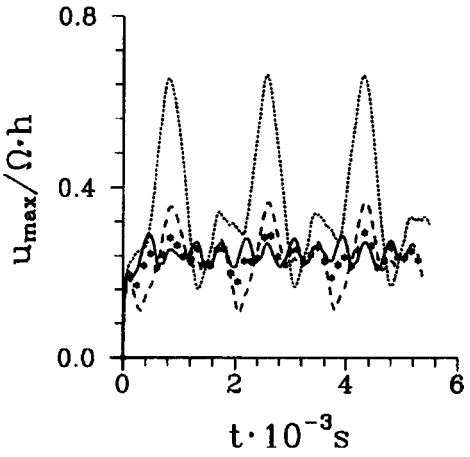

FIG. 4. Variation of the maximum convection velocity of a liquid in a rectangular container with sides $l=d=0.5$ as a function of time under the influence of angular velocity variations shown in Fig. 2b. Ek=0.158, Pr=0.01, $\beta\Delta T=0$—continuous curve, 0.001—asterisks, 0.003—dashed curve.

$\beta\Delta T$ corresponds to isothermal convection which is neglected in the standard approach to the problem of convection in weightlessness. It can be seen that in this case, the dimensional convection velocity is $0.01-0.02\Omega_0 h$ or $0.1-0.2v/h$. The last expression is obtained if the Ekman number is taken as 0.1 for the calculations. It can be seen that although the convection velocity is fairly low, it may nevertheless have a fairly appreciable influence on impurity transport processes during crystal growth, particularly at low growth rates (of the order of one micron) and low impurity diffusion coefficients. As $\beta\Delta T$ increases, the amplitude of the variations in the maximum convection velocity increases substantially, which is clearly caused by interaction between the buoyancy force $\mathbf{F}_b$ and the inertial force $\mathbf{F}_i$. However, the influence of thermal convection only becomes appreciable for fairly large temperature drops where $\beta\Delta T|\mathbf{R}_0| \gg 0.1$. Figure 4 shows results of calculations of the maximum convection velocity under the influence of the angular velocity variations shown in Fig. 2b in a rectangular region with side lengths $l=d=0.5$. In this case, the convection rate is considerably higher, which is not surprising since the amplitude of the angular velocity variations of the spacecraft is more than an order of magnitude greater than those of the Mir-Shuttle complex. It should be noted that in both these examples, the microaccelerations are small, of the order of $0.2-2\times10^{-6}g_0$, where g_0 is the acceleration due to gravity at the Earth's surface.

To sum up, the convection caused by variations in the angular rotational velocity of a spacecraft may be very appreciable and must be taken into account when designing and analyzing the results of technological experiments and fluid physics experiments on board spacecraft.

This work was carried out under contract between the Russian Space Agency and NASA NAS-15-10110.

[1] V. V. Sazonov and S. G. Zykov, *Calculations and Measurements of the Low-Frequency Component of the Microacceleration on Board an Artificial Earth Satellite*, Preprint No. 31, M. V. Keldysh Institute of Applied Mathematics, Russian Academy of Sciences, Moscow (1996).
[2] W. Y. Soh and J. W. Goodrich, J. Comput. Phys. **79**, 113 (1988).
[3] V. V. Sazonov, M. M. Komarov, M. Yu. Belyaev, S. G. Zykov, and V. M. Stazhkov, *Estimate of the Quasistatic Component of the Microacceleration on Board an Artificial Earth Satellite*, Preprint No. 45, M. V. Keldysh Institute of Applied Mathematics, Russian Academy of Sciences, Moscow (1995).

Translated by R. M. Durham

Čerenkov superradiance from a subnanosecond electron bunch in a sectional decelerating system

M. I. Yalandin, S. A. Shunaĭlov, V. G. Shpak, N. S. Ginzburg, I. V. Zotova, A. S. Sergeev, A. D. R. Phelps, A. W. Cross, and P. Aitken

Institute of Experimental Physics, Urals Branch of the Russian Academy of Sciences, Ekaterinburg; Institute of Applied Physics, Russian Academy of Sciences, Nizhniĭ Novgorod; Strathclyde University, Glasgow, Great Britain

(Submitted July 30, 1997)
Pis'ma Zh. Tekh. Fiz. **23**, 14–19 (December 26, 1997)

Induced coherent radiation (superradiance) from a subnanosecond electron bunch in a combined decelerating system has been investigated experimentally. In a first section formed by a periodically modulated waveguide, the density of the bunch is modulated and it then radiates in a second section formed by a waveguide partially filled with a dielectric. At an electron energy of 250 keV and a peak current of 800 A, millimeter radiation pulses with powers up to 2 MW and lengths up to 800 ps were obtained.
[S1063-7850(97)01912-5]

Studies of coherent radiation processes in isolated electron bunches having dimensions greater than the wavelength of microwave radiation but still substantially shorter than the characteristic lengths of the interaction space have recently attracted considerable interest. The possibility of obtaining coherent radiation from these bunches was appreciated relatively recently and is associated with so-called superradiance effects.[1–5] The evolution of this type of process inside an electron bunch is accompanied by particle bunching whose phasing is caused by slippage of radiation relative to the bunch as a result of a difference between the group velocity of the radiation and the translational velocity of the particles.

The results of the first experimental observations of Čerenkov supperradiance in the millimeter wavelength range were discussed in Refs. 6 and 7. The source of subnanosecond electron pulses was a high-current accelerator consisting of a RADAN 303 generator, a pulse slicer, and a coaxial magnetically insulated vacuum diode with an explosive emission cathode.[8] Superradiance was observed in two types of decelerating systems. The first system was a corrugated waveguide in which the electron bunch interacted with the concurrent spatial harmonic of a counterpropagating electromagnetic wave under synchronism conditions similar to those found in backward-wave tubes:

$$\omega=(-k+\overline{k})V_{\parallel},$$

where $V_{\parallel}$ is the translational electron velocity, ω and k are the frequency and longitudinal wave number, respectively, $\overline{k}=2\pi/d$, and d is the corrugation period. An alternative decelerating system comprised a regular waveguide partially filled with a dielectric. Here, the wave was emitted in the direction of translational motion of the particles and interaction took place under the conditions

$$\omega=kV_{\parallel}.$$

Features of the first system (a corrugated waveguide 8 cm long) included a high level of stability and reproducibility of the microwave pulses at a moderate peak power of 0.5 MW. The angular distribution of the radiation broadly corresponded to the excitation of the E_{01} mode. The superradiance in the dielectric waveguide, whose typical length was 30 cm, had a peak radiation power of 1 MW. However, the radiation exhibited considerably lower stability and comprised a combination of E_{01} modes and the HE_{11} hybrid mode.

Here we report an experimental investigation of superradiance from an electron bunch in a combined (sectional) decelerating system where the first section, formed by a corrugated waveguide, serves to modulate the electron bunch and the second section, consisting of a waveguide partially filled with a dielectric, functions as the emission (amplification) region. An advantage of a sectional system is that the high degree of stability and reproducibility of the superradiance pulses typical of backward-wave tube systems can be combined with the high peak power achieved previously as a result of emission from an electron bunch in a dielectric waveguide. As in previous experiments, the subnanosecond accelerator generated a beam with a current pulse length of 300–500 ps and a typical electron energy of 250 keV. The microwave pulses were recorded with a calibrated hot carrier germanium detector with a transient characteristic of 200 ps. The signals from the current, accelerating voltage, and microwave signal detectors were recorded using a 7 GHz Tektronix 7250 digitizing oscilloscope. The microwave unit of the experimental apparatus is shown schematically in Fig. 1. The length of the corrugated section of circular waveguide

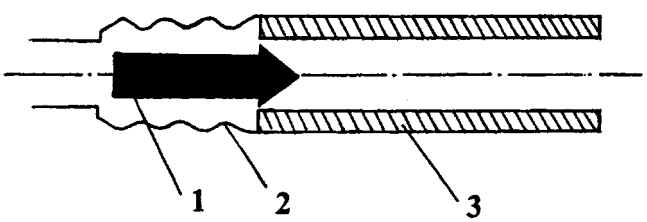

FIG. 1. Schematic of microwave section of experimental apparatus: *1*—electron bunch, *2*—modulator formed by section of corrugated waveguide, and *3*—emission region formed by a waveguide partially filled with a dielectric.

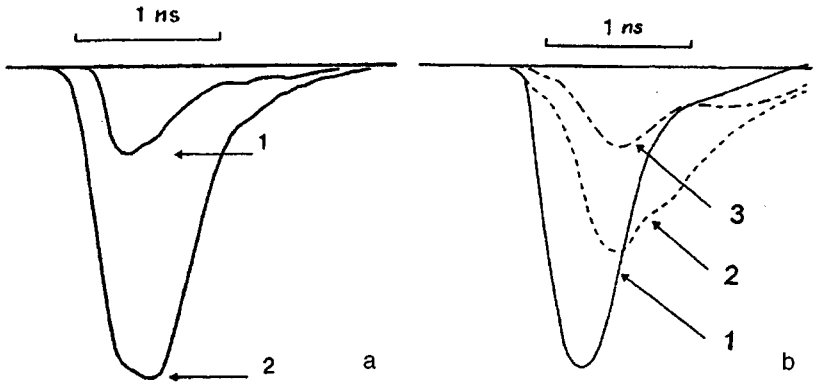

FIG. 2. a—Signal from microwave detectors obtained without (curve *1*) and with modulator (curve *2*); b—transformation of the signal with high-frequency filters installed in the waveguide channel.

was 3 cm, the corrugation period was 3.3 mm with a corrugation depth of 0.8 mm, and the average waveguide diameter was 8 mm. The length of the second section was 20 cm. A composite dielectric waveguide with a dielectric constant of ~ 3.5 was used as this decelerating system.

The operating efficiency of the sectional system is evidenced by Fig. 2a which shows that the installation of a modulator increased the peak power of the microwave pulse approximately five times compared with the radiation only in the dielectric channel. We also note that without the second section, i.e., when the electron bunch only passed through a short modulator, the output signal was at the noise level and was barely recorded by the detector. The spectral composition of the radiation was estimated by installing high-frequency waveguide filters (cutoff waveguides) with different cutoff frequencies in the detector channel.

Figure 2b shows the evolution of the microwave pulse profile as the signal passes through various filters. It can be concluded from these results that the pulse spectrum lies approximately between 36 and 40 GHz. The angular distribution of the radiation, shown in Fig. 3a, was recorded by a detector whose receiving horn was oriented to detect the E_r component of the field.

In an ideal variant the entry section should not only modulate the electron bunch longitudinally but should also define the transverse structure of this modulation, thus assigning to the radiation in the second section a spatial structure in the form of the E_{01} mode. It is known that when this mode is excited, the angular distribution of the radiation should have a zero (deep minimum) on the axis of the system. The absence of such a minimum indicates that the radiation spectrum contains the hybrid HE_{11} mode. This may be attributed to the azimuthal inhomogeneity of the electron bunch in the second section. This inhomogeneity is caused by the initial inhomogeneity of the emitting surface of the tubular cathode and also by some misalignment of the system. At least the replica of the bunch in various cross sections of the electrodynamic channel indicated that it possessed transverse asymmetry.

The percent content of the parasitic HE_{11} mode differs at the beginning and at the tail of the microwave pulse. This can be seen from a comparison of oscilloscope traces recorded by a detector positioned near the axis of the system (position *1*, Fig. 3b) and at the edge (position *2*, Fig. 3c). A relative increase in the signal amplitude in the tail section of the pulse is observed for the horn in position *2* with a corresponding decay for the horn in position *1*. Thus, the angular distribution for the tail section of the pulse is more consistent with the excitation of the E_{01} working mode. To interpret this observation, it should be borne in mind that for the leading section of the electron pulse the first section only operates as an electron beam modulator. However, the microwave radiation generated in this section in the form of a counterpropagating electromagnetic wave relative to the bunch E_{01} is re-

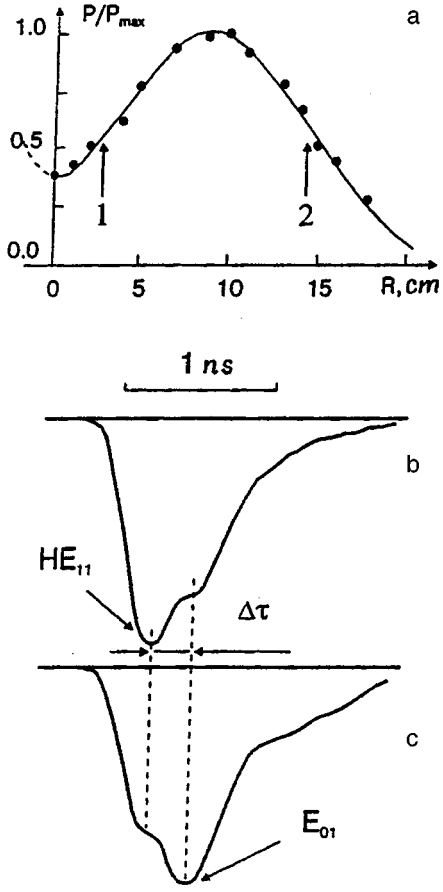

FIG. 3. Angular distribution of radiation (a), showing two positions of the microwave detector along the radial coordinate at which the signals shown in Figs. 3b and 3c were observed.

flected from a supercritical constriction positioned at the gun end of the system and passes through the modulator concurrently with the electrons, before entering the second section where it again interacts with the tail section of the electron bunch. Thus, the tail section is exposed to an additional influence from the incoming signal from the first section with a delay $\Delta\tau \approx 300$ ps which ultimately gives the radiation the spatial structure of the E_{01} mode.

To conclude, these experimental investigations have shown that it is justified to use a sectional decelerating system to generate high-power pulses of Čerenkov superradiance. The peak radiation power was increased to 2 MW, the overall length of the electrodynamic system was reduced (from 30 to 23 cm), and the angular distribution and reproducibility of the pulses was enhanced.

This work was supported by the Russian Fund for Fundamental Research, Grant No. 95-02-04791.

[1] R. Bonifacio, C. Maroli, and N. Piovella, Opt. Commun. **68**, 369 (1988).
[2] R. Bonifacio, N. Piovella, and B. W. J. McNeil, Phys. Rev. A **44**, 3441 (1991).
[3] N. S. Ginzburg, I. V. Zotova, and A. S. Sergeev, Pis'ma Zh. Eksp. Teor. Fiz. **60**, 501 (1994) [JETP Lett. **60**, 513 (1994)].
[4] N. S. Ginzburg and Yu. V. Novozhilova, Pis'ma Zh. Tekh. Fiz. **22**(9), 39 (1996) [Tech. Phys. Lett. **22**, 359 (1996)].
[5] N. S. Ginzburg, I. V. Zotova, A. S. Sergeev, I. V. Konoplev, A. D. R. Phelps, A. W. Cross, S. J. Cooke, V. G. Shpak, M. I. Yalandin, S. A. Shunaiov, and M. R. Ul'maskulov, Phys. Rev. Lett. **78**, 2365 (1997).
[6] A. D. R. Phelps, A. W. Cross, S. J. Cooke *et al.*, in *Proceedings of the International Workshop on Strong Microwaves in Plasmas*, Institute of Applied Physics, Russian Academy of Sciences, 1996, Vol. 2, p. 791.
[7] N. S. Ginzburg, I. V. Zotova, and A. S. Sergeev, Abstracts of Papers presented at the 18th International Conference on Free Electron Lasers, Rome, Italy, 1996, p. 50.
[8] V. G. Shpak, S. A. Shunaĭlov, M. R. Ul'maskulov, M. I. Yalandin, and I. V. Pegel', Pis'ma Zh. Tekh. Fiz. **22**(7), 65 (1996) [Tech. Phys. Lett. **22**, 297 (1996)].

Translated by R. M. Durham

Desorption of fullerene C_{60} from a mixture with a copolymer of trifluorochloroethylene and vinylidene fluoride

A. O. Pozdnyakov, B. M. Ginzburg, O. F. Pozdnyakov, and B. P. Redkov

Institute of Problems in Mechanical Engineering, Russian Academy of Sciences, St. Petersburg
(Submitted July 21, 1997)
Pis'ma Zh. Tekh. Fiz. **23**, 20–26 (December 26, 1997)

Thermal desorption mass spectrometry has been used to study the desorption of fullerene C_{60} molecules from a mixture with a copolymer of trifluorochloroethylene and vinylidene fluoride. The temperature range of the C_{60} yield from the copolymer mixture is substantially lower (approximately 100 °C lower) than the temperature range for the sublimation of pure C_{60} molecules. The temperature range of the C_{60} yield from the copolymer mixture is the same as that for the desorption of HCl and HF formed as a result of copolymer cross linking reactions. The desorption of C_{60} from the copolymer mixture is a two-stage process correlated with the stages of HCL and HF formation for which the temperatures at the maximum desorption rates differ. The results suggest that the copolymer cross-linking processes and the desorption of C_{60} molecules are interrelated. © *1997 American Institute of Physics.* [S1063-7850(97)02012-0]

Copolymers of trifluorochloroethylene and vinylidene fluoride are widely used for protective or antifriction coatings, so that the search for modifying additives such as fullerene C_{60} molecules and studies of their interaction with the copolymer macromolecules are of major practical and scientific importance. We have already shown[1] by mass spectrometry that when a copolymer of trifluorochloroethylene and vinylidene fluoride is heated in vacuum, the main volatile products are hydrogen halides (HCl and HF), trifluorochloroethylene, 1-propane, 3-chloro-1,1,2,3,3-pentafluorine and chloropentafluoroethane, and that unlike all the other products, the formation of hydrogen halides is a two-stage process. Combined with data on the reduced solubility of the copolymer[2–4] in the temperature range of the low-temperature hydrogen halide formation stage, the results suggest that at the low-temperature stage the formation of hydrogen halides is a consequence of cross-linking reactions between copolymer chains with the formation of C–C cross links between the chains.

We have also begun to study the relative influence of reactions in the polymer chains and the temperature behavior of fullerene C_{60} taking polystyrene as an example. It was shown in Ref. 5 that, unlike the case where a mixture of polystyrene and C_{60} is heated i.e., the case of van der Waals interaction between polystyrene macromolecules and C_{60} where destruction of the polystyrene merely leads to a negligible decrease in the maximum temperature of C_{60} desorption, when polystyrene is heated with grafted C_{60}, i.e., under conditions of covalent attachment of C_{60} to polystyrene macromolecules, the destruction of the polystyrene is accompanied by complex desorption of C_{60}, for which the profile and intensity of the thermal desorption peaks show good agreement with the thermal destruction reaction of polystyrene. It may be hypothesized that the thermal desorption of C_{60} is a unique microprobe, sensitive to the type of interaction between C_{60} and the polymer. It is also known from the literature[6,7] that C_{60} interacts readily with halogens and hydrogen to form stable compounds. Thus, one of the aims of the present study is to identify the nature of the thermal desorption of C_{60} mixed with a polymer having side hydrogen atoms and side halogens. It is natural to assume that C_{60}, which is highly active in relation to a broad spectrum of chemical agents,[6–11] will exhibit selective interaction with side atoms of macromolecules. This interaction shows up particularly well in the formation of interchain cross links when a copolymer of trifluorochloroethylene and vinylidene fluoride is heated, as was demonstrated in our previous study.[1]

We used an F-32 grade copolymer of trifluorochloroethylene and vinylidene fluoride (average numerical molecular mass $M_n \cong 1.2\times10^5$, trifluorochloroethylene and vinylidene fluoride content 73 and 27 mol.%, respectively) and C_{60} (96–98%) prepared by the Kratschmer method. Films were prepared on the surface of steel foil by depositing 10 μl of an ethylacetate solution of the copolymer followed by a suitable quantity of a toluene solution of C_{60} using a calibrated microsyringe. The mass ratio of C_{60} to copolymer was around 1/3 which approximately corresponds to 100 C_{60} molecules per copolymer molecule. The average calculated thickness of the films after removing the solvents was around 2000 Å.

We used an MCX-6 time-of-flight mass spectrometer (mass reflectron) with a resolving power of around 700, updated with a special vacuum chamber for thermal desorption mass spectrometry. The pressure in the chamber of the mass spectrometer was maintained at 5×10^5 Pa before the experiments.

The composition of the volatile products formed by heating films of the pure copolymer in the range 200–700 °C was determined in Ref. 1. Figure 1a shows two-stage temperature curves of the hydrogen halide yield: two HF release peaks can be identified at 250 and 400 °C while HCl peaks are observed at slightly higher temperatures, ~300 and 420 °C, i.e., the highest intensity of the cross-link formation processes involving fluorine atoms on the one hand and chlorine atoms on the other is obtained at slightly different temperatures. The yield of one of the comonomers of the copoly-

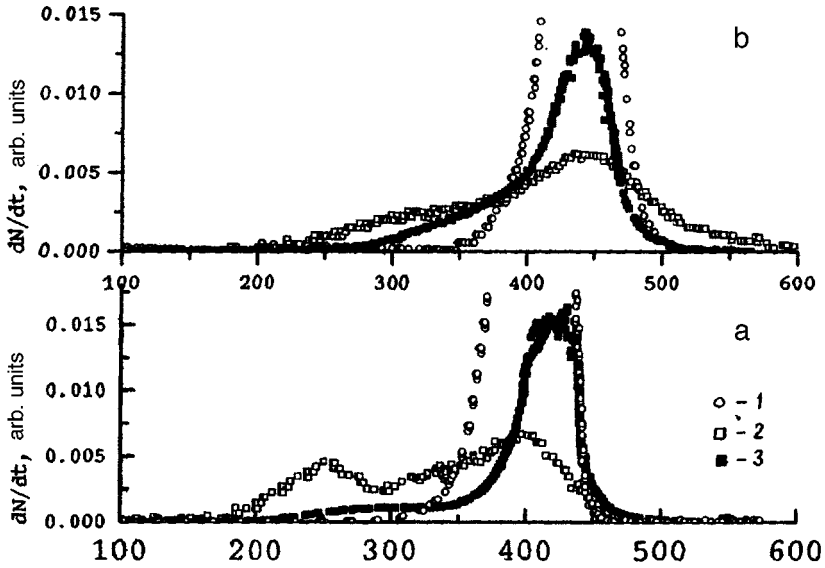

FIG. 1. Temperature dependences of the rate of formation of the comonomer (CF_2CFCl) (*1*), HF (*2*), and HCl (*3*) as a result of heating a copolymer of trifluorochloroethylene and vinylidene fluoride at the rate: a—0.7 K/s and b—7 K/s.

mer, trifluorochloroethylene (CF_2CFCl), involves a single-stage process with a maximum at 400–410°. Figure 1b shows similar curves obtained at a heating rate an order of magnitude higher than that used to obtain the curves plotted in Fig. 1a. In this case, the HF yield is observed at ~330 and 440 °C. On the curve of the HCl yield the low-temperature stage is far less clearly defined than that for the low heating rate (Fig. 1a) and shows up as some asymmetry of the overall peak in the low-temperature range, with the high-temperature peak shifted to 440 °C. The trifluorochloroethylene yield is also shifted to higher temperatures (around 440 °C), i.e., as at the low rate of heating, the high-temperature stages of the yield of all the products lie in the same temperature range, which provides additional evidence that the structuring processes resulting in their formation are interrelated. It may be stressed that a characteristic feature of the behavior of the thermal desorption curves with increasing heating rate is a shift of the thermal desorption peaks toward higher temperatures together with reduced resolution of the individual stages of hydrogen halide release.

An identification of the mass spectra of films prepared from a mixture of C_{60} and copolymer revealed that, in addition to the products observed as a result of heating the pure copolymer, C_{60} molecules are also formed when the copolymer-C_{60} mixture is heated. On account of the small quantities of C_{60} in the thin films being studied, we used high rates of heating (around 10 K/s) to record the thermal desorption curves for the C_{60}-copolymer mixture. Figure 2 shows the thermal desorption curve of C_{60} from a copolymer mixture and for comparison, the temperature dependence of the rate of formation of C_{60} molecules from a polylayer of C_{60} molecules, which illustrates the sublimation of crystalline

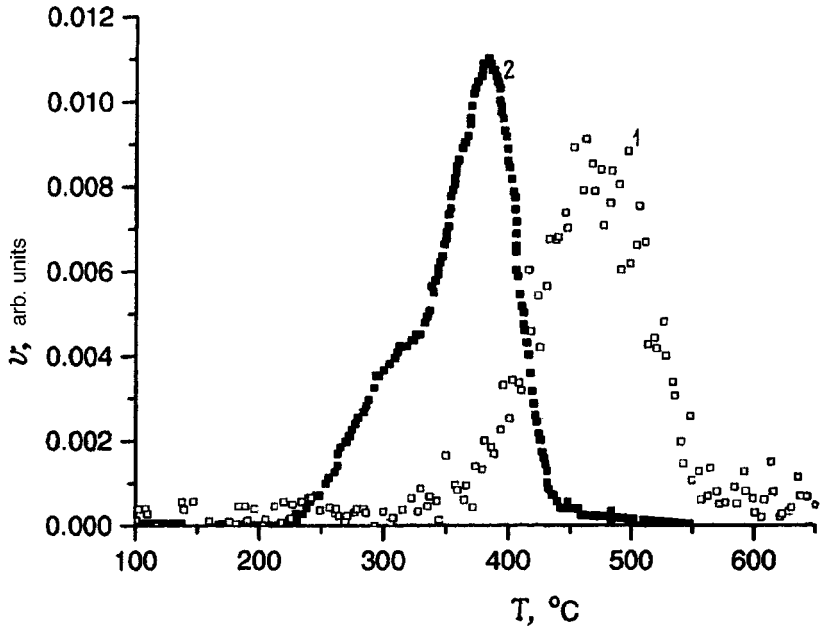

FIG. 2. Rate of formation of $_{60}$ from a $_{60}$ polylayer (*1*) and from a mixture with a copolymer of trifluorochloroethylene and vinylidene fluoride (*2*).

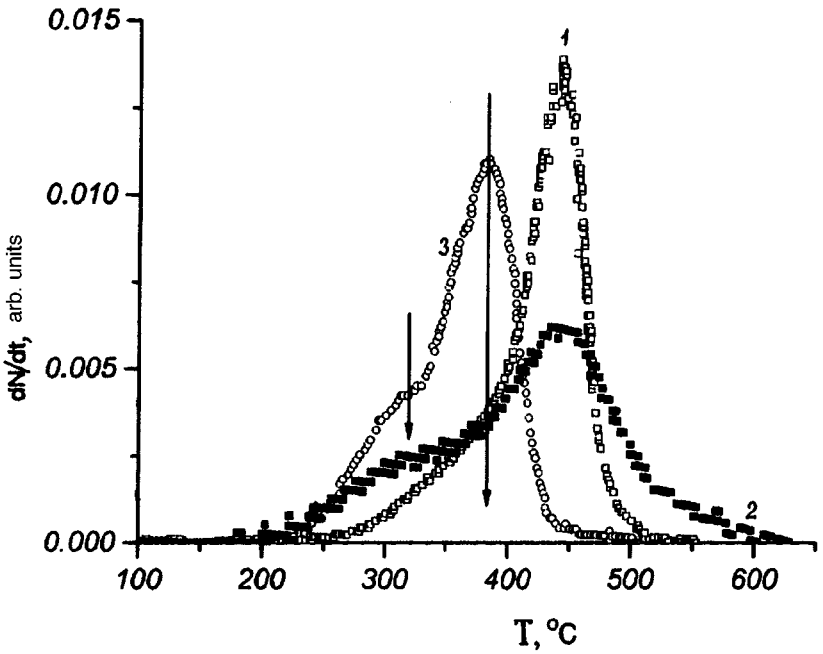

FIG. 3. Rate of formation of HCl (*1*), HF (*2*), and C_{60} (*3*) as a result of heating a mixture of C_{60} with a copolymer of trifluorochloroethylene and vinylidene fluoride.

C_{60}. These results indicate first, that there is a substantial difference between the state of the C_{60} molecules in the copolymer mixture and their state in films of pure crystalline C_{60}, as is evidenced by the shift of the main stage of C_{60} release from the copolymer mixture compared with pure C_{60} toward temperatures approximately 100 °C lower. Second, the curves reveal a two-stage process of C_{60} release from the copolymer, i.e., the envelope of the C_{60} thermal desorption curve exhibits a low-temperature shoulder at $\approx$330 °C and a principal peak at 370 °C.

The abrupt change in the temperature range of the C_{60} yield clearly reflects a change in the structural state of the C_{60} molecules in the polymer film and specifically indicates that the initial crystalline C_{60} ''dissolves'' at the experimental temperatures. A possible interpretation of the two-stage formation of C_{60} from a copolymer mixture is based on comparing the thermal desorption curves of C_{60} and the yield of other volatile products from the C_{60}-copolymer mixture (Fig. 3). It can be seen that the low-temperature shoulder of C_{60} release is observed at temperatures corresponding to the low-temperature stage of the HF yield and the high-temperature stage of C_{60} release corresponds to the low-temperature stage of the HCl yield, which is arbitrarily illustrated by the vertical arrows in the figure.

To conclude, it is quite plausible to assume that C_{60} interacts fairly strongly with side atoms in the copolymer chain, as can be seen from its thermal desorption pattern in the course of the intermolecular cross-linking reactions. The C_{60} molecules, as in the case of polystyrene grafted to C_{60} (Ref. 5), play the role of a unique intermolecular microprobe which traces the temperature behavior of the copolymer chain. Specifically, the removal of hydrogen halides as a result of the formation of intermolecular cross links, is accompanied by the desorption of C_{60}. Taking as an example the yield of hydrogen halides at high heating rates, it has been shown that the thermal desorption of C_{60} may be an indicator of chemical processes in the system in cases where these are difficult to determine experimentally under the same conditions, for example, at low concentrations of the material being studied.

[1] A. O. Pozdnyakov and B. M. Ginzburg, Pis'ma Zh. Tekh. Fiz. **23**(17), 87 (1997) [Tech. Phys. Lett. **23**, 694 (1997)].
[2] T. G. Degteva, Vysokomolek. Soed. **3**, 671 (161).
[3] T. G. Degteva, I. M. Sedova, and A. S. Kuz'minskiĭ, Vysokomolek. Soed. **5**, 378 (1963).
[4] T. G. Degteva, I. M. Sedova, and A. S. Kuz'minskiĭ, Vysokomolek. Soed. **5**, 1485 (1963).
[5] A. O. Pozdnyakov, O. F. Pozdnyakov, B. P. Redkov, V. N. Zgonnik, E. Yu. Melenevskaya, L. V. Vinogradova, and B. M. Ginzburg, Pis'ma Zh. Tekh. Fiz. **22**(18), 57 (1996) [Tech. Phys. Lett. **22**, 759 (1996)].
[6] K. Kniaź, J. E. Fisher, H. Selig, G. B. M. Vaughan, W. J. Romanov, D. M. Cox, S. K. Chowdhury, J. P. McCauley, R. M. Strongin, and A. B. Smith, J. Am. Chem. Soc. **115**, 6060 (1993).
[7] N. F. Gold'shleger and A. P. Moravskiĭ, Usp. Khim. **66**, No. 4 (1997).
[8] V. I. Sokolov, Izv. Akad. Nauk. SSR, Ser. Khi. , No. 1 (1993).
[9] V. I. Sokolov and I. V. Stankevich, Usp. Khim. **62**, No. 5 (1993).
[10] R. Taylor and D. R. M. Walton, Nature (London) **363**, 685 (1993).
[11] C. N. McEwen, R. G. Mckay, and B. S. Larsen, J. Am. Chem. Soc. **114**, 4413 (1992).

Translated by R. M. Durham

Superconductivity in single crystals of the nonperovskite-like cuprate $Ba_2Cu_3O_{6-x}$

S. V. Moshkin, S. I. Goloshchapov, O. V. Frank-Kamenetskaya, I. I. Bannova, T. I. Ivanova, T. N. Kaminskaya, M. A. Kuz'mina, and M. Yu. Vlasov

St. Petersburg State University; A. F. Ioffe Physicotechnical Institute, Russian Academy of Sciences, St. Petersburg

(Submitted July 4, 1997)
Pis'ma Zh. Tekh. Fiz. **23**, 27–34 (December 26, 1997)

Spontaneous crystallization from a solution in a melt at a pressure of $(0.8-1)\times10^{-3}$ Pa was used to obtain single crystals of a new nonperovskite-like superconducting phase $Ba_2Cu_3O_{6-x}$ (space group P_{ccm}, $a=13.065$, $b=20.654$, and $c=11.431$ Å). The superconducting properties of the crystals were investigated by modulated microwave absorption. The superconducting transition temperatures were 5 K (sample No. 1), 7 K and 13 K (sample No. 2). The superconductivity in the $Ba_2Cu_3O_{6-x}$ crystals is attributed to the presence of CuO_2 chains of edge-sharing copper-oxygen squares. Nonperovskite-like $Ba_2Cu_3O_{6-x}$ crystals are a new class of one-dimensional (1D) superconductors. © *1997 American Institute of Physics.* [S1063-7850(97)02112-5]

The observation of superconducting properties in the incommensurate composite phase $Sr_{0.4}Ca_{13.6}Cu_{24}O_{41+x}$ (Ref. 1) has shown that a perovskite-like crystal structure containing CuO_2 planes formed by stacked copper-oxygen squares is not a necessary condition for superconductivity in cuprates of alkaline-earth metals. The structure of $Sr_{0.4}Ca_{13.6}Cu_{24}O_{41+x}$ contains two types of copper-oxygen fragments formed by plane edge-sharing $[CuO_4]$ squares: CuO_2 chains and Cu_2O_3 layers of two-legged ladders. It is not yet clear which of these fragments (one-dimensional or quasione-dimensional) is responsible for the superconducting transition of this phase at $T_c=(12-9)$ K and a pressure of 3–4.5 GPa.

Here we describe a new superconducting nonperovskite-like phase $Ba_2Cu_3O_{6-x}$. Compounds with a similar chemical composition are known in the Ba–Cu–O system and at least five polymorphic modifications have been reported in the literature (see Table I). No data have been reported on the preparation of single crystals of these phases. The crystal structure is determined to a first approximation using powder diffractometry data only for the monoclinic modification.[3] No studies of the superconducting properties of $Ba_2Cu_3O_{6-x}$ modifications have been reported.

Single crystals of the $Ba_2Cu_3O_{6-x}$ phase were prepared in our attempts to synthesize crystals of high-temperature superconducting phases in the Hg–Ba–Ca–Cu–O system. The experiments were carried out by spontaneous crystallization from a solution in a melt. The solvent was excess HgO+CuO. The composition of the charge was varied in the range: Hg:Ba:Ca:Cu=(2.0–3.5):2.0:(0–1.5):(3.0–6.0). The 20 ml crucible (aluminum oxide) containing the charge was sealed in a thick-walled quartz ampoule. The ampoule was inserted in an autoclave pressurized to an excess pressure of $(0.8-1)\times10^{-3}$ Pa, heated to 700 °C, and held at this temperature for 24 h. The ampoule was then heated to 950 °C at a rate of 50°/h and, after being held at this temperature for 1 h, was cooled to 850 °C at a rate of 4–15 °C/h. The furnace was then switched off.

Powder diffractometry data indicate that the ingots obtained under these conditions predominantly contain nonsuperconducting phases: CuO, $BaCuO_2$, Ca_2CuO_3, HgO, $Ca_3Al_2O_6$, an incommensurate composite phase $[Ca_2Cu_2O_3]_xCuO_2]$, and also the oxide $Ba_2Cu_3O_{6-x}$, which has a nonstoichiometric oxygen content and forms the subject of the present study. Fairly large crystals of the recently discovered high-temperature superconducting phase $CaCuO_{2+x}$ are also formed in small amounts.[5] The distribution and shape of the HgO crystals indicates that they are grown from the vapor phase while the other phases crystallize from the solution.

The phase and chemical composition of the ingot suggests that the solubility of mercury in the oxide melt is extremely low for the experimental parameters used. This hypothesis is also evidenced by the fact that the excess pressures required to prevent damage to the ampoule are close to the gas pressure in the ampoule (Hg—$(4-6)\times10^{-4}$ Pa and O_2—$(2-3)\times10^{-4}$ Pa) calculated assuming that the HgO undergoes complete evaporation and dislocation. These values clearly correspond to the crystallization conditions in our experiments. It should be noted that we did not succeed in obtaining the $Ba_2Cu_3O_{6-x}$ phase at atmospheric pressure.

The external appearance and mechanical properties of the $Ba_2Cu_3O_{6-x}$ crystals ($1.0\times0.5\times0.07$ mm) separated from the ingot are very reminiscent of the Bi-2212 phase and possess high electrical conductivity at room temperature. Results of an x-ray spectral microanalysis performed using a CAMSCAN-4DV scanning electron microscope show that the crystals have the composition $Ba_{2.08-2.29}Cu_3O_y$. An x-ray analysis shows that this phase is an unknown orthorhombic modification $Ba_2Cu_3O_{6-x}$ (see Table I).

The orthorhombic modifications $Ba_2Cu_3O_{6-x}$ studied by us and described in the literature[2,6] are characterized by the parameter $c\approx11.4$ Å, which is present in both sublattices of the superconducting phase $Sr_{0.4}Ca_{13.6}Cu_{24}O_{41+x}$ (Ref. 1) and have different parameters a and b which are multiples of 4.2–4.4 and 3.4–3.7 Å, respectively. For the orthorhombic phase studied the lattice parameters are

TABLE I. Crystallographic Data for $Ba_2Cu_3O_{6-x}$ Structural Modifications

System	Space group	Lattice parameters Å			Source
		a	*b*	*c*	
Cubic	n.d.	18.28	*a*	*a*	Ref. 2
Tetragonal	$P4_2/mcm$	12.98	*a*	9.16	Ref. 6#40-312
Tetragonal	n.d.	16.19	*a*	12.38	Ref. 6#40-313
Orthorhombic	C_{mcm}	4.23	7.3368	11.3863	Ref. 6#40-762
Orthorhombic	n.d.	4.38	3.66	11.36	Ref. 2
Orthorhombic	P_{cmm}	13.065(15)	20.654(21)	11.431(8)	Our data
Monoclinic	P2	8.48	7.33	12.154 $\beta=110.4°$	Ref. 3

$a \approx 4.35\times 3 \approx 13.06$ Å and $b \approx 3.44\times 6 \approx 20.65$ Å. The structure of the monoclinic modification $Ba_2Cu_3O_6$ (Ref. 3) has the parameters $a=4.24\times 2=8.48$ Å, $b=3.67\times 2=7.34$ Å, and $c=11.4/\sin(\beta)=12.15$ Å, which clearly indicates that the structures of these $Ba_2Cu_3O_{6-x}$ modifications are similar. The structure of the monoclinic modification[3] has the same CuO_2 chains distributed along the *a* axis in the *ac* plane as in the superconducting phase $Sr_{0.4}Ca_{13.6}Cu_{24}O_{41+x}$ but the spacing of the Cu–Cu and O–O bonds along the chains is substantially greater (2.82 as opposed to 2.75 Å).

An analysis of the geometric characteristics of the substructures of the composite phases $M_{14}Cu_{24}O_{41+x}$ (M-Bi, Sr, Ca) (Refs. 7–9 and the structure of the monoclinic modification[3] shows that the presence of layers of unconnected CuO_2 chains and interacting two-legged ladders (Cu_2O_3 layers) requires that one of the translations (or d/n) in the plane of the layer is 11.4 Å and that the second (parallel to the chains) is equal to or a multiple of 2.7–2.8 Å or 3.9 Å, respectively. Assuming that such one-dimensional or quasione-dimensional fragments exist in the structure of the orthorhombic phase under study, these cannot be directed along the *a* axis because of the corresponding spacings of Cu–Cu or O–O, which in this case should be either 2.61 Å or 3.26 Å ($2.61\times 5 \approx 3.26\times 4 \approx 13.065$ Å). Plausible spacings are obtained if the CuO_2 chains are distributed in the [110] direction with a period of 24.44 Å ($2.72\times 9 \approx 24.44$ Å). It is less probable that the two-legged ladders are directed in this direction since the Cu–Cu or O–O spacing in this case is ~4.1 Å ($4.07\times 6 \approx 24.44$ Å), which is appreciably greater than 3.9 Å. The results of a detailed structural analysis now being conducted confirm that the structure of the new superconducting phase $Ba_2Cu_3O_{6-x}$ has nonintersecting CuO_2 chains in the [110] and $[\bar{1}10]$ directions.

The superconducting properties of the $Ba_2Cu_3O_{6-x}$ samples were studied by modulated microwave absorption using a Varian E-112 ESR spectrometer. The measurements were made at a frequency of 9.5 GHz and an excitation power up to 50 mW. The first harmonic of the absorption signal at a modulation frequency of 100 kHz was recorded experimentally for amplitudes of modulation of the magnetic field up to 40 Oe. Temperature measurements were made in the range 3–300 K using an Oxford Instruments continuous-flow helium cryostat. The sample temperature was measured to within 0.1 K.

Two single-crystal $Ba_2Cu_3O_{6-x}$ wafers were studied. Crystal No. 1 was grown at $pO_2 \approx 3\times 10^{-4}$ Pa and crystal No. 2 was grown at $pO_2 \approx 1.7\times 10^{-4}$ Pa. The $0.6\times 0.3\times 0.02$ mm surface of sample No. 1 was formed by the cleavage plane and sample No. 2, $1.0\times 0.5\times 0.03$ mm, was formed by the growth surface. The surfaces of both crystals had a complex profile associated with their macroblock structure. The samples were placed in a plastic ampoule so that their planes were perpendicular to a static magnetic field H_0.

Figure 1 gives the first harmonic of the absorption signal

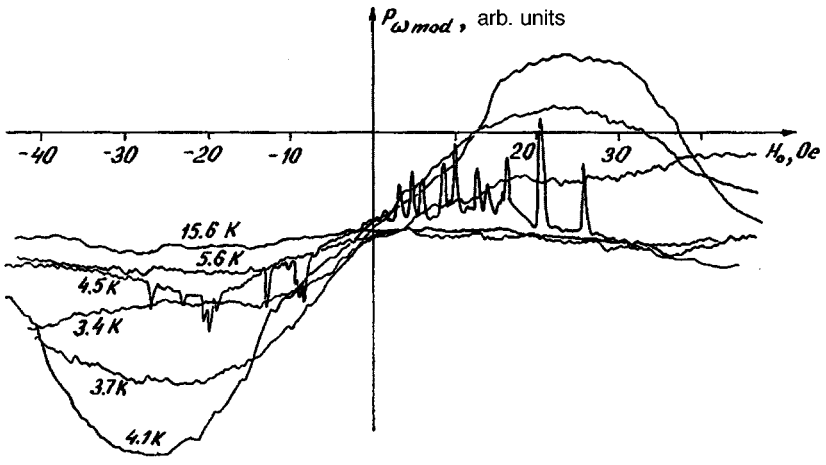

FIG. 1. First harmonic of the microwave absorption signal at the modulation frequency $P_{\omega_{mod}}(H)$ as a function of the static magnetic field for a $Ba_2Cu_3O_{6-x}$ crystal (No. 2); $P_{mw}=20$ mW; $H_{mod}=40$ Oe.

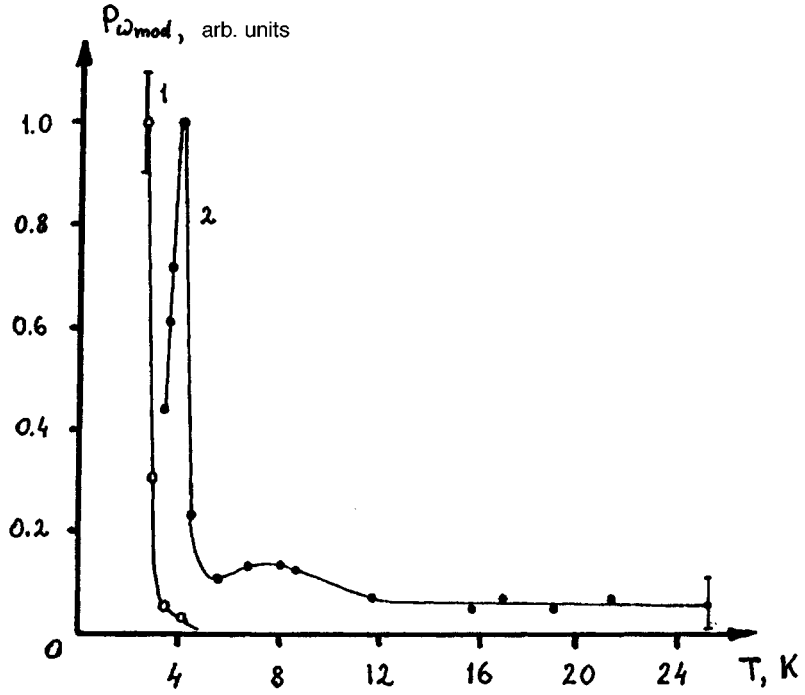

FIG. 2. Temperature dependences of the first harmonic of the microwave absorption signal $P_{\omega_{\mathrm{mod}}}$ for $Ba_2Cu_3O_{6-x}$ crystals: *1*—sample No. 1, *2*—sample No. 2.

$P_{\omega_{\mathrm{mod}}}(H)$ for the second $Ba_2Cu_3O_{6-x}$ sample as a function of the field. The behavior of the microwave absorption in weak magnetic fields is typical of that in superconductors. It does not exhibit the typical hysteresis which may be attributed to the limiting amplitude of the magnetic field modulation which suppresses the hysteresis. The field dependence $P_{\omega_{\mathrm{mod}}}(H)$ of sample No. 2 reveals a noise-like mesostructure at $T \approx 4.5$ K which is attributed to the penetration of vortex ''bundles'' into the superconducting volume of the sample as the magnetic field increases. For sample No. 1 a similar noise-like mesostructure is observed at $T < 3$ K. For both samples the microwave absorption signal does not depend on the angle between the external magnetic field and the plane of the sample.

Temperature dependences of the microwave absorption signal in $Ba_2Cu_3O_{6-x}$ samples are plotted in Fig. 2. For sample No. 1 the signal decreases sharply with increasing temperature and disappears at $T_c = 5 \pm 1$ K. For sample No. 2 we can identify two signals. The first has a sharp peak at $T = 4$ K and disappears at $T_c = 7 \pm 1$ K. This signal is similar to that for sample No. 1 but its characteristic temperature is 2 K higher. The weak signal observed up to $T \leqslant 13$ K has an amplitude an order of magnitude smaller.

These field and temperature dependences of the microwave absorption signal in $Ba_2Cu_3O_{6-x}$ single crystals are typical of single crystals of type II superconductors. However, the lack of dependence of the microwave absorption on the angle between H_0 and the plane of the sample requires explanation. We assume that this lack of an orientational dependence may be attributed to the following factors: first, the complex surface profile of these macroblock single crystals levels out the influence of the demagnetization factor of the sample; second, the need to observe microwave absorption under limiting conditions of excitation and amplification of the spectrometer receiving channel indirectly indicates that the sample is not completely transferred to the superconducting state. This observation is confirmed by the variation of T_c with varying oxygen pressure during synthesis of the samples and by the existence of regions with different superconducting transition temperatures in the second sample. If the randomly distributed superconducting regions do not form an infinite cluster, the demagnetization factor of the single crystal wafer becomes negligible.

The superconductivity of these $Ba_2Cu_3O_{6-x}$ single crystals can only be attributed to the presence of CuO_2 chains formed by edge-sharing copper-oxygen squares in the structure. These chains make it possible for the copper ions to undergo a disproportionation reaction: $Cu^{1+} + Cu^{3+}$, similar to that taking place in the two-dimensional CuO_2 layers in perovskite-like high-temperature superconductors.

The appearance of carriers in the CuO_2 chains may be caused by defects in the barium or oxygen sublattices. It is known (see Ref. 12, for example) that defects in the rare-earth sublattice in 1:2:3 compounds may be a source of carriers in the CuO_2 layers and may give rise to superconductivity. It may be postulated that the differences in the temperature dependences of the modulated microwave absorption in the $Ba_2Cu_3O_{6-x}$ crystals are mainly caused by the oxygen nonstoichiometry which differs for samples synthesized at different oxygen pressures.

The synthesis of superconducting $Ba_2Cu_3O_{6-x}$ single crystals, which are a new class of one-dimensional superconductors, is of fundamental interest from the point of view of identifying the mechanism of superconductivity in superconducting phases with a variable oxygen content.

This work was supported by INTAS (Project No. 94-2007) and by the State Program ''Current Directions in the

Physics of Condensed Media'' (''Poisk'' project).

The authors would like to thank Yu. L. Kreĭtser for carrying out the microprobe analysis of the single crystals and also A. P. Ipatov and E. F. Efimova for technical assistance with the experiments.

[1] S. Maekawa, Science **273**, 1515 (1996).
[2] L. A. Klinkova, Zh. Neorg. Khim. **36**, 1102 (1991).
[3] J. G. Thompson, T. J. White, R. L. Withers *et al.*, Mater. Sci. Forum **14**, 27 (1990).
[4] S. F. Pashin, E. V. Antipov, L. M. Kovba, and Yu. Ya. Skolis, Sverkhprovodimost' KIAE, **2**(7), 102 (1989) [Superconductivity **2**, 116 (1989)].
[5] J. Karpinski *et al.*, Physica C **234**, 10 (1994).
[6] *Powder Diffraction File* (International Center for Diffraction Data, Swarthmore, PA, 1992).
[7] A. F. Jensen, F. K. Larsen, I. B. Johannsen *et al.*, Acta Chem. Scand. **47**, 1179 (1993).
[8] T. Siegrist, L. F. Schneemeyer, S. A. Sunshine *et al.*, Mater. Res. Bull. **23**, 1429 (1988).
[9] E. M. McCarron, M. A. Subramanian, J. C. Calabrese *et al.*, Mater. Res. Bull. **23**, 1355 (1988).
[10] A. A. Romanyukha, Yu. N. Shvachko, and V. V. Ustinov, Usp. Fiz. Nauk. **161**(10), 37 (1991) [Sov. Phys. Usp. **34**, 862 (1991)].
[11] A. I. Veĭnger, S. I. Goloshchapov, S. G. Konnikov, and A. S. Kheĭfets, Sverkhprovodimost' KIAE **5**, 2102 (1992) [Superconductivity **5**, 1995 (1992)].
[12] O. A. Usov, S. I. Goloshchapov, N. F. Kavtenko *et al.*, Fiz. Tverd. Tela (St. Petersburg) **36**, 2328 (1994) [Phys. Solid State **34**, 1266 (1994)].

Translated by R. M. Durham

Reciprocity relation for the effective electrical conductivity of a randomly inhomogeneous medium in the fractal region

A. A. Snarskiĭ, K. V. Slipchenko, and I. V. Bezsudnov

Ukraine National Technical University, ''Kiev Polytechnical Institute'', Kiev
(Submitted July 11, 1997)
Pis'ma Zh. Tekh. Fiz. **23**, 35–39 (December 26, 1997)

An accurate relation for the realization-averaged effective conductivities in the fractal region, i.e., for dimensions smaller than the self-averaging dimension, is obtained for a two-dimensional randomly inhomogeneous medium. For large dimensions this relation yields the Dykhne reciprocity relation. © *1997 American Institute of Physics.* [S1063-7850(97)02212-X]

It is well known that a macroscopically inhomogeneous medium is described by effective characteristics, such as the effective electrical conductivity σ_e which by definition relates the volume-averaged electric fields and currents

$$\langle \mathbf{j}(\mathbf{r})\rangle = \sigma_e \langle \mathbf{e}(\mathbf{r})\rangle, \quad \langle \mathbf{j}(\mathbf{r})\rangle = \int_V \mathbf{j}(\mathbf{r})dV,$$

$$\langle \mathbf{e}(\mathbf{r})\rangle = \int_V \mathbf{e}(\mathbf{r})dV, \tag{1}$$

where $\mathbf{j}(\mathbf{r})$ and $\mathbf{e}(\mathbf{r})$ are the local electric field strength and current density.

The effective electrical conductivity is $\sigma_e = \sigma_1 f(h=\sigma_2/\sigma_1, p)$, where σ_1 and σ_2 are the local phase conductivities for a two-phase medium, and p is the concentration of the phase with conductivity σ_1.

The problem of determining a universal function $f(h,p)/\sigma_1$ near the threshold p_c is similar to determining the critical behavior of the order parameter in the theory of second-order phase transitions and, as in this theory, does not have an accurate solution.

However, as in the theory of second-order phase transitions for a two-dimensional two-phase situation, an accurate Dykhne solution $\sigma_e = \sqrt{\sigma_1\sigma_2}$ (Ref. 1) is known for σ_e and is valid for media with an average geometrically equivalent phase distribution. In terms of flow theory, this solution is that at the percolation threshold $p = p_c = 1/2$; $\tau = (p-p_c)/p_c = 0$.

For $p \neq p_c$ such a solution does not exist but, as was also shown in Ref. 1, a so-called reciprocity relation is obtained which relates σ_e above and below the percolation threshold

$$\sigma_e(\tau)\sigma_e(-\tau) = \sigma_e^2(\tau=0), \quad \sigma_e(\tau=0) = \sqrt{\sigma_1\sigma_2}. \tag{2}$$

On scales $L < \xi$ (smaller than the self-averaging scale), an inhomogeneous medium is mesoscopic and the measured characteristics, including the conductivity, fluctuate from one realization to another. It was shown in Ref. 2 that if the ratio of the phase conductivities is nonzero $h = \sigma_2/\sigma_1 \neq 0$, the realization-averaged effective conductivity $\{\sigma_e\}$ and resistivity $\{\rho_e\}$ are given by

$$\{\sigma_e\} = \sigma_1 \frac{\tau_L+\tau}{2\tau_L}\left(\frac{L}{a_0}\right)^{-l/\nu} + \sigma_2 \frac{\tau_L-\tau}{2\tau_L}\left(\frac{L}{a_0}\right)^{q/\nu},$$

$$\{\rho_e\} = \rho_1 \frac{\tau_L+\tau}{2\tau_L}\left(\frac{L}{a_0}\right)^{l/\nu} + \rho_2 \frac{\tau_L-\tau}{2\tau_L}\left(\frac{L}{a_0}\right)^{-q/\nu}, \quad \rho_i = 1/\sigma_i, \tag{3}$$

where $\tau_L = (L/a_0)^{-1/\nu}$, a_0 is the minimum dimension in the system—the bond length in lattice models. The averages over the realizations are power functions of L, and these systems are described as fractal ones.

It follows from Eq. (3) that although both $\{\sigma_e\}$ and $\{\rho_e\}$ depend strongly on L, their combination, which generalizes the Dykhne reciprocity relation (2) to the fractal region, is almost independent of L

$$\{\sigma_e(\tau,L)\}\{\rho_e(-\tau,L)\}^{-1} = \sigma_e^2(\tau=0, L \gg \xi). \tag{4}$$

Figure 1 gives averages over realizations as a function of various combinations, plotted using formula (3) and numerical analyses.

The reciprocity relation in the fractal region (4) can be strictly proven by using a symmetry transformation.[1] For a medium with the local law $\mathbf{j}(\mathbf{r}) = \sigma(\mathbf{r})\mathbf{e}(\mathbf{r})$, where $\sigma(\mathbf{r} \in O_i) = \sigma_i$ in regions O_1 and O_2, respectively, the transformations

$$\mathbf{j} = \Lambda \mathbf{n} \times \mathbf{e}, \quad \mathbf{e} = \frac{1}{\Lambda}\mathbf{n} \times \mathbf{j}, \quad \Lambda = \sqrt{\sigma_1\sigma_2} \tag{5}$$

convert the initial medium into a ''tilded'' one with the local law $\tilde{\mathbf{j}}(\mathbf{r}) = \tilde{\sigma}(\mathbf{r})\tilde{\mathbf{e}}(\mathbf{r})$, where $\tilde{\sigma}(\mathbf{r} \in O_1) = \sigma(\mathbf{r} \in O_2) = \sigma_2$, $\tilde{\sigma}(\mathbf{r} \in O_2) = \sigma(\mathbf{r} \in O_1) = \sigma_1$, where $\mathbf{n}$ is the unit normal vector. If the phases of the initial medium are colored black and white, the tilded medium will be a negative of the initial medium. Averaging the local law over volume with the characteristic dimension $L \ll \xi$ gives

$$\langle \mathbf{j}(\mathbf{r})\rangle = \hat{\sigma}_e \langle \mathbf{e}(\mathbf{r})\rangle, \quad \hat{\sigma}_e = \sigma_e \hat{1} + \hat{\sigma}_e^a, \tag{6}$$

where the tensor symbol over the effective conductivity stresses the fact that the conductance of each individual realization differs in different directions. Since $\{\hat{\sigma}_e\}$ becomes isotropic after averaging over realizations, it is meaningful to express $\{\hat{\sigma}_e\}$ as two terms (6)—an isotropic component $\sigma_e\hat{1}$ and an anisotropic correction $\hat{\sigma}_e^a$, for which $\{\hat{\sigma}_e^a\} = 0$.

Generalizing the transformations (5) to the volume averages $\langle \mathbf{j}\rangle = \Lambda \mathbf{n} \times \langle \tilde{\mathbf{e}}\rangle$, $\langle \mathbf{e}\rangle = \Lambda^{-1}\mathbf{n} \times \langle \tilde{\mathbf{j}}\rangle$ and applying these to

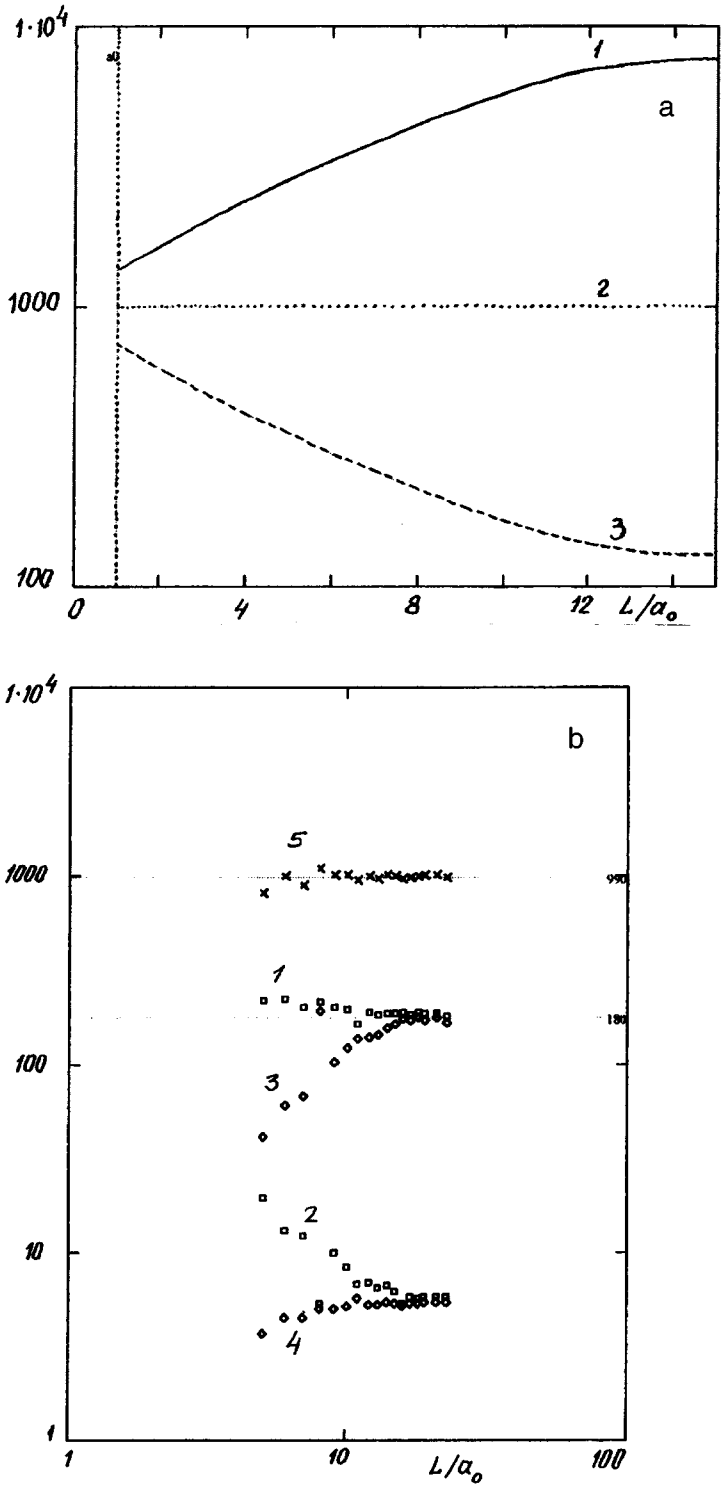

FIG. 1. a—Realization-averaged conductivities and resistivities versus sample dimensions: *1*—$\{\rho_e(\tau=0.15,L)\}/\{\sigma_e(\tau=0.15,L)\}$, *2*—$\{\rho_e(\tau=0.15,L)\}/\{\sigma_e(\tau=-0.15,L)\}$, *3*—$\{\rho_e(\tau=-0.15,L)\}/\{\sigma_e(\tau==-0.15,L)\}$. The L axis gives the correlation length for given parameters, $\xi(\tau=0.15)\approx a_0\tau^{-\nu}\approx 12.5$, the averages over realizations cease to depend on the sample dimension; b—realization-averaged conductivities versus sample dimensions: *1*—$\{G(\tau=0.1,L)\}$, *2*—$\{G(\tau=-0.1,L)\}$; reciprocal realization-averaged resistivities: *3*—$1/\{R(\tau=0.1,L)\}$, *4*—$1/\{R(\tau=-0.1,L)\}$, and *5*—the ratios $\{G(\tau=0.1,L)\}/\{R(\tau=-0.1,L)\}$ obtained by numerical calculations using a square mesh.

formula (6) for a tilded medium, we obtain $\hat{\sigma}_e=\sigma_e\hat{1}+\hat{\sigma}_e^a$, where the isotropic components of the conductivity in this realization are related by

$$\sigma_e(L,\tau)=\Lambda^2/\tilde{\sigma}_e(L,\tau), \quad \Lambda^2=\sqrt{\sigma_1\sigma_2}. \tag{7}$$

We average relation (7) over the realizations and assume that $\{\tilde{\rho}_e(\tau,L)\}=\{\rho_e(-\tau,L)\}$—transformation (5) swaps the phases, i.e., replaces the concentration p with $1-p$ which, assuming $p_c=1/2$, yields the substitution $\tau\to-\tau$. Relation (7) then yields the reciprocity relation in the fractal region (4).

We shall briefly discuss another case. It was shown in Ref. 1 that such a solution also exists for phases with continuously distributed resistivities. If the local conductivity depends on the random variable $\chi(\mathbf{r})=\ln\sigma(\mathbf{r})-\langle\ln\sigma\rangle$ such that the conductivity distribution function is an even function of χ, then for $L\gg\chi$, we have $\sigma_e(L\gg\xi)=\exp\langle\ln\sigma\rangle$.

Using the reasoning put forward above, it can be shown that

$$\{\sigma_e(L)\}/\{\rho_e(L)\} = \sigma_e^2(L \gg \xi). \quad (8)$$

A particular case of these media is a medium with $\sigma(\chi(\mathbf{r})) = \sigma_e e^{\chi(\mathbf{r})}$, with a smooth distribution function $D(\chi) = D(-\chi)$. In this case, we have $\sigma_e(L \gg \xi) = \sigma_0$ and the relations (8) have the form

$$\{\sigma_e(L)\}/\{\rho_e(L)\} = \sigma_0^2, \quad (9)$$

i.e., the ratio of the averages over realizations does not depend on L although each of the averages over realizations, such as $\{\sigma_e\} \sim e^{(L/a_0)^{-1/\nu}}$ (Ref. 3) depends exponentially strongly on L.

The authors would like to than A. N. Lagar'kov and A. K. Sarychev for discussions of issues raised. The work was partly supported by the Russian Fund for Fundamental Research, Grant No. 95-02-04432a.

[1] A. M. Dykhne, Zh. Éksp. Teor. Fiz. **59**, 110 (1970) [Sov. Phys. JETP **32**, 63 (1971)].
[2] A. A. Snarskiĭ and A. E. Morozovskiĭ, Zh. Éksp. Teor. Fiz. **109**, 674 (1996) [JETP **82**, 361 (1996)].
[3] A. A. Snarskiĭ, A. E. Morozovskiĭ, and E. M. Baskin (in press).

Translated by R. M. Durham

Radiation characteristics of a dense cesium plasma in the visible range

F. G. Baksht and V. F. Lapshin

A. F. Ioffe Physicotechnical Institute, Russian Academy of Sciences, St. Petersburg
(Submitted July 28, 1997)
Pis'ma Zh. Tekh. Fiz. **23**, 40–45 (December 26, 1997)

Calculations are made of the radiation spectrum from a cesium plasma column. It is shown that this plasma may serve as a light source with a high proportion of visible radiation and an almost continuous spectrum. The visible spectrum is formed mainly by bright recombination $6P$ and $5D$ continua whose thresholds are shifted in the long-wavelength direction. © *1997 American Institute of Physics.* [S1063-7850(97)02312-4]

1. The development of ecologically clean, mercury-free light sources is a topical problem is contemporary lighting engineering. One method of solving this problem involves using pulse-periodic striking of a high-pressure arc.[1] In Refs. 2 and 3 a pulse-periodic discharge in Na vapor with added Xe was used to demonstrate that, even when the power deposited in the discharge column is comparatively low ($P=10-60$ W/cm), it is possible to obtain a plasma with a high temperature ($T\cong 6000-7000$ K) and high charged particle concentration ($n_i\cong(2-5)\times 10^{17}$ cm^{-3}). Under these conditions a state of local thermodynamic equilibrium is established in the plasma with a comparatively low degree of plasma nonideality $\Gamma=(e^2/r_D)/(3/2kT)\leqslant 0.2$. Although the thermodynamic functions of this plasma still differ little from those of an ideal plasma, interaction between the plasma particles already has an appreciable influence on the visible radiation spectrum. Here we calculate the radiation spectrum for this type of plasma formed by ionization of Cs vapor. It is shown that as the concentration increases in the cesium plasma, the fraction of visible radiation increases substantially mainly as a result of the formation of bright $6P$ and $5D$ continua and a long-wavelength shift of the thresholds of these continua. The resultant spectrum has a substantially higher color rendition index compared with a Na plasma. Additional advantages of cesium as an emitting gas are related to its low thermal conductivity and larger cross section for resonant charge transfer of Cs^+ ions. This means that to a considerable extent, a buffer gas is unnecessary, especially expensive xenon.

2. Here we calculate the spectral density F_λ of the radial radiation flux emitted by the surface of a homogeneous cesium plasma column. Under conditions of local thermal equilibrium, the value of F_λ with allowance for Kirchhoff's law may be defined as

$$F_\lambda = F_{\lambda P}(T)\varepsilon(\tau_\lambda). \tag{1}$$

Here $F_{\lambda P}(T)$ is Planck's function, $\tau_\lambda = 2Rk_\lambda$ is the optical thickness, R is the column radius, k_λ is the spectral absorption coefficient,

$$\varepsilon(\tau_\lambda)=\frac{4}{\pi}\int_0^{\pi/2} d\theta \int_0^{\tau_\lambda \cos\theta} dx \int_0^{\pi/2} d\psi \cos\psi \exp(-x/\cos\psi) \tag{2}$$

is the spectral emissivity ($0\leqslant\varepsilon(\tau_\lambda)\leqslant 1$). The spectral absorption coefficient k_λ was calculated as the sum of the absorption coefficients corresponding to free–bound, bound–free, and bound–bound transitions:

$$k_\lambda = k_\lambda^{(\mathrm{ff})} + k_\lambda^{(\mathrm{bf})} + k_\lambda^{(\mathrm{bb})}. \tag{3}$$

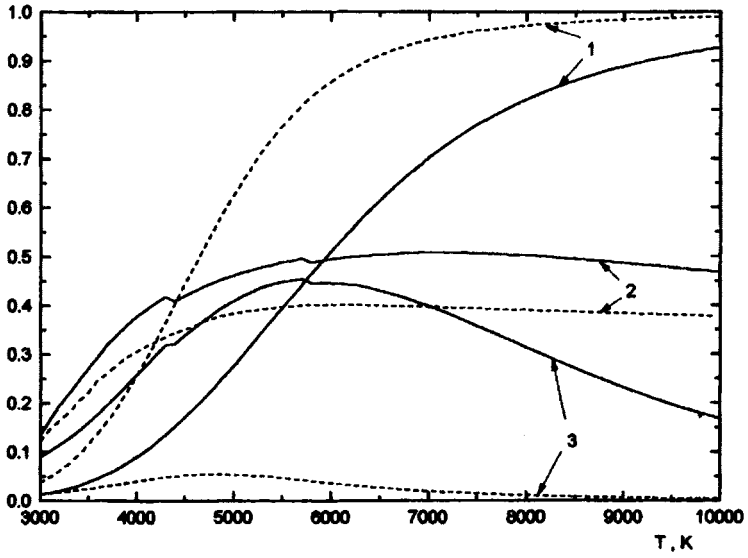

FIG. 1. Main radiative characteristics of a cesium plasma column with $R=2.5$ mm: *1*—β, *2*—η_{vis}, *3*—ε_T. Solid curves—$n=8\times 10^{17}$ cm^{-3}, dashed curves—$n=8\times 10^{16}$ cm^{-3}.

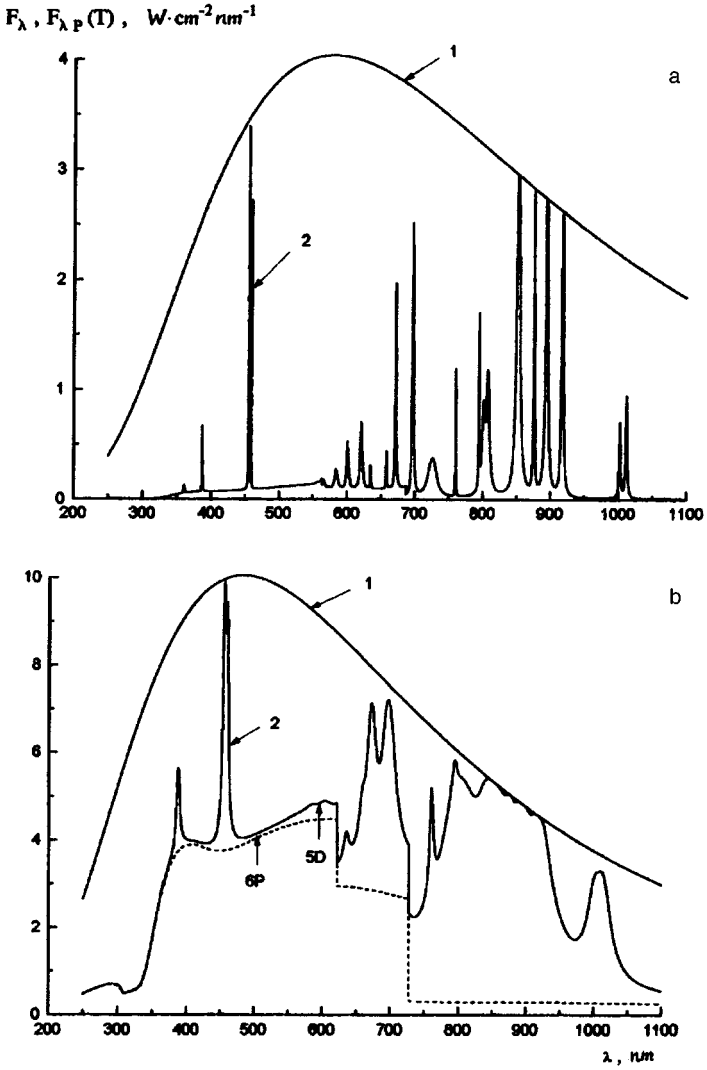

FIG. 2. Radiation spectrum of a cesium plasma column with $R=2.5$ mm: *1*—$F_{\lambda P}(T)$, *2*—F_λ; a—$n=-8\times10^{16}$ cm^{-3}, $T=5000$ K, b—$n=8\times10^{17}$ cm^{-3}, and $T=6000$ K.

The value of $k_\lambda^{(\mathrm{ff})}$ is taken from Ref. 4. The coefficient $k_\lambda^{(\mathrm{bb})}$ was determined with allowance for $6S\rightarrow nP$ $(n\geqslant 6)$, $6P\rightarrow nD$ $(n\geqslant 6)$, $6P\rightarrow nS$ $(n\geqslant 7)$, and $5D\rightarrow nF$ $(n\geqslant 4)$ transitions in the cesium atom with due regard to the fine structure of the levels. Two broadening mechanisms were assumed for the $(6S\rightarrow 6P)$ resonant line: broadening by Cs atoms with resonant transfer of excitation[5] and Stark broadening.[6] Only Stark broadening was assumed for all the other lines. The coefficient $k_\lambda^{(\mathrm{bf})}$ was determined with allowance for photoionization of the $6S$, $7S$, $6P$, $7P$, $8P$, $5D$, $6D$, $7D$, $4F$, $5F$, and $5G$ states: $k_\lambda^{(\mathrm{bf})}=\Sigma_\gamma n_\gamma \sigma_\gamma^{(\mathrm{ph})}(\lambda)$. The fine structure of the levels was neglected. The photoionization cross section $\sigma_\gamma^{(\mathrm{ph})}(\lambda)$ was determined in terms of the spectral density of the oscillator strengths calculated in Ref. 7

$$\sigma_\gamma^{(\mathrm{ph})}(E)=4\pi^2\alpha a_0^2\,\frac{df}{d(E/\mathrm{Ry})}, \tag{4}$$

where Ry is the Rydberg constant, a_0 is the Bohr radius, $\alpha=1/137$, and E is the photoelectron energy. The concentration n_γ of excited atoms was determined by the Saha–Boltzmann method. The calculations took account of the reduction in the ionization potential $\Delta E_i=e^2/r_D$ in the Debye approximation, but neglected the decrease in the ionization potential as a result of interaction between charged particles and neutral Cs atoms, which is comparatively unimportant under these particular conditions (in this context, see Ref. 8, p. 50, for example).

3. We shall now discuss separately the method of calculating k_λ near the photoionization threshold. We analyze the spectrum of highly excited bound states γ' adjacent to the continuum, assuming that in a dense plasma these states are established with a certain probability $W_{\gamma'}<1$, which is the result of plasma microfields acting on the atoms (see Refs. 9 and 10). Thus, $1-W_{\gamma'}$ is the probability of a free state rather than a bound one appearing in the continuous spectrum. The absorption coefficients for a series of spectral lines converging toward the photoionization threshold therefore have the form: $k^{(\mathrm{bb})}=W_{\gamma'}n_\gamma\sigma_{\gamma\gamma'}$, $k^{(\mathrm{bf})}=(1-W_{\gamma'})n_\gamma\sigma_\gamma^{(\mathrm{ph})}$, where $\sigma_{\gamma\gamma'}$ is the photoionization cross section corresponding to the transition $\gamma\rightarrow\gamma'$. In a dense plasma, the Stark line broadening causes merging of the higher terms in the spectral series which converge toward the photoionization threshold. Here, we assumed as an approximation that the lines

merge if the sum of the ''electron'' half-widths of neighboring lines in the spectral series is greater than the spacing between the centers of the lines. When the lines merge, the cross section $\sigma_{\gamma\gamma'}$ is the same as the photoionization cross section (4). Thus, in the region where the lines merge we find $k^{(\mathrm{bb})}+k^{(\mathrm{bf})}=n_\gamma\sigma_\gamma^{(\mathrm{ph})}$, i.e., in this region the total absorption coefficient does not depend on the probability $W_{\gamma'}$ of the states being appearing in the discrete spectrum. This factor is important because the probabilities $W_{\gamma'}$ are calculated approximately using model representations.

4. The results of the calculations are illustrated in Figs. 1 and 2. Figure 1 gives the main radiative characteristics η_{vis} and ε_T of a homogeneous plasma column of radius $R=2.5$ mm as a function of the plasma temperature T for two values of the total cesium concentration $n=n_i+n_a$:

$$\eta_{\mathrm{vis}}=\frac{1}{F}\int_{\lambda_1}^{\lambda_2}F_\lambda d\lambda \quad \text{and} \quad \varepsilon_T=\frac{F}{F_P},$$

where

$$F=\int_{\lambda_{\min}}^{\lambda_{\max}}F_\lambda d\lambda, \quad F_P=\sigma_{S.B}T^4.$$

Here η_{vis} is the fraction of the visible radiation in the total radiation flux, ε_T is the integrated emissivity, $\sigma_{S.B}$ is the Stefan–Boltzmann constant, $\lambda_1=400$ nm, $\lambda_2=750$ nm, $\lambda_{\min}=250$ nm, and $\lambda_{\max}=1500$ nm. Also plotted is the degree of ionization of the plasma $\beta=n_i/n$. It can be seen that the optimum conditions for achieving good radiative characteristics are achieved at the maximum ε_T (where $\beta\cong 0.5$). Here a fairly high value of η_{vis} is combined with optimum utilization of the plasma radiative capacity at the given temperature. The corresponding plasma radiation spectra for two values of n are shown in Fig. 2. It can be seen from a comparison of Figs. 2a and 2b that as n increases, the plasma radiation spectrum is transformed from a line spectrum to a continuous one and approaches black body radiation. This transformation of the spectrum is mainly caused by the appearance of bright $6P$ and $5D$ continua and by the thresholds of these continua being shifted in the long-wavelength direction. To illustrate this, the dashed curve in Fig. 2b shows the spectrum when allowance is only made for absorption in the continuous spectrum and the arrows indicate the thresholds of the $6P$ and $5D$ continua for an isolated atom. The spectrum calculated in Fig. 2b corresponds to $n_i\cong 4\times 10^{17}$ cm^{-3}. Note that at concentrations $n_i\geqslant 10^{18}$ cm^{-3} the plasma becomes strongly nonideal. In the plasma microfields the deep levels of the cesium atom begin to decay and the intensity of the recombination continuums may decrease (similar effects in a dense rare-gas plasma were observed in Ref. 11). This range of topics requires further investigation.

To conclude, we have shown that in a certain range of concentrations and temperatures a cesium plasma may serve as a light source with a high fraction of visible radiation and a high color rendition index.

The authors would like to thank V. G. Ivanov for useful discussions of the work.

[1] Yu. B. Aĭzenberg, Svetotekhnika, No. 5–6, 1 (1993).
[2] F. G. Baksht and V. F. Lapshin, Zh. Tekh. Fiz. **66**(11), 170 (1996) [Tech. Phys. **41**, 1177 (1996)].
[3] F. G. Baksht and V. F. Lapshin, Zh. Tekh. Fiz. **67**(9), 22 (1997) [Tech. Phys. **42**, 1004 (1997)].
[4] I. I. Sobelman *Atomic Spectra and Radiative Transitions* (Springer-Verlag, Berlin, 1979) [Russ. original, Nauka, Moscow 1977].
[5] I. I. Sobelman, L. A. Vaĭnshtein, and E. A. Yukov, *Excitation of Atoms and Broadening of Spectral Lines* (Springer-Verlag, Berlin, 1981) [Russ. original, Nauka, Moscow (1979].
[6] H. R. Griem, *Spectral Line Broadening by Plasmas* (Academic Press, New York, 1974; Mir, Moscow, 1978).
[7] S. T. Lahiri and S. T. Manson, Phys. Rev. A **33**, 3151 (1986).
[8] A. G. Khrapak and I. T. Yakubov, *Electrons in Dense Gases and Plasmas* [in Russian], Nauka, Moscow (1981).
[9] V. Sevastyanenko, Contrib. Plasma Phys. **25**, 151 (1985).
[10] L. G. D'yachkov, Opt. Spektrosk. **81**, 885 (1996) [Opt. Spectrosc. **81**, 809 (1996)].
[11] V. E. Gavrilov, Opt. Spektrosk. **74**, 1028 (1993) [Opt. Spectrosc. **74**, 609 (1993)].

Translated by R. M. Durham

Some laws governing laser beam ignition of an ethylene stream in air

G. I. Kozlov

Institute of Problems in Mechanics, Russian Academy of Sciences, Moscow
(Submitted January 13, 1997)
Pis'ma Zh. Tekh. Fiz. **23**, 46–50 (December 26, 1997)

The process of laser beam ignition of an ethylene stream in air has been studied experimentally. It has been established that the ignition process has two stages and the threshold power of the igniting laser radiation is extremely low.
[S1063-7850(97)02412-9]

A promising line of research involves studying the effect of laser radiation on the ignition and combustion processes of fuel gas mixtures. Practical interest is already being directed toward aspects of the initiation of combustion and explosion processes, the safe use of laser scalpels, the use of laser radiation to develop alternative ignition systems, the synthesis of various materials, and other applications.

Here an attempt is made to study experimentally the characteristics of the laser beam ignition of an ethylene stream in atmospheric air. On account of its practical importance, this aspect has recently been examined in various studies[1–3] but these have not touched on the fundamental issues involved in studying the ignition mechanism in a laser beam.

The experiments were carried out using a planar flame burner 6 cm in diameter and a 35 W cw gas-discharge CO_2 laser.[2] Ethylene was supplied via the burner and flowed out into the atmosphere, intersecting the focusing region of the laser beam at the exit from the burner. The CO_2 laser beam was focused by a KCl salt lens, having a focal length of 7.5 cm, into a spot approximately 0.4 mm in diameter. By moving the lens, the focusing region could be moved over the diameter of the burner and could be localized at various points in the stream approximately 1.5 cm above the exit cross section of the burner.

The evolution of the ignition process was recorded with a video camera. An analysis of the video frames yielded some important conclusions on the evolution of the laser beam ignition process in an ethylene stream in air.

In the first series of experiments, the focusing region was located approximately 1.0 cm from the edge of the burner, in the zone where the ethylene stream mixed with the surrounding air. It was established that, above a certain threshold laser beam power, stable ignition of the fuel mixture occurred after an induction period had elapsed. For these conditions the threshold power P_t for initiation of the ignition process was unexpectedly low, only 11.5 W. However, this power corresponds to a fairly high threshold laser radiation intensity at the focus, $S_t \approx 10^4$ W/cm^2.

It was found that when the focus was shifted toward the center of the burner inside the ethylene stream, ignition occurred not at the focus, but in the convergent part of the light cone, i.e., at the point where the composition of the fuel mixture was optimum for initiation of the ignition process. In experiments where the focusing region was shifted deep into the ethylene stream, ignition occurred only 2.5 cm from the surface of the lens. This observation was surprising because at this point the laser radiation intensity was extremely low and did not exceed $S_t \approx 40$ W/cm^2. Thus, for large laser beam cross sections the threshold laser radiation intensity for ignition falls sharply (by two or three orders of magnitude!).

This strong dependence of S_t on the beam diameter $2r_0$ may be explained as follows. Let us imagine that the ignition region is a sphere of radius r_0. Then, the energy release inside this sphere will be approximately $P_t \varkappa 2r_0$ (where $\varkappa$ is the coefficient of absorption of laser radiation by the fuel mixture). Assuming that energy is lost by heat conduction, the energy losses for a spherical ignition region are $4\pi\theta r_0$ (here θ is the heat flux potential for the fuel mixture). Equating the energy release to the heat losses, we find that S_t is related to the radius r_0 by the following expressions:

$$S_t \approx \frac{2\theta}{\varkappa r_0^2},$$

which, to a first approximation, correlates reasonably well with the experiment.

Another characteristic feature deduced from an analysis of these experiments involves the evolution of the ignition process. Figure 1 shows two most typical video frames of the process when the focus was situated 1.0 cm from the edge of the burner. An examination of the video frames shows that in this case, the ignition process is initiated in the focusing region of the laser beam. At the first stage of the process (see Fig. 1a) a nucleating center with a light blue glow forms at the focus and its front rapidly propagates in all directions at a velocity exceeding both the propagation velocity of cold flames and the maximum flame propagation velocity in ethylene-air mixtures. The expansion velocity of the boundary of the pale blue zone is approximately 1 m/s and is probably determined by the diffusion of active particles—hydrogen atoms.

At the second stage of the ignition evolution process, as can be seen from the next frame taken after 40 ms and shown in Fig. 1b, a bright explosive orange-yellow flash is observed within the pale blue zone and its front propagates across the entire region of the fuel mixture.

This pattern of evolution of the ignition process in a laser beam indicates a complex thermokinetic mechanism. In fact, if the laser beam acted only as a heat source, we should observe the formation of a flame front near the focus which would then propagate throughout the entire volume of the fuel mixture. However, details of the video recording of the

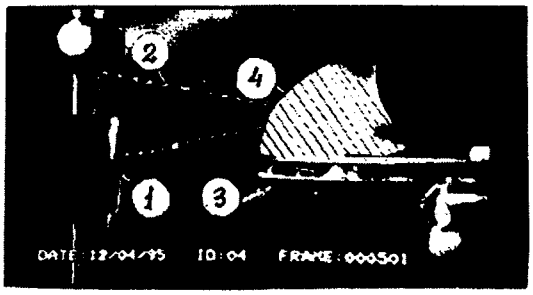

a

b

FIG. 1. Video frames of the laser beam ignition of an ethylene stream: *1*—lens, *2*—contours of focused laser beam, *3*—exit cross section of burner, *4*—ignition region (hatched area—light blue zone, unhatched area at center—orange zone.

ignition evolution process indicate a fundamentally different, two-stage explosive ignition process. At the first stage of ignition, the gas is weakly heated during its residence time in the laser beam and estimates show that this heating does not exceed approximately 300 °C. Under these conditions cold-flame oxidizing processes take place in the mixture with the formation of intermediate products such as aldehydes and peroxides.

At the second stage of the process, these substances probably dissociate to form a large quantity of active atoms and radicals. These active particles initiate a chain-branching chemical process in the pale blue zone, which leads to the progressive acceleration of the chemical conversions and the formation of various stable intermediate products, including acetylene. The bright orange flash at this stage of the ignition process is probably caused by an acetylene dissociation reaction. The flash has a volume nature and is accompanied by an appreciable release of energy, expansion of the reaction products in the ignition nucleus, and by turbulence of the entire stream.

The ignition region is then transformed into a jet of diffusive flame which completely prevents oxygen in the air from penetrating into that part of the laser beam where ignition occurred. The action of the laser radiation on the ethylene stream then becomes completely different, and this will be discussed in later publications.

To sum up, these results indicate that the mechanism of laser beam ignition of an ethylene stream in air is highly specific, the threshold beam powers are low, and the ignition process is a two-stage explosive process which requires further in-depth study.

To conclude, the author would like to thank the United Kingdom for giving him a grant to carry out this research at Imperial College, University of London, in collaboration with Prof. F. Weinberg and Doctors F. Carleton and M. Carabine.

[1] G. I. Kozlov, V. A. Kuznetsov, and A. D. Sokurenko, Pis'ma Zh. Tekh. Fiz. **17**(11), 25 (1991) [Sov. Tech. Phys. Lett. **17**, 398 (1991)].
[2] M. D. Carabine, F. B. Carleton, G. I. Kozlov, and F. J. Weinberg, Joint Meeting of the Portuguese, British, Spanish, and Swedish Section of the Combustion Institute, Madeira, Portugal, 1996, pp. 21.7.1–21.7.4.
[3] M. A. Tanoff, M. D. Smooke, R. E. Teets, and J. A. Sell, Combust. Flame **103**, 253 (1995).

Translated by R. M. Durham

Evolution of deformation domains and kinetics of fatigue fracture of Duralumin polycrystals at the mesoscopic level

V. E. Panin, V. S. Pleshanov, and V. V. Kibitkin

Institute of Physics of Strength of Materials and Materials Science, Siberian Branch of the Russian Academy of Sciences, Tomsk
(Submitted May 14, 1997)
Pis'ma Zh. Tekh. Fiz. **23**, 51–57 (December 26, 1997)

Laws governing the buildup of fatigue fracture under cyclic loading of aluminum alloy polycrystals under conditions of multicycle fatigue have been studied by analyzing the space-time dynamics of mesoscopic structures. It has been shown that under the periodic action of an external mechanical field, deformation domains form in the material at the mesoscopic level. The evolution of these dynamic mesoscopic domain substructures determines the kinetics of the fatigue fracture of the polycrystals.
[S1063-7850(97)02512-3]

1. INTRODUCTION

Mechanisms of fatigue fracture in solids have conventionally been studied along two lines of research on different scales.[1–4] At the microscopic level, concerned with the physics of plasticity, crystal structure defects, their interaction and evolution are studied using dislocation theory. At the macroscopic level of the mechanics of a continuous medium and the mechanics of damage, the overall characteristics of the solid are investigated without regard to its internal structure. Both these lines of research have achieved considerable success but so far, the processes taking place in a crystalline material under cyclic loading at the microscopic level have not been related theoretically or experimentally to those taking place at the macroscopic level.

Here we propose a new approach to study the laws governing the fatigue-induced loss of integrity based on concepts of the physical mesomechanics of materials.[5] According to this approach, the carrier of plastic deformation in a solid at the intermediate (mesoscopic) level is a bulk structural element (mesovolume) which exhibits both translational and rotational deformation modes. The motion of these mesovolumes may be described and analyzed using the equations of mechanics for a continuous medium while the accommodation processes within the mesovolumes and at their interfaces may be analyzed using dislocation theory at the microscopic level. When a load is applied to the surface of materials, space-time mesoscopic substructures are formed and an analysis of their dynamics may form the basis for studying the mechanisms of deformation and fatigue fracture under cyclic loading.

Experimental investigations of mesoscopic mechanisms of fatigue fracture of polycrystals were carried out under multicycle fatigue conditions using $75\times10\times0.8$ mm plane samples of D16 AT structural aluminum alloy. The alloy had an average grain size of 18 μm, with 250 MPa yield stress, 370 MPa tensile strength, 870 MPa microhardness, and 13%

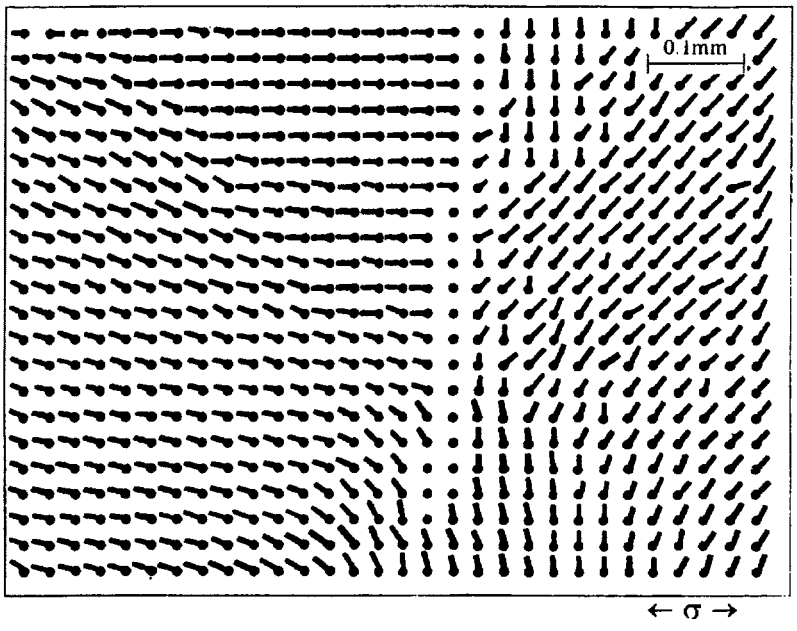

FIG. 1. Deformation domains ahead of the front of a surface fatigue crack (crack above). Number of loading cycles $N=60\times10^3$.

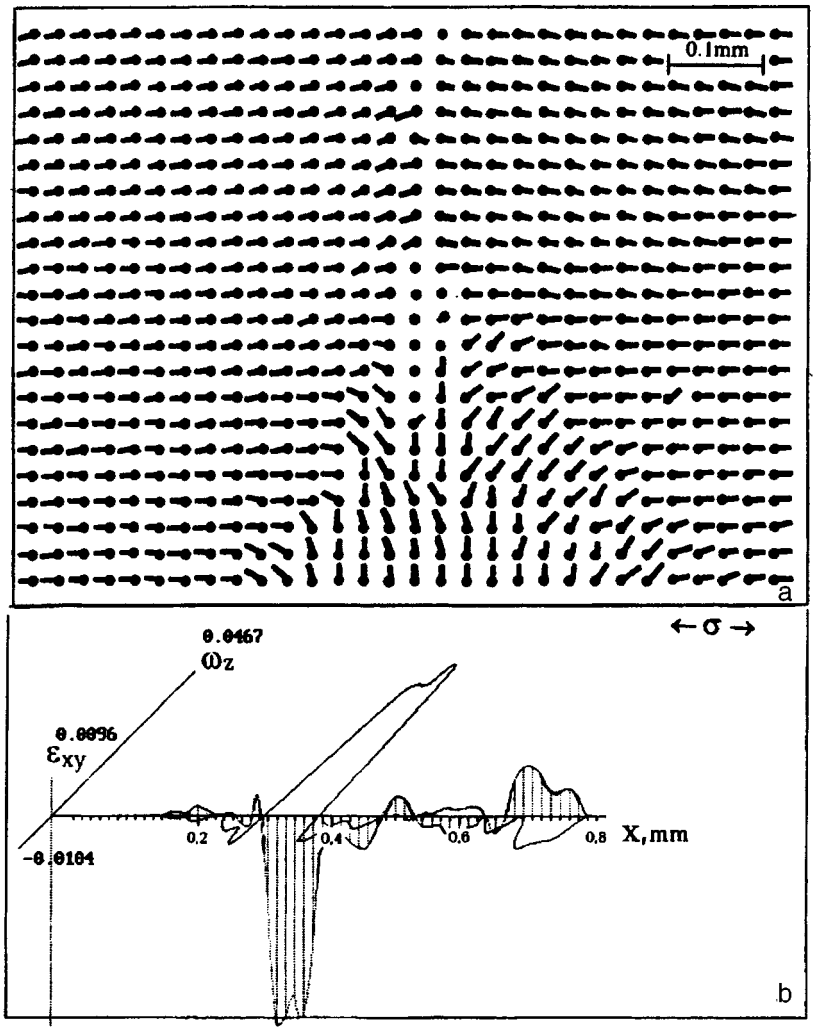

FIG. 2. Domain mesosubstructure near main crack (a) and distribution of local shears ε_{xy} and rotations ω_z ahead of crack tip (b). $N=86\times10^3$.

plasticity. A hole 2 mm in diameter was made in the center of the sample to introduce a stress macroconcentrator to initiate the damage buildup processes. The tests were carried out using a cyclic stretching (push-pull) system with a load of 50 ± 50 MPa at a frequency of 1.5 Hz. The laws governing the formation of the mesostructures were studied using an optical imaging measuring system[5] which can construct the fields of the displacement vectors of elementary sections of the surface and can calculate the distributions of the local components of the plastic distortion tensor, i.e. the longitudinal ε_{xx}, transverse ε_{yy}, shear ε_{xy}, and rotational ω_z components.

2. RESULTS AND DISCUSSION

The results indicate that the process of fatigue fracture of Duralumin polycrystals at the mesoscopic level may be divided into five main stages of evolution:

—randomly distributed zones of plastic shear in the region where the transverse cross section of the sample has a minimum;

—nucleation and quasibrittle growth of surface microcracks in the local area of the plastic shear;

—brittle-plastic growth of surface cracks;

—evolution of a main fatigue crack;

—plastic elongation and final rupture.

Each stage has a specific type of mesoscopic structure forming on the surface of the loaded polycrystal.

The first stage involves the formation of a system of randomly distributed zones of between 3–5 and 15–25 μm with localized plastic shear, in that area of the material subject to the maximum tensile stresses. During application of the load, these zones alter their position, which leads to deformation hardening of the material, nucleation and quasibrittle growth of surface fatigue microcracks at the second stage of damage. Almost no plastic deformation is identified experimentally in the vicinity of these cracks. These surface cracks develop in a thin surface layer associated with an Al_2O_3 oxide film whose role in the evolution of deformation at the mesoscopic level was studied in Ref. 6 for aluminum polycrystals.

After the surface crack has reached a certain length (0.4–0.5 mm), appreciable plastic deformation is observed ahead of its tip. This indicates the onset of the third stage where the integrity of the polycrystal is impaired. A characteristic block mesosubstructure forms in the stressed material ahead of the crack front, as can be seen in the field of the

displacement vectors shown in Fig. 1. In accordance with the ideas put forward in Ref. 7, these blocks may be interpreted as bulk mesodefects — deformation zones formed in polycrystals in zones of highly localized plastic shear and propagating as an entire ''shear + rotation'' system. The formation of these deformation domains is the most important stage in the fatigue fracture process at the mesoscopic level. It indicates the onset of bulk displacements in the material in the local stress concentrator zone and precedes the appearance of a fatigue crack in this part of the polycrystal. Studies have shown that the trajectory of the fatigue crack is determined by the interdomain walls along the normal to the direction of maximum tensile stresses. This behavior shows good agreement with the theoretical results of Ref. 8.

In an external mechanical field, the deformation domains tend to become oriented in the direction of the loading axis during a cyclic loading process. This is responsible for the fourth stage of the damage process — transformation of a surface fatigue crack into a through (main) crack with its subsequent evolution. At the mesoscopic level, the propagation of a main surface crack may be described from the point of view of the dynamic domain substructures by a ''shear-rotation-tear'' system as opposed to the conventional ''shear-tear'' system.[9] The deformation domains adjacent to the edges of the main crack are displaced in the direction of the applied load, thereby achieving a normal tearing mechanism (Fig. 2a). This is preceded by spatial displacement of the domains by a ''shear-rotation'' system, as can be seen clearly in Fig. 2b. Near the front of the crack the domains exhibit varying orientation and undergo translational-rotational motion with the shear ε_{xy} and rotational ω_z deformation modes highly localized in front of the crack tip. An essential accommodation process involves the formation of a free surface at the tip of the main crack by a ''shear + rotation'' mechanism. In this case, allowance for the rotational component is fundamentally important and is fully consistent with the concepts of physical mesomechanics whereby rotational deformation modes form the basis of material damage processes.

The final, fifth stage of the fatigue fracture process involves the formation of a triangular zone of plastic elongation between the tip of the main crack and the side surface of the sample.[10] The evolution of the main crack then reaches a bifurcation point and as a result of the formation of a free surface at the front of the fatigue crack, the fracture is replaced by plastic shears in the direction of maximum tangential stresses. This effect is caused by overloading of the sample (in excess of the yield stress) when the main crack is 2.0–2.2 mm long. The conjugate boundaries of the elongation zone are oriented at angles of 45° and 1.35° to the loading axis. Mesodefects are displaced toward the tip of the crack along these boundaries by a shear mechanism. Under further cyclic loading, the sample finally ruptures in the plastic elongation zone as a result of the growth of a rotational deformation mode.

3. CONCLUSIONS

These results suggest that the kinetics of fatigue fracture of Duralumin polycrystals is determined by the evolution of a dynamic mesoscopic domain substructure by a ''shear-rotation-tear'' system. The onset of fatigue fracture is preceded by the formation of transverse microcracks in the brittle surface layer associated with an Al_2O_3 surface oxide film.

This work was supported by the Russian Fund for Fundamental Research (Project No. 96-01-00902).

[1] V. S. Ivanova, S. E. Gurevich, I. M. Kop'ev *et al.*, *Fatigue and Embrittlement of Metallic Materials* [in Russian], Nauka, Moscow (1968).
[2] V. T. Troshchenko, *Fatigue and Inelasticity of Metals* [in Russian], Naukova Dumka, Kiev (1971).
[3] *Damage*, edited by G. Libovits [Russ. transl.], Vol. 3, Mir, Moscow (1973).
[4] V. S. Ivanova, A. S. Balankin, A. A. Bunin *et al.*, *Synergetics and Fractals in Materials Sciences* [in Russian], Nauka, Moscow (1994).
[5] V. E. Panin, V. E. Egorushkin, P. V. Makarov *et al.*, *Physical Mesomechanics and Computer-Aided Design of Materials*, Vol. 1 [in Russian], Nauka, Novosibirsk (1995)
[6] V. E. Panin and S. V. Panin, Izv. Vyssh. Uchebn. Zaved. Fiz. No. 1, 31 (1997).
[7] V. E. Panin and S. V. Panin, Izv. Vyssh. Uchebn. Zaved. Fiz. **1**, 31 (1997).
[8] V. E. Panin, S. V. Panin and A. I. Mamaev, Dokl. Akad. Nauk **350**(1), 35 (1996) [Phys. Dokl. **41**, 392 (1996)
[9] F. Erdogan and G. C. Sih, J. Basic Eng. **85**, 519 (1963).
[10] B. Tomkins, Metal Sci. **13**, 387 (1979).
[11] V. A. Vaĭnshtok, A. Ya. Krasovskiĭ, G. N. Nadezhdin *et al.*, Prob. Prochnost. No. 11, 101 (1978).

Translated by R. M. Durham

Dependence of electron and hole lifetimes on the majority recombination impurity concentration in the presence of auxiliary carrier trapping centers

V. A. Kholodnov and P. S. Serebrennikov

Theory Department, State Science Center of the Russian Federation, Orion State Scientific-Industrial Organization, Moscow
(Submitted July 30, 1997)
Pis'ma Zh. Tekh. Fiz. **23**, 58–63 (December 26, 1997)

It has been shown that a substantial increase in carrier lifetimes in a certain range of increasing concentration of recombination impurities may also take place in the presence of auxiliary (background) deep impurities, and two maxima may even be observed. © *1997 American Institute of Physics.* [S1063-7850(97)02612-8]

It was shown theoretically in Refs. 1–3 that when nonequilibrium carriers undergo impurity recombination in semiconductors,[4–7] the lifetimes of the electrons τ_n and holes τ_p may increase by several orders of magnitude as the concentration N of the recombination centers increases. Significantly, the position of the maxima of the functions $\tau_n(N)$ and $\tau_p(N)$ coincides with the value of N for which the ambipolar mobility of the carriers vanishes, as was first reported in the symposium proceedings.[8] Consequently, even under conditions of strong carrier recombination at the current contacts[9] the well-known negative property of intrinsic photoconductivity of a semiconductor[10–12] is suppressed—the photoelectric gain saturates with increasing electron field strength E.

These results were obtained using a simplified model which includes shallow, completely ionized donors with the concentration N_D and negative, singly charged and neutral deep acceptors with the concentrations N_- and $N_0=N-N_-$ (single-level approximation). For the sections of increasing lifetimes[2,3] we find $\sigma\equiv N_-^e/N_0^e\gg 1$, where N_-^e and N_0^e are the corresponding equilibrium concentrations. This inequality implies that capture of electrons by charged centers may play a significant role, which was neglected in Refs. 1–3. This capture process was taken into account in Ref. 13 where the approximation of two-level recombination impurities was used to show that, as for the single-level problem,[1–3] the curves $\tau_n(N)$ and $\tau_p(N)$ may have a section of very large increase. For this reason capture of electrons by auxiliary (background) impurities may also play a significant role. Thus, it is appropriate to determine whether the functions $\tau_n(N)$ and $\tau_p(N)$ may become highly nonmonotonic in the presence of auxiliary trapping centers and this forms the subject of the present study. As in Refs. 1–3, and 13, we consider a slight deviation from the equilibrium state which is achieved, for example, when weak optical radiation is recorded using semiconductors. Unlike Refs. 1–3, we assume that there is another (auxiliary) deep impurity, say an acceptor, which may be in the same charge states as the majority impurity, and has the concentration $\tilde{N}\ll N_D$ (the parameters of the auxiliary impurity are denoted by tildes).

Let us suppose that nonequilibrium electrons and holes, having the concentrations $\Delta n=n-n_e$ and $\Delta p=p-p_e$, are formed only by interband lasing or by injection from contacts (n and p are the electron and hole concentrations, and n_e and p_e are their equilibrium values). Neutral atoms of the majority and auxiliary impurities capture electrons with the probabilities w_n and $\tilde{w}_n$, and also generate holes thermally. Charged centers capture holes with the probabilities w_p and $\tilde{w}_p$, and also generate electrons thermally. Thus, the recombination velocities of the electrons $R_n=\mathscr{R}_n+\tilde{\mathscr{R}}_n$ and holes $R_p=\mathscr{R}_p+\tilde{\mathscr{R}}_p$ consist of the corresponding partial components

$$\mathscr{R}_n=w_n nN_0-w_n\delta^{-1}n_eN_-,\quad \tilde{\mathscr{R}}_n=\tilde{w}_n n\tilde{N}_0-\tilde{w}_n\tilde{\delta}^{-1}n_e\tilde{N}_-, \tag{1}$$

$$\mathscr{R}_p=w_p pN_--\omega_p\delta p_eN_0,\quad \tilde{\mathscr{R}}_p=w_p p\tilde{N}_--w_p\tilde{\delta}p_e\tilde{N}_0, \tag{2}$$

where $\tilde{\delta}=\tilde{N}_-^e/\tilde{N}_0^e=\delta\cdot(n_t/\tilde{n})=\delta\cdot(\tilde{p}_t/p_t)$; n_t,p_t and $\tilde{n}_t,\tilde{p}_t$ are the equilibrium carrier concentrations when the energies of the Fermi level $\mathscr{E}_F$ and the corresponding deep level $\mathscr{E}_t$ or $\tilde{\mathscr{E}}_t$ are the same. In the steady-state case, we have

$$\mathscr{R}_n=\mathscr{R}_p,\quad \tilde{\mathscr{R}}_n=\tilde{\mathscr{R}}_p. \tag{3}$$

As in Refs. 2, 3, and 13, we write

$$N=\frac{n_t(1+\delta)}{2\delta^2}\left(4\frac{p_t}{n_t}+2\frac{N_D}{n_t}\delta-\delta^2\right)-\frac{\tilde{\delta}(1+\delta)}{\delta(1+\tilde{\delta})}\tilde{N}. \tag{4}$$

If the concentrations of the carriers and their trapping centers deviate slightly from their equilibrium values, relations (1) and (2) can be linearized with respect to these deviations. Then, using the Poisson equation, as in Refs. 3 and 13, we find that

$$R_n=\frac{\Delta n}{\tau_n}+a_n\,\mathrm{div}(\Delta E),\quad R_p=\frac{\Delta p}{\tau_p}+a_p\,\mathrm{div}(\Delta E), \tag{5}$$

where

$$\frac{1}{\tau_n(\delta)}=\frac{\delta n_t}{2}\left[w_n\left(x_1-\frac{x_2}{\delta}\right)+\tilde{w}_n\left(x_3-\frac{x_4}{\tilde{\delta}}\right)\right]+\frac{w_nN}{1+\delta}+\frac{\tilde{w}_n\tilde{N}}{1+\tilde{\delta}}, \tag{6}$$

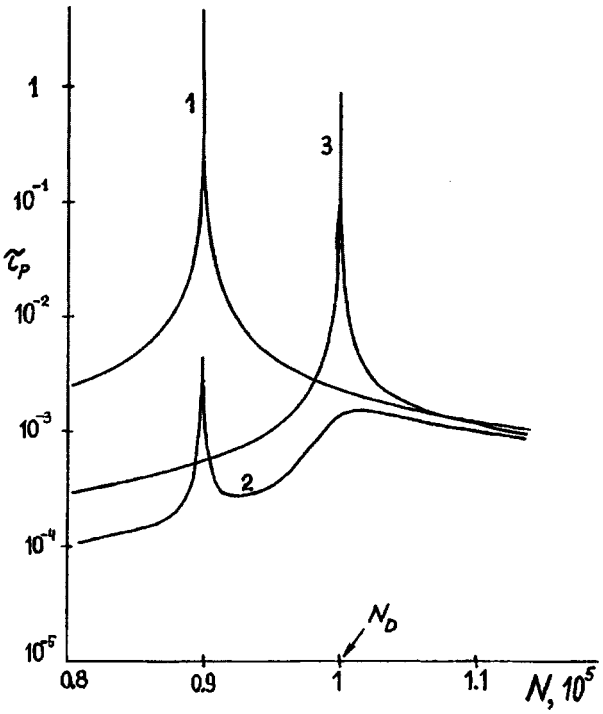

FIG. 1. Hole lifetime τ_p versus concentration N of majority recombination impurity in the presence of an auxiliary acceptor recombination impurity: *1*—$\tilde{n}_t/n_t=10^{-1}$, *2*—$\tilde{n}_t/n_t=10^3$, *3*—$\tilde{n}_t/n_t=10^9$. It is assumed that: $n_t=10^{-4}n_i$, $N_D=10^5 n_i$, the auxiliary impurity concentration is $\tilde{N}=10^{-1}N_D$, $w_p/w_n=10^2$, $w_p=\tilde{w}_p$, and $w_n=\tilde{w}_n$. The lifetime is measured in units of $1/(n_i w_p)$ and N is in units of n_i, where n_i is the intrinsic carrier concentration.

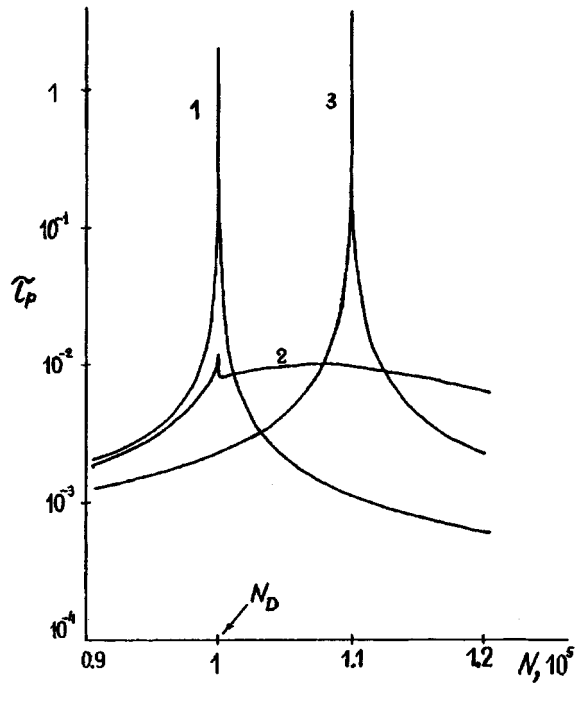

FIG. 2. Hole lifetime τ_p versus of concentration N of majority recombination impurity in the presence of an auxiliary donor recombination impurity which may be in neutral and positive singly charged states. Charged atoms of the auxiliary impurity capture electrons with the probability $\tilde{w}_n$ and thermally generate holes, while neutral atoms capture holes with the probability $\tilde{w}_p$ and thermally generate electrons: *1*—$\tilde{n}_t/n_t=10^{-1}$, *2*—$\tilde{n}_t/n_t=50$, *3*—$\tilde{n}_t/n_t=10^9$. It is assumed that: $n_t=10^{-4}n_i$, $N_D=10^5 n_i$, the auxiliary impurity concentration is $\tilde{N}=10^{-1}N_D$, $w_p/w_n=10^2$, $w_p/\tilde{w}_p=10^2$, and $w_p=\tilde{w}_n$. The lifetime is measured in units of $1/(n_i w_p)$ and N is in units of n_i, where n_i is the intrinsic carrier concentration.

$$\frac{1}{\tau_p(\delta)}=\frac{2p_t}{\delta x_5}[w_p(x_2-\delta x_1)+\tilde{w}_p(x_4-\delta x_3)]+\frac{w_p\delta N}{1+\delta}+\frac{\tilde{w}_p\tilde{\delta}\tilde{N}}{1+\tilde{\delta}}, \tag{7}$$

the dependences of x_1, x_2, x_3, x_4, and x_5 on δ are determined by the system of equations

$$x_1+x_2=x_3+x_4=0, \quad x_5-x_2-x_4=1, \tag{8}$$

$$\left(\frac{w_n n_t}{2}+\frac{2w_p p_t}{\delta}\right)(\delta x_1-x_2)=\frac{N}{1+\delta}(\delta w_p x_5-w_n), \tag{9}$$

$$\left(\frac{\tilde{w}_n\tilde{n}_t}{2}+\frac{2\tilde{w}_p\tilde{p}_t}{\delta}\right)(\delta x_3-x_4)=\frac{\tilde{N}}{1+\tilde{\delta}}(\tilde{\delta}\tilde{w}_p x_5-\tilde{w}_n), \tag{10}$$

$a_n(\delta)$ and $a_p(\delta)$ are certain coefficients, and ΔE is the change in the electric field strength caused by the deviation of n, p, N_0, N_-, $\tilde{N}_0$, and $\tilde{N}_-$ from their equilibrium values. As in Refs. 2, 3, and 13, we use the same terminology for the lifetimes τ_n and τ_p even when quasineutrality is violated.

The curves $\tau_p(N)$ and $\tau_n(N)$ can easily be determined by computer using relations (4) and (6)–(10). We also consider the case of auxiliary deep donor impurities. The curves $\tau_p(N)$ for both cases are plotted in Figs. 1 and 2. It can be seen that the function $\tau_p(N)$ may be highly nonmonotonic even in the presence of auxiliary trapping centers. Unlike the case of a single deep impurity,[1–3] the value of $N=N_{\max}$ at the maximum may differ appreciably from N_D. It is even possible to have two maxima although their value of $\tau_p^{\max}$ is reduced. We shall briefly discuss these results.

The lifetime τ_p increases with increasing N because the concentration of nonequilibrium neutral atoms of the majority deep impurity ΔN_0, which thermally generate holes, increases faster than N_-^e (Refs. 2 and 3). It follows from the physics of the increase in τ_p (Refs. 2 and 3) that at the maximum point we can write

$$N_D+\tilde{N}_+^e(N)=N+\tilde{N}_-^e(N), \tag{11}$$

where $\tilde{N}_+^e$ is the concentration of equilibrium charged atoms of the auxiliary donor impurity. If $\tilde{n}_t/n_t$ is approximately an order of magnitude lower, the condition $\mathscr{E}_F>\tilde{\mathscr{E}}_t$ is always satisfied for $N=N_{\max}$. Thus, in the presence of an auxiliary acceptor impurity (situation ''a'') we have $N_{\max}=N_D-\tilde{N}\equiv N_1$, and for a donor impurity (situation ''d'') we have $N_{\max}=N_D$ (curve *1*). If $\tilde{n}_t$ is very large, then the condition $\mathscr{E}_F<\tilde{\mathscr{E}}_t$ is always satisfied for $N=N_{\max}$. Thus, we have $N_{\max}=N_D$ in situation ''a'' and $N_{\max}=N_D+\tilde{N}\equiv N_2$ in situation ''d'' (curve *3*).

For intermediate values of $\tilde{n}_t$ (curve *2*) we find $\mathscr{E}_F>\tilde{\mathscr{E}}_t$ at the first maximum and $\mathscr{E}_F<\tilde{\mathscr{E}}_t$ at the second. Thus, we

have $N_{\max}^{(1)}=N_1$, $N_{\max}^{(2)}=N_D$ for situation ''a'' and $N_{\max}^{(1)}=N_D$, $N_{\max}^{(2)}=N_2$ for situation ''d.'' The maximum $\tau_p^{\max}$ decreases because a drop in $\mathscr{E}_F$ below $\widetilde{\mathscr{E}}_t$ causes intense capture of nonequilibrium electrons by the auxiliary level, and thus suppresses any increase in the combined (majority plus auxiliary) concentration of nonequilibrium centers responsible for thermal hole generation. This does not occur for very high values of $\widetilde{n}_t$ because of the low probability of thermal hole generation in this case.

A pattern similar to that depicted in Figs. 1 and 2 is also observed for the function $\tau_n(N)$.

The authors are grateful to the Russian Fund for Fundamental Research for supporting this work (Grant No. 96-02-17196).

[1] A. A. Drugova and V. A. Kholodnov, Pis'ma Zh. Tekh. Fiz. **18**(1), 23 (1992) [Tech. Phys. Lett. **18**, 8 (1992)].
[2] A. A. Drugova and V. A. Kholodnov, Solid-State Electron. **38**, 1247 (1995).
[3] V. A. Kholodnov, Fiz. Tekh. Poluprovodn. **30**, 1011 (1996) [Semiconductors **30**, 538 (1996)].
[4] J. S. Blakemore, *Semiconductor Statistics* (Pergamon Press, Oxford, 1962; Mir, Moscow, 1964).
[5] A. G. Milnes, *Deep Impurities in Semiconductors* (Wiley, New York, 1973; Mir, Moscow, 1977).
[6] R. A. Smith, *Semiconductors* (Cambridge University Press, Cambridge, 1959; Mir, Moscow, 1982).
[7] J. S. Blakemore, *Solid State Physics*, 2nd ed. (Cambridge University Press, Cambridge, 1985; Mir, Moscow, 1988).
[8] A. A. Drugova and V. A. Kholodnov, in *Proceedings of the International Symposium on Semiconductor Device Research*, Charlottesville (1995), Vol. 1, pp. 197–200.
[9] V. A. Kholodnov and A. A. Drugova, Pis'ma Zh. Tekh. Fiz. **23**(2), 80 (1997) [Tech. Phys. Lett. **23**, 82 (1997)].
[10] J. Chacham-Diamandy and I. Kidron, Infrared Phys. **21**, 105 (1981).
[11] H. Beneking, IEEE Trans. Electron Devices **ED-29**, 1420 (1982).
[12] A. Rogalski, M. Kimata, V. F. Kocherov, J. Piotrovski, F. F. Sizov, I. I. Taubkin, N. Tubouchi, and N. B. Zalatev, *Infrared Photon Detectors* (SPIE Optical Engineering Press, Bellingham, WA, 1995).
[13] V. A. Kholodnov and N. S. Serebrennikov, Pis'ma Zh. Tekh. Fiz. **23**(7), 39 (1997) [Tech. Phys. Lett. **23**, 268 (1997)].

Translated by R. M. Durham

Evolution of domains and thermal hysteresis effects in the pyrochlore-structure ferroelectric $Cd_2Nb_2O_7$

N. N. Kolpakova, I. L. Shul'pina, L. Shchepan'ska, and P. Piskunovich

A. F. Ioffe Physicotechnical Institute, Russian Academy of Sciences, St. Petersburg;
Institute of Molecular Physics, Polish Academy of Sciences, Poznan, Poland;
A. Mickiewicz University, Poznan, Poland
(Submitted July 1, 1997)
Pis'ma Zh. Tekh. Fiz. **23**, 64–69 (December 26, 1997)

An analysis of the thermally induced domain behavior in $Cd_2Nb_2O_7$ under cooling and heating in the dark has revealed that below T_c the coexistence of ferroelectric-ferroelastic domains of different types is accompanied by irreversible changes in the domains of the previous phase ($T_c<T<T_s$). Interaction of domains with dislocations and other lattice defects causes thermal hysteresis in the phase transition region near T_s and T_c typical of the ''superheated'' ferroic state. © *1997 American Institute of Physics.* [S1063-7850(97)02712-2]

Disordered systems with competing interactions (glasses, relaxors, incommensurately modulated and randomly ordered systems) have recently formed the subject of numerous investigations because of their importance for the development of fundamental ideas on interactions, state evolution, and phase transitions in these systems and their possible applications.[1–4]

Relaxor behavior was recently observed in the pyrochlore-structure compound $Cd_2Nb_2O_7$ ($Fd3m-O_h^7$) (Ref. 5). Unlike the already known perovskite-structure relaxors ($Pm3m-O_h^1$) (Ref. 2), in $Cd_2Nb_2O_7$ the ferroelectric and relaxor states coexist in the ferroelectric phase, the former predominating near T_c and the latter predominating at $T \ll T_c$. Note that below $T_s=205$ K the compound is entirely ferroelastic whereas below $T_c=196$ K it is partly ferroelectric and partly ferroelastic.[6,7] In this system the coexistence of ordered and disordered states and their evolution are directly related to changes in the domain structure. Here we propose to study the thermally induced change in the domain structure in $Cd_2Nb_2O_7$ and the related hysteresis effects in the phase transition region near T_s and T_c.

A regime in which the sample was left ''in the dark'' during cooling and heating was used with $Cd_2Nb_2O_7$ for the first time, in order to study the evolution of the domains in photosensitive materials by optical spectroscopy. The illumination was only switched on at the instant when the domains were photographed (less than 2 s exposure). This regime can reveal the real pattern of the domain behavior with temperature, and can provide an accurate interpretation of data on the electrical, pyroelectric, thermal, and other properties of materials with allowance for the domain structure.

In order to identify the part played by dislocations and other defects in changes in the domain mobility accompanying a phase transition, an analysis was made of the real crystal structure of $(111)_{cub}$ plates by reflection and transmission x-ray diffraction topography using CuK_α and MoK_α radiation at room temperature. It was observed that the samples incorporate numerous microdefects and in some cases, have a thick, severely damaged, surface layer. Naturally faceted plates which have only undergone etching, rather than mechanical treatment, have a thin surface relief, which is regular in some places. When photographed using transmission geometry, the dislocation structure of these thin crystal plates only showed up after the surfaces had been polished mechanically, followed by deep, prolonged (for several hours) chemical etching in an orthophosphoric acid solution to remove any damaged layers. It was established that the crystals have a bulk cellular dislocation structure with an average linear cell size of around 15 μm and a dislocation density of $\sim 10^4$ cm^{-2} or higher.

Figure 1 shows the change in the domain structure in a $(111)_{cub}$ plate during cooling and heating in the dark. The investigations were carried out using the apparatus described in Ref. 7. In this plane, the projections of the domain walls in the $[100]_{cub}$ and $[110]_{cub}$ directions observed below T_s and T_c, respectively,[6,7] lie in the $[112]_{cub}$ directions and are almost indistinguishable. As a result, the static domain pattern in the $(111)_{cub}$ plane is complex and its dynamics have not been analyzed so far.

In the ferroelastic phase ($T_c<T<T_s$), the domain pattern consists of uniformly colored, relatively wide, dark and light bands whose boundary is blurred. In the ferroelectric phase ($T<T_c$), the bands decay into narrower domains in the form of a wedge, which continue to narrow with decreasing temperature and their colors appear in different orders. Some of these domains gradually disappear for $T \to T_{dis} \approx 160$ K, whereas others are observed optically up to $T_{inc}=85$ K. Domains of the first type are not observed optically when the sample is heated to T_s either in the dark or under illumination. Domains of the second type gradually become broader as the sample is heated to T_c in the dark, and disappear at temperatures several degrees above T_c. This pattern of domain behavior is repeated at thermal scanning rates of 1 K·min^{-1}, 5 K·min^{-1}, and 15 K·min^{-1} if the cooling and heating cycle begins at $T \geqslant (T_s+\Delta T)$, where $\Delta T \approx 20$ K, and the sample is held at this temperature for approximately an hour. The domain behavior during heating does not depend on whether the sample is cooled to $T<T_{inc}$ or $T>T_{inc}$. If the rate of thermal scanning is increased to 15 K·min^{-1}, domains of the first type disappear at temperatures considerably higher than 160 K whereas domains of the second type remain broader over the entire temperature range

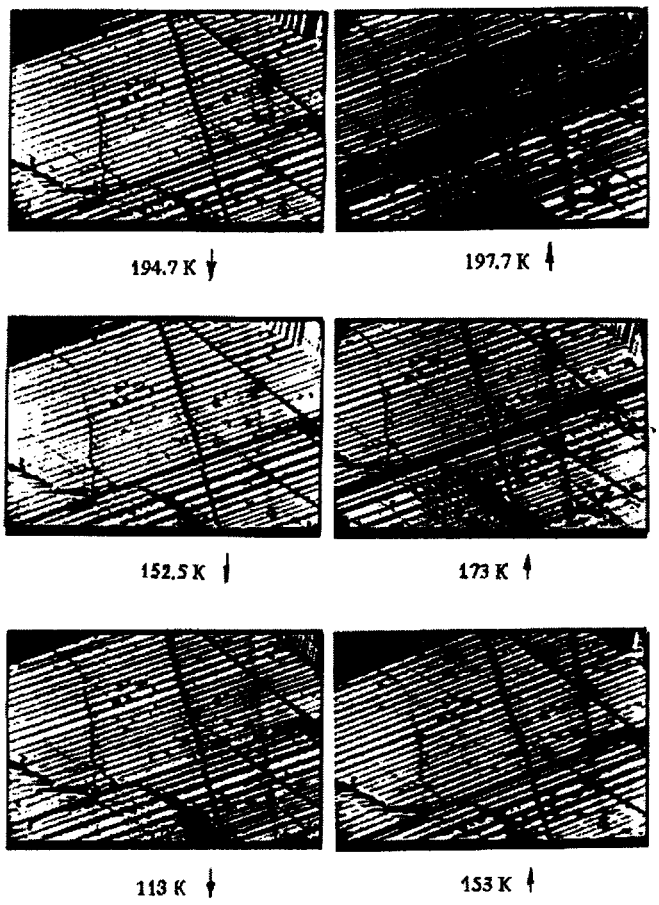

FIG. 1. Thermally induced evolution of domains in the dark during cooling and heating of the sample at a rate of $5\,\mathrm{K}\cdot\mathrm{min}^{-1}$. The thickness of the $(111)_{\mathrm{cub}}$ plate is less than 0.8 mm.

up to T_{inc}. As the sample is heated, the thermal hysteresis effect increases near T_s and T_c. When the sample is repeatedly cooled at a rate of $15\,\mathrm{K}\cdot\mathrm{min}^{-1}$ (or with decreasing ΔT), a ''memory'' effect for the previous state is observed near T_s and T_c. The change in the domain pattern in the phase transition region and in the ferroelectric phase implies that at least two slowly evolving processes in real time take place in the system. These processes are associated, on the one hand, with anchoring of domain walls at impurities and lattice defects and on the other hand, are caused by the specific characteristics of the state and the internal properties of the system.

This conclusion is also supported by the results of calorimetric measurements (Fig. 2). As the sample is cooled, a broad λ-type anomaly corresponding to two phase transitions is observed at $T_s = 205$ K and disappears at $T \approx T_{\mathrm{dis}}$. As the sample is heated, the DTA anomaly is shifted toward higher temperatures and disappears at temperatures 3–5 K above T_s, which may provide indirect evidence of the existence of optically unobservable domains of the first type. Thermal hysteresis of the DTA curves is not typical of a first-order phase transition and more likely corresponds to the superheated ferroic state. The area bounded by the heating curve is approximately 10% smaller than the area below the cooling curve, which indicates a difference between the thermal energy of the exothermic and endothermic processes. For the

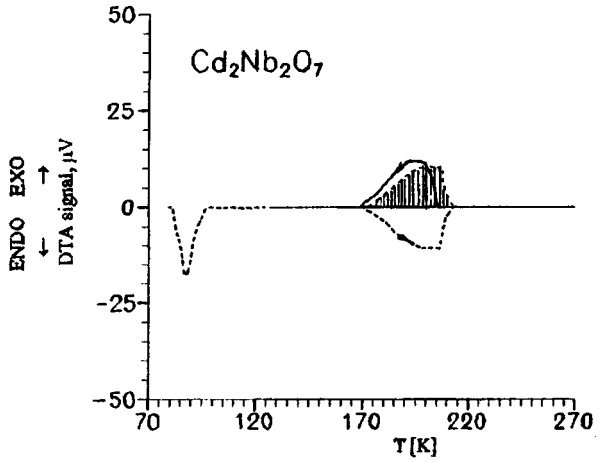

FIG. 2. Differential thermal analysis (DTA) of the excess specific heat of the lattice in the phase transition region during cooling and heating at a rate of $5\,\mathrm{K}\cdot\mathrm{min}^{-1}$. The shaded area corresponds to a mirror image of the heating curve and illustrates the existence of thermal hysteresis and the difference between the thermal energy of the exothermic and endothermic process.

exothermic process, the change in the total enthalpy and the total entropy of the two phase transitions is $\Delta H = (199 \pm 26)\,\mathrm{J}\cdot\mathrm{mol}^{-1}$ and $\Delta S = (0.995 \pm 0.13)\,\mathrm{J}\cdot\mathrm{mol}^{-1}\cdot\mathrm{K}^{-1}$, respectively. The decrease in the thermal energy of the exothermic process is clearly caused by an irreversible change in the domains of the first type.

Note that the sizes of the domains of the second type (around 50–70 μm at 120 K) are comparable with the size of the dislocation cells, whereas at $T < T_{\mathrm{dis}}$ the domains of the first type may even be appreciably smaller. Interactions between the two types of domains and the dislocation superlattice may be responsible for the reduced mobility of the domains under heating and may cause a thermal hysteresis effect in the phase transition region typical of the ''superheated'' state.

The coexistence of two types of domains in the ferroelectric phase, capable of being switched by an external electric field[6] and by uniaxial pressure,[7] indicates that below T_c not only do ferroelectric-ferroelastic domains of the second type appear but also the ferroelastic domains of the preceding phase (domains of the first type) become ferroelectric-ferroelastic.

The evolution of the different domains and also the tendency of the pyrochlore lattice toward a gradual reduction in symmetry as a result of structural phase transitions (i.e., $m3m \rightarrow mmm(ss) \rightarrow mm2(pp)$ instead of $m3m \rightarrow mm2(pp)$) (Ref. 6) support the assumption that the structural instability of the $Cd_2Nb_2O_7$ pyrochlore lattice with decreasing temperature is caused by instability of the $(CdO_8)^{n-}$ sublattice.[5,8] Dynamic disorder in the localization of the Cd ions as a result of off-center displacements[8] is responsible for the structural instability of the $(CdO_8)^{n-}$ sublattice which also provokes instability of the rigid $(NbO_6)^{n-}$ sublattice, i.e., functions as a trigger mechanism for the phase transition sequence in the system.

This work was partly supported financially by the Russian Fund for Fundamental Research (Project No. 97-02-18099).

[1] U. T. Höchli, K. Knorr, and A. Loidi, Adv. Phys. **39**, 405 (1990).
[2] L. Cross, Ferroelectrics **76**, 241 (1987); F. Chu, L. M. Reaney, and N. Setter, J. Appl. Phys. **77**, 1671 (1995).
[3] T. Janssen and J. A. Tjon, J. Phys. C: Solid State Phys. **16**, 4789 (1983).
[4] V. Westphal, W. Kleemann, and M. D. Glinchuk, Phys. Rev. Lett. **68**, 847 (1992).
[5] N. N. Kolpakova, M. Wiesner, G. Kugel, and P. Bourson, Ferroelectrics **190**, 179 (1997).
[6] Z. G. Ye, N. N. Kolpakova, J. P. Rivera, and H. Schmid, Ferroelectrics **124**, 275 (1991).
[7] N. N. Kolpakova, R. Margraf, and A. Petrashenko, Fiz. Tverd. Tela **29**, 2638 (1987) [Sov. Phys. Solid State **29**, 1520 (1987)].
[8] K. Lukaszewicz, A. Pietraszko, J. Stepien-Damm, and N. N. Kolpakova, Mater. Res. Bull. **29**, 987 (1994).

Translated by R. M. Durham

Method of determining the single-domain property of magnetic powder particles

Sh. M. Aliev, I. K. Kamilov, and K. M. Aliev

Kh. I. Amirkhanov Institute of Physics, Dagestan Scientific Center, Russian Academy of Sciences, Makhachkala

(Submitted July 25, 1996; resubmitted April 25, 1997)
Pis'ma Zh. Tekh. Fiz. **23**, 70–73 (December 26, 1997)

A method of determining the single-domain property of magnetic powder particles based on Mössbauer spectroscopy is proposed and checked experimentally. © *1997 American Institute of Physics.* [S1063-7850(97)02812-7]

It is known that single-domain particles are formed when a magnetic substance is vigorously ground. The physical reason for this effect is that, as the size of a particle is reduced, its magnetostatic energy, which is proportional to its volume, decreases faster than the energy of the domain walls, which is proportional to the surface area of the particle. For a certain critical size, the single-domain state becomes energetically favorable. The critical diameter at which the particle is converted from the multidomain to the single-domain state is determined from the expression:[1]

$$d_{\mathrm{cd}}=\frac{9}{4\pi}\frac{\sigma}{M_s^2}, \tag{1}$$

where σ is the energy density of the domain wall and M_s is the spontaneous magnetization of the particle. Magnetic powders formed of single-domain particles have found extensive technical applications, having been used to fabricate permanent magnets, magnetic tape for video and audio recording, diskettes and other information media for computing technology.

Here we propose a method of determining the single-domain state of magnetic powder particles based on Mössbauer spectroscopy.

We consider an ensemble of single-domain particles distributed isotropically in space. If this ensemble of particles is magnetized to saturation and the magnetizing field H is then switched off, the maximum angle θ_m of deflection of the particle magnetization vectors relative to the direction of the applied field will be equal to the angle α between the difficult and easy magnetization axes in this magnetic substance. For magnetic substances with cubic anisotropy we have $\alpha=55°$ and for those with uniaxial anisotropy $\alpha=90°$. Thus, in the residual magnetization state, the magnetization vectors of single-domain particles are isotropically distributed in the solid angle $\Omega=2\theta_m=2\alpha$. If a domain structure exists in the particles, then $\theta_m>\alpha$ since, apart from domains whose magnetization vectors are directed along the easy magnetization axes, the domain structure also contains domains of closure and domain walls in which the magnetic moments of the atoms are directed at an angle to the easy magnetization axes.

Let us assume that the experimental geometry is such that the direction of propagation of the γ-quanta coincides with the H direction. Then, S which is the ratio of the second to the first or the fifth to the sixth lines in the Mössbauer spectrum of the ^{57}Fe nuclei in the sample, can be written as:[2]

$$S=\frac{4(1-\overline{\cos^2\theta_i})}{3(1+\overline{\cos^2\theta_i})}, \tag{2}$$

where θ_i is the angle between the direction of propagation of the γ-quanta and the direction of magnetization of the ith particle $(0\leqslant\theta_i\leqslant\theta_m)$:

$$\overline{\cos^2\theta_i}=\frac{\int_0^{\theta_m}\int_0^{2\pi}\cos^2\theta\sin\theta\,d\theta\,d\varphi}{\int_0^{\theta_m}\int_0^{2\pi}\sin\theta\,d\theta\,d\varphi}=\frac{\cos^3\theta_m-1}{3(\cos\theta_m-1)}. \tag{3}$$

For single-domain particles we obtain: $\overline{\cos^2\theta_i}=0.63$ (cubic anisotropy) and $\overline{\cos^2\theta_i}=0.33$ (uniaxial anisotropy). Substituting these values into formula (2), we obtain the following

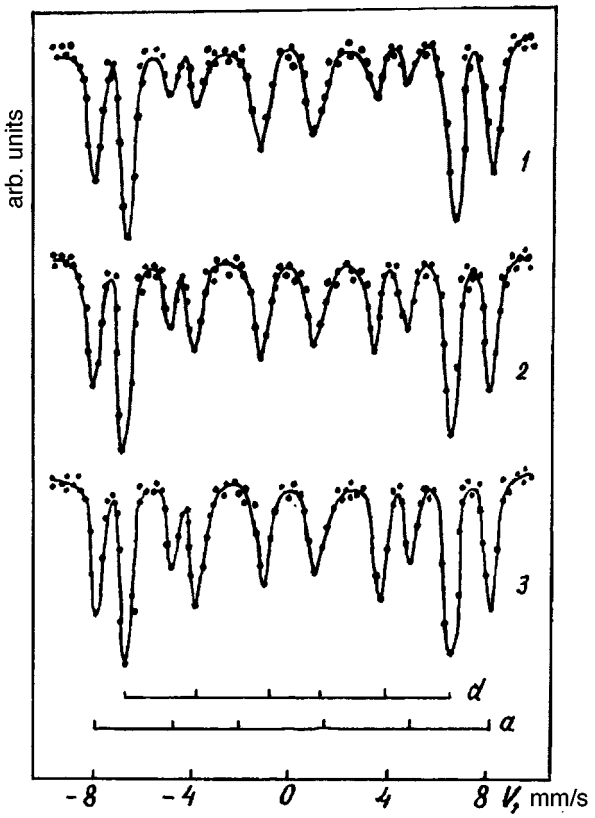

FIG. 1. Mössbauer spectra of a sample of single-crystal ferrite $Gd_3Fe_5O_{12}$ particles ($d=20$ μm). The sample was converted to a state of residual magnetization perpendicular to the plane of the sample for: *1*—$T=T_{\mathrm{com}}+1$ K, *2*—$T=T_{\mathrm{com}}+33$ K, and *3*—$T=T_{\mathrm{com}}+45$ K.

criteria: if $S+\Delta S \leqslant 0.30$ (cubic anisotropy) or $S+\Delta S \leqslant 0.67$ (uniaxial isotropy), the powder particles will be single-domain: ΔS is the experimental error in determining the parameter S.

If $S-\Delta S > 0.30$ (cubic anisotropy) or $S-\Delta S > 0.67$ (uniaxial anisotropy), the powder particles will have a domain structure and the relative number of domains in the particles can be assessed from the value of S.

The most favorable magnetic substances from the experimental point of view are ferrites having a compensation point T_{com}. In fact, as a result of their low spontaneous magnetization, even fairly large ferrite particles may become single-domain near T_{com} (Ref. 3). In addition, particles which are single-domain near T_{com} are converted to multidomain with increasing departure from T_{com}. Thus, the validity of the criteria may be checked experimentally by gradually moving away from T_{com}.

The method was checked for crystals of the single-crystal ferrite $Gd_3Fe_5O_{12}$ ($T_{com}=286$ K) which possesses cubic anisotropy. By passing the powder through a set of fine sieves, we obtain ferrite particles of approximately uniform diameter $d=20$ μm. A standard technique was used to prepare a sample from the powder. The sample was converted to a state of residual magnetization in a field $H=5$ kOe applied perpendicular to the plane of the sample. Typical spectra obtained near T_{com} are shown in Fig. 1. The spectra consist of two superposed Zeeman sextets attributed to iron ions in the a and d ferrite sublattices. The following data were obtained for S: for $T=T_{com}+1$ K, $S=0.26\pm0.04$, for $T=T_{com}+33$ K, $S=0.45\pm0.04$, and for $T=T_{com}+45$ K, $S=0.64\pm0.04$. It can be seen that near T_{com} the ferrite particles are single-domain.

With increasing departure from T_{com}, the particles are converted to the multidomain state and the number of domains in the particles increases. In the domain structure the domains occupy a considerably larger volume than the domain walls so that the increase in the parameter S with distance from T_{com} is mainly caused by an increase in the number of domains of closure magnetized at an angle to the easy magnetization axes.

It should be noted that near T_{com}, ferrite particles are weakly magnetic so that during the particle preparation process at room temperature the particles did not attract each other and the isotropy of the sample was automatically ensured. In practice, strongly magnetic materials are more frequently used, in which the single-domain particles may attract each other like elementary magnets, forming chains and clumps which may impair the isotropy of the sample on which the proposed method is based. Thus, it is better to prepare the samples at temperatures above the Curie temperature T_c by selecting a binder which hardens near T_c.

[1] S. Krupichka, *Physics of Ferrites and Their Related Magnetic Oxides*, Vol. 2 [in Russian], Mir, Moscow (1976).
[2] S. M. Irkaev, R. N. Kuz'min, and A. A. Opalenko, *Nuclear Gamma Resonance* [in Russian], Moscow State University Press, Moscow (1970).
[3] V. G. Bar'yakhtar and D. A. Yablonskiĭ, Fiz. Tverd. Tela (Leningrad) **16**, 3511 (1974) [Sov. Phys. Solid State **16**, 2282 (1974)].

Translated by R. M. Durham

Introduction of color centers in fluorinated sol gel quartz glasses by radiation thermal treatment

S. S. Vetokhin, E. S. Voropaĭ, G. A. Lisovskiĭ, I. M. Mel'nichenko, B. V. Plyushch, E. N. Poddenezhnyĭ, and V. A. Saechnikov

Scientific-Research Institute of Applied Physics Problems, Belarus State University
(Submitted May 8, 1997)
Pis'ma Zh. Tekh. Fiz. **23**, 74–79 (December 26, 1997)

Data are presented to show how fluorination influences the optical quality and radiation resistance of quartz glasses fabricated by the sol gel method. It is found that under the action of gamma radiation, mainly E' centers form in the glasses. The incorporation of fluorine in the xerogel lattice promotes the removal of hydroxyl groups and enhances the radiation optical resistance of the synthesized samples in the red. It is observed that the radiation resistance of the glass is enhanced in the ultraviolet by using irradiation-annealing cycles and this is attributed to a decrease in the concentration of radiation-induced E' centers. © *1997 American Institute of Physics.* [S1063-7850(97)02912-1]

The solution of problems involved in using glassy silicon dioxide, which forms of the basis of fiber-optic waveguides, in ionizing radiation fields is closely related to studies of the mechanisms responsible for the formation of radiation-induced color centers, and is aimed at developing a technology to produce glasses possessing enhanced radiation optical stability.[1,2] Here we propose to examine the efficiency of a technological procedure involving the fluorination of quartz glasses fabricated by a sol gel method, in terms of their radiation resistance.

The samples were prepared by a sol gel technique, developed by the authors, using tetraethylorthosilicate $Si(OC_2H_5)_4$ as the initial component.[3] The xerogel obtained after drying at 60 °C was placed in a horizontal furnace in a pure quartz glass reactor, where fluorination was carried by holding the blanks at 1000 °C in a mixture of fluorine-containing gases prepared by dissociation of freon ($C_2Cl_3F_3$) in an oxygen atmosphere (samples in series 1). Samples in series 2 were not fluorinated. Both types of blanks were sintered as far as the optical glass state in a helium atmosphere at temperatures of 1200–1300 °C. Results of an x-ray microanalysis gave the fluorine content in the series 1 glasses as 0.45–0.5 wt.%.

The samples were exposed to primary irradiation by ^{60}Co gamma quanta, then annealed at 1000 °C, and exposed to further irradiation. The dose rate was 280 Gy/s. The absorption spectra of the samples were recorded using SPEKORD UV VIS, SPEKORD M-40, and SOLAR P-1256 absorption spectrometers. The luminescence spectra were measured with a FLUOROLOG-SPEX spectrofluorimeter using a xenon lamp as the excitation source and recording perpendicular to the direction of excitation. The ESR spectra were recorded using a Varian spectrometer.

After gamma irradiation, the ESR spectra of the samples reveal a signal with $g=2.0013$, known in the glass network to be an E' center, which corresponds to a band with a maximum at 212 nm in the optical absorption spectra. In addition, at a dose of 5×10^3 Gy series 2 samples began to reveal a weak absorption band near 580 nm. With increasing irradiation, the peak of this band underwent a long-

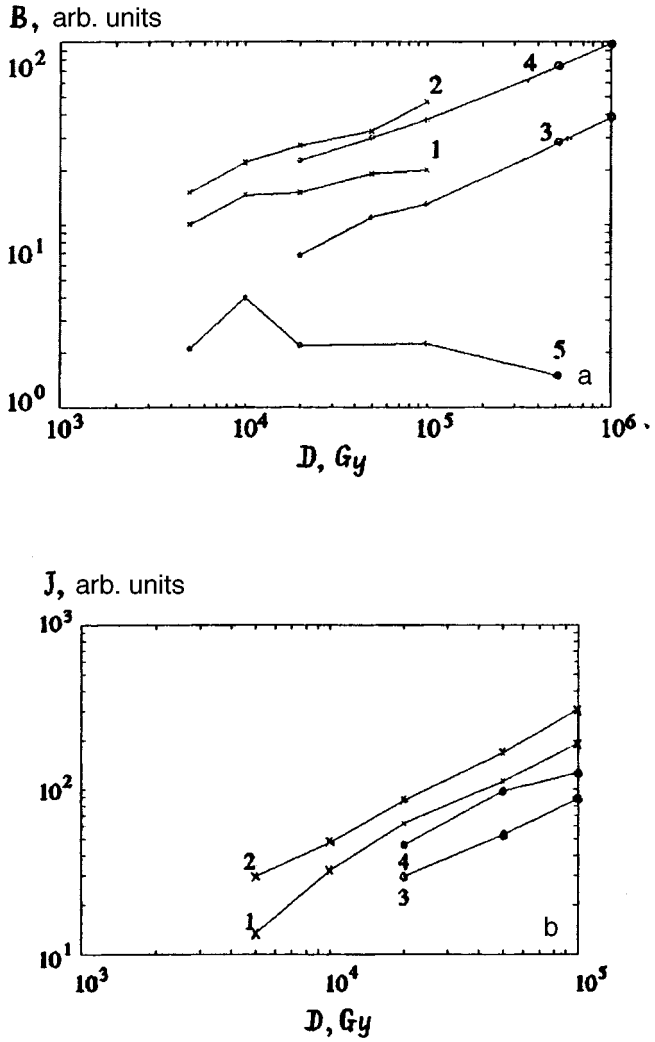

FIG. 1. Optical absorption intensity in the 212 nm band (a) and ESR signal intensity of E' centers (b) as a function of dose: *1, 3*—series 1 samples, *2, 4*—series 2 samples; *1, 2*—first irradiation, *3, 4*—repeated irradiation after thermal annealing at 1000 °C; *5*—optical absorption intensity of nonbridging oxygen atoms for series 2 glasses.

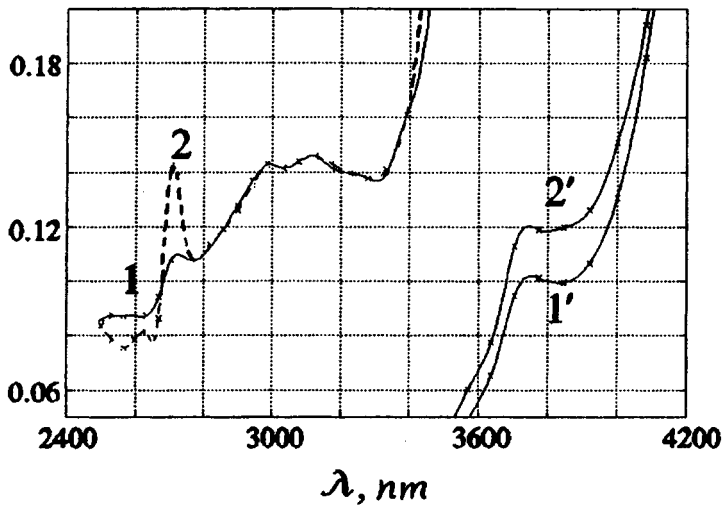

FIG. 2. Optical density of samples D (*1*, *2*) and $D/8$ (*1′*, *2′*) for series 1 samples (*1*, *1′*) and series 2 samples (*2*, *2′*).

wavelength shift to 620 nm and this was accompanied by a synchronous increase in its intensity (Fig. 1, curve *5*). As the dose increased further, the peak reverted to its initial position 580 nm and the band intensity fell accordingly. The photoluminescence spectra revealed a 1.9 eV band attributed to absorption by nonbridging oxygen atoms.[4]

In the literature, the shift of the absorption peaks is attributed to the formation of a hydrogen bond between hydrogen belonging to a hydroxyl group and a neighboring nonbridging oxygen atom. A high concentration of $\equiv$Si–OH complexes is required to create conditions for the formation of hydrogen bonds, and the corresponding effects may be observed in quartz glasses with a high concentration of structurally bound hydrogen. The authors of Ref. 6 examined the optical characteristics of two types of nonbridging oxygen atom which give the same 1.9 eV red luminescence band, but in a different spectral range of photoexcitation: a nonbridging oxygen atom with a hydrogen bond and a $\equiv SiO^-$ complex, formed by radiolytic breaking of peroxide bridges (H1 center). The shift of the optical absorption peak near 2 eV is a result of the action of the absorption bands of each of these nonbridging oxygen atoms.

These results on the shift of the optical absorption band in the range 580–620 nm may be interpreted by analogy with Ref. 6. The gel fluorination stage was omitted for the series 2 samples and these therefore contained structurally bound hydrogen in the form of a fairly high concentration of $\equiv$Si–OH groups, as is evidenced by the infrared absorption spectra in the 2700 nm band, caused by the stretching vibrations of these groups. Thus, the nonbridging oxygen atoms generated at the initial stage of irradiation are caused by a hydrogen bond with neighboring hydroxyl groups, which is responsible for the 580 nm band. Since the precursors of nonbridging oxygen atoms are $\equiv$Si–OH fragments, an increase in the number of nonbridging oxygen atoms with increasing irradiation dose is accompanied by a decrease in the concentration of OH groups and this leads to weakening of the hydrogen bonds. Nonbridging oxygen without a hydrogen bond forms the 620 nm band. Thus, the shift of the absorption peak to 620 nm is an effect caused by the superposition of the 580 and 620 nm bands whose intensity varies in opposite directions under irradiation. The reverse shift of the absorption band back to 580 nm with increasing irradiation is caused by the reappearance of hydroxyl groups and strengthening of hydrogen bonds (the concentration of nonbridging oxygen atoms is then reduced).

The 212 nm band (E' center) predominated in the ultraviolet part of the spectrum, its intensity being an order of magnitude higher than that of the band assigned to the nonbridging oxygen. Figure 1 (curves *1* and *2*) shows the kinetics of the buildup of E' centers from the results of the optical and ESR measurements. In the dose range 5×10^3–10^6 Gy the corresponding curves are power functions. Figure 2 shows the infrared absorption spectra. A comparison between the intensity of the stretching vibration bands of the $\equiv$Si–OH complexes at 2700 nm for both batches of samples indicates that the series 2 samples contain a considerable quantity of structurally bound water which reduces their radiation resistance compared with the series 1 glasses (Fig. 1, curves *1* and *2*). In addition a 3740 nm (2673^{-1} cm) vibrational band can be detected in the infrared spectrum which corresponds to the vibration frequency of a diatomic molecule such as $H^{35}Cl^+$ (Ref. 7). These molecules may well be present in these glasses, distributed in structural cavities in the glass network, since the source of chlorine may be a technological process involving the hydrolysis of tetraethylorthosilicate and the source of hydrogen may be radiation-excited silanol and hydroxyl groups.

It is known[8,9] that fluorine, as an electrophilic agent, attacks the Si–OR bond and thereby accelerates the hydrolysis of alkoxyl compounds, catalyzes the polymerization reaction, and promotes the removal of hydroxyl from the gel. However, as the temperature rises, the volatile compounds HF and SiF_4, formed in intermediate reactions, reduce the fluorine content in the gels, and the number of OH groups is therefore reduced less efficiently.[8] In the present case, the gel was fluorinated at 1000 °C at the stage preceding sintering (series 1 samples) which appreciably reduced the intensity of the vibrational band associated with the presence of hydroxyl groups and improved the radiation resistance of the glasses in the red (no nonbridging oxygen atom band was observed).

These results indicate that fluorine clearly interacts pre-

dominantly with ≡Si–OH groups, while the ≡Si–H complexes are mainly unaffected and act as precursors for the E' centers produced as a result of radiation damage to the corresponding valence bonds with the formation of triply-coordinated silicon atoms and mobile hydrogen. No reappearance of the ≡Si–H bond is observed since the hydrogen possibly stabilizes in the glass network where it combines with the process fluorine. Repeated irradiation of the samples, which was carried out after exposure to a dose of 10^5 Gy and thermal annealing at 1000 °C for 1.5 h almost doubled the radiation resistance for the E' center (Fig. 1, curves *3* and *4*), which may be explained by breaking of stressed ≡Si–O–Si≡ bonds followed by their high-temperature reappearance during topological reconstruction of the glass network. This observation may be used as the basis for enhancing the radiation optical resistance of glasses, by using radiation thermal treatment as an additional process factor.

[1] S. M. Brekhovskikh and V. A. Tyul'nin, *Radiation Centers in Inorganic Glasses* [in Russian], Énergoatomizdat, Moscow (1988).
[2] V. I. Arbuzov, Fiz. Khim. Stekla **19**, 410 (1993).
[3] E. N. Poddenezny, I. M. Melnichenko, B. V. Plyush *et al.*, J. Advanced Mater. **2**, 382 (1995).
[4] A. R. Silin', L. N. Skuya, and A. V. Shendrik, Fiz. Khim. Stekla **4**, 405 (1978).
[5] A. G. Revesz, J. Electrochem. Soc. **126**, 122 (1979).
[6] S. Munekuni, T. Yamanaka, Y. Shimogaichi *et al.*, J. Appl. Phys. **68**, 1212 (1990).
[7] *Molecular Constants of Inorganic Compounds*, edited by K. S. Krasnov [in Russian], Khimiya, Leningrad (1979).
[8] G. Sijian and G. Zhenan, in *Proceedings of the 16th International Congress on Glass, Madrid, Spain, 1992*, Vol. 7, pp. 39–42.
[9] R. Winter, J. B. Chan, J. B. Frattini, and J. Jonas, J. Non-Cryst. Solids **105**, 214 (1988).

Translated by R. M. Durham

Multiple formation of microcracks during mechanical loading of polymers

S. O. Gladkov and V. G. Nikol'skiĭ

N. N. Semenov Institute of Chemical Physics, Russian Academy of Sciences, Moscow
(Submitted April 9, 1997)
Pis'ma Zh. Tekh. Fiz. **23**, 80–85 (December 26, 1997)

General kinetic and thermodynamic reasoning is used to propose a new mechanism for multiple crack formation caused by a mechanical action on a polymer. It is shown that the role of information ''carrier'' to ''weak'' (in terms of thermodynamic stability) spots localized in the polymer matrix is assigned to phonons as a unique class of quasiparticles which exist in nonconducting and nonmagnetic dielectrics.
[S1063-7850(97)03012-7]

Studies of cracking mechanisms in polymer structures undergoing mechanical damage in mills, dispersers, and crushers have recently attracted growing interest, mainly because of the broad spectrum of applications of finely dispersed structures in engineering and industry. It is known that existing powder technology has reached a level where any surface coating of any degrees of complexity can now be fabricated. This has given rise to numerous problems of a purely physical nature, which include studying the physical nature of the mechanism of microcrack formation in a polymer undergoing mechanical damage. We shall discuss a new approach.

Let us consider a polymer subjected to shear strain. It is known[1] that when a material is exposed to an external mechanical action, an elastic strain wave appears, propagating through the material at the characteristic velocity of sound for the material. Since polymers are, in most respects, isotropic structures (in a polymer as such, there are no symmetric transformations typical of a purely crystalline structure), we can assume that sound propagates in a polymer at the single velocity c_s. It should be noted also that, since a polymer consists of randomly distributed crystallites and amorphous components, and each crystallite has its own axis of anisotropy **n**, the total free energy of the structure within the entire polymer matrix must clearly be averaged over all orientations **n**. As a result, a purely isotropic free energy will be obtained, whose expression only contains combinations of derivatives $(\partial u_i/\partial x_i)^2$, where **u** is the displacement vector of the medium, and $i=1,2,3$. Let us assume that the crystallites have the dimensions R. In practice, two cases are found: a) $\lambda \gg R$ and b) $\lambda \ll R$, where λ is the wavelength of sound. Both cases may be taken into account in the same manner, by introducing a functional dependence of the velocity of sound on the degree of crystallinity ξ of the polymer. Suppose that $c_s = c_s(\xi)$, and the phonon dispersion is, as usual,[1] $\omega_k = c_s(\xi)k$, where k is the wave vector. It was shown in Ref. 2 that when an atom in a specific energy state with the energy ε absorbs n phonons, the atom is excited and transferred to the level ε^*. This process may be arbitrarily called a preparatory process preparing the atom for active chemical interaction. Since a polymer always contains some radicals, foreign chemically active atoms, inhomogeneous defects exhibiting high chemical activity, and other similar ''elements'', there is always a certain probability of finding an excited atom prepared (having absorbed n photons) for a chemical bond with these elements. As we know, the most efficient chemical reaction takes place at the surface of a solid structure. This implies that when the polymer matrix contains foreign macroscopic defects, the probability of a chemical interaction of the atoms in the main structure is fairly high and their contact is therefore a *fait accomplis*. However, since the defect concentration is usually low, this chemical contact will be less likely than the multiple ''repulsion'' of atoms. We shall examine this aspect in detail.

Since temperatures close to the polymer melting point T_{mp} are being studied, the Vogel-Fulcher law, established empirically at the beginning of the twentieth century, begins to apply under these conditions.[1,2] This law basically states that all dynamic parameters characterizing a given substance begin to depend strongly on the degree of approximation to the melting point. In fact, these experiments indicate that the viscosity becomes a function of the temperature difference: $\eta = \eta_0 \exp\{-\Delta/(T_{mp}-T)\} + \eta_p$, where η_0 is the polymer viscosity at $T = T_{mp}$. Physically, this is quite understandable: as the percolation point is approached[3] $\langle T = T_{mp} \rangle$, exchange interaction between molecules of the main polymer structure is suppressed and another additional geometric parameter appears—the correlation length, which increases rapidly as the melting point is approached (as a result of the stochasticity of the exchange interaction). Formally, this gives us the right to talk of bond weakening, and thus of increasing distance between the interacting molecules, which then justifies the introduction of viscosity and consequently, of the molecular mean free path.

Let us consider the following model scenario. Suppose that at zero time when no mechanical load is applied, the polymer matrix has a certain equilibrium entropy S_0. Since the polymer consists of crystalline and amorphous components (here we are obviously talking of temperatures above the glass-transition temperature T_g), we can write $S_0 = \xi S_{01} + (1-\xi)S_{02}$, where ξ is the degree of crystallinity (the ratio of the number of crystallite molecules to the total number of polymer molecules), S_{01} and S_{02} are the entropies of the crystalline and amorphous regions, respectively. Then suppose that as a result of deformation, the surface of the polymer is displaced by δx. This displacement leads to a change in entropy which we denote by δS. Then, according

to the first law of thermodynamics (neglecting the losses in the external medium), we have

$$\mathbf{F}\delta\mathbf{x} = \delta E - T\delta S, \tag{1}$$

where **F** is the shear strain force (in other words, the external force) and δE is the change in the internal energy of the polymer.

Since the external action comprises shear strain, the first problem which forms the essence of this study, involves determining the relation between the entropy and the strain tensor u_{ik}, which is some temporally periodic wave propagating ahead of the shear strain front.

There is a high probability that prepared chemically active particles may undergo a chemical reaction with other active elements. This reaction only takes place if the process is energetically favorable and this therefore gives rise to the quite specific thermodynamic problem of estimating which of two mechanisms of interaction between a pair of active elements is more favorable, either:

a) interacting, having formed a bound structure, or
b) repelling each other, having broken the bond.

We shall only discuss a pair of interacting conglomerates (the number of atoms or molecules contained in its structure is completely unimportant), as this can obviously be generalized to an arbitrary number of conglomerates.

A mechanical shear strain generates a sound wave propagating through the material at the characteristic velocity of sound. It should be said that because of the macroscopic nature of the mechanical action, there will be a sufficient number of these waves for us to talk of a multiple process. We stress that these advance waves are characteristic not only of crystalline structures but also of amorphous, fiber, and other extremely complex dense structures. Drawing a parallel between these waves and phonons, we consider the possible repulsion of structure conglomerates (particles for short) excited by the absorption of n phonons.

We assume that the central spacing between particles in the excited state ε^* is r_0. We arbitrarily call particle 1 left and particle 2 right. If y is the displacement of the left particle toward the right and $r_0 - x - y$ is the displacement of the right particle toward the left, where x is the distance between the particles after displacement, the total energy of this system is $E = 0.5m(\omega^*)^2y^2 + 0.5m(\omega^*)^2(r_0 - x - y)^2 + \alpha/x^n$, where ω^* is the oscillation frequency of the excited particle. Differentiating the function $E\{x,y\}$ first with respect to x and then with respect to y and equating the derivatives to zero, we find that the condition of minimum E gives: $y = 0.5(r_0 - x)$, and x satisfies the equation $x - 2\alpha n/m(\omega^*)^2x^{n+1} = r_0$. The solution of this equation is only physically meaningful for $x > r_0$. This implies that breaking of the bond and separation by a certain large (compared with the interatomic spacing) but finite distance $x > r_0$ is energetically favorable. Note that the frequency ω^* is proportional to the energy of an excited particle which has absorbed n acoustic quanta. It was shown in Ref. 2 that the corresponding probability is highest at comparatively high (say room) temperatures. Thus, at those energetically weak points where there is a local tendency to microseparation, a microcrack begins to form, its size x increasing as the external strain wave advances. Physically, this process is quite understandable and only requires one factor, allowance for the probability of an n-particle absorption process.

In order to allow for this process, we must bear in mind that the frequency of an excited atom is $\omega^* = \omega + \nu W$, where ω is the frequency of the zero-point oscillations, ν is some characteristic frequency, and W is the probability of phonon absorption. This probability was calculated in Ref. 2. In principle, this approach to explain the process of polymer damage is fairly general and may also be applied to other types of structures. The role of the exciting mechanism will be particular to each specific case: for dielectrics it will be phonons, for magnetic substances it can either be phonons or magnons (competition between these two mechanisms is determined by the temperature ranges for which the investigation is made), and for metals it will be electrons.

Since an enormous number of phonons appear as the strain wave propagates, their interaction with numerous atoms and the transitions of these atoms forming the conglomerate to the excited state ε^* is also a multiple process. However, since near each excited particle there may be at least one other excited particle, ultimately it is energetically favorable for these to separate, as has been shown above but, since there are many of these pairs, there will also be many incipient microcracks.

It should be noted that this theory of multiple microcrack generation using a many-phonon mechanism has a completely realistic physical basis which does not contradict known theoretical hypotheses.[4–9]

This work was partially supported by the Russian Fund for Fundamental Research, Grant No. RFFI-96-03-03237.

[1] V. L. Gurevich, *Kinetics of Phonon Systems* [in Russian], Nauka, Moscow (1980).
[2] S. O. Gladkov, Phys. Lett. A **148**, 253 (1990).
[3] B. L. Shklovskiĭ and A. E. Efros, *Percolation Theory* [in Russian], Nauka, Moscow (1982).
[4] S. O. Gladkov, Chem. Phys. Lett. **174**, 636 (1990).
[5] S. N. Zhurkov, Vestn. Akad. Nauk SSSR No. 3, 46 (1968).
[6] S. N. Zhurkov, V. S. Kuksenko, and A. I. Slutsker, Fiz. Tverd. Tela (Leningrad), **11**, 297 (1969) [*sic*].
[7] Yu. Ya. Gotlib, A. V. Dobroumov, A. M. El'yashevich, and Yu. E. Svetlov, Fiz. Tverd. Tela (Leningrad) **15**, 801 (1973) [Sov. Phys. Solid State **15**, 555 (1973)].
[8] G. M. Bartenev, *Strength and Damage Mechanism of Polymers* [in Russian], Khimiya, Moscow (1984).
[9] V. S. Kuksenko, *Physics of Strength and Plasticity* [in Russian], Nauka, Moscow (1986).

Translated by R. M. Durham

Vortex structures in a ceramic under high-velocity impact

V. A. Gorel'skiĭ and S. A. Zelepugin

Tomsk Branch of the Institute of Structural Macrokinetics, Russian Academy of Sciences
(Submitted April 11, 1997)
Pis'ma Zh. Tekh. Fiz. **23**, 86–90 (December 26, 1997)

A finite-element method in a two-dimensional axisymmetric formulation is used to analyze the characteristics of shock-wave processes in a ceramic plate under the impact of a high-speed cylinder. It is established that a vortex structure is formed and the evolution of the vortices is investigated. © *1997 American Institute of Physics.* [S1063-7850(97)03112-1]

Studies of the behavior of ceramics under dynamic loading carried out so far have predominantly been experimental,[1,2] and simplified models and approaches have mainly been used for calculated estimates. However, the process of high-velocity loading of ceramic targets over a wide range of initial conditions can only be investigated using a single mathematical model by means of numerical simulation.[3,4] Here, a finite-element method in a two-dimensional axisymmetric formulation is used to analyze the characteristics of shock wave processes in a ceramic plate under the impact of a high-velocity cylinder. For the calculations we use a model of a medium vulnerable to damage, in which cracks can form and grow.[3] The system of equations describing the nonsteady-state adiabatic motion of a compressible medium includes equations of continuity, motion, and energy, and an equation describing the change in the specific volume of the cracks.[5]

An analysis is made of a ceramic plate, 10 mm thick and 60 mm in diameter under the impact of a cylindrical steel striker, 7.6 mm in diameter and 25 mm long. Glide conditions were established at the contact surface between the striker and the plate: the initial velocity of the striker was varied in the range 100–1500 m/s. The constants of the mathematical model for the ceramic were taken from Ref. 3. Figure 1 shows the velocity fields in the radial cross section of the ceramic plate and part of the striker profile (the axis of symmetry is at the left). When the ceramic plate receives an impact at a velocity of 100 m/s, a compression wave forms, propagating toward the rear and side surfaces. At the same time, a rarefaction wave forms at the free surface alongside the striker. The interaction between these two waves at the initial stage of the process results in the formation of a vortex structure in the front surface layer of the ceramic plate. Figure 1a shows the displacement of this vortex along the plate. In the plate an arbitrary distinction can be made between the main zone, most actively influenced by the striker, having a radius approximately 3–4 times the striker radius, and the remaining peripheral zone. In the main zone, propagation and interaction of the compression and rarefaction waves is observed between the front and rear surfaces at the initial stage of the process. After some time, new vortex structures form in this region. Figure 1b shows the formation of a vortex in the surface layer of the ceramic plate beneath the striker, caused by the rarefaction wave reaching the front surface.

It is interesting to study the evolution of the first vortex. This continues to propagate along the plate, moving downward at the same time. After 1.8 μs (see Fig. 1b) the center of the structure is located approximately in the middle layer of the ceramic plate. Then, as it continues to move along the plate toward the side surface, the center of the vortex reaches the rear surface of the plate after 4 μs. Then, as it moves into

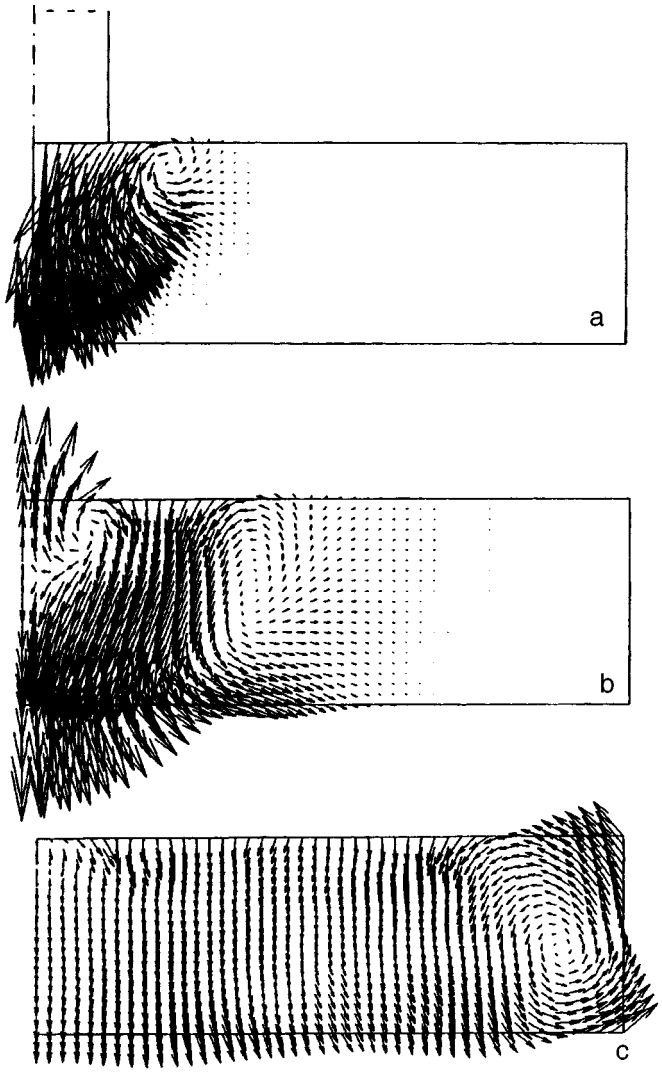

FIG. 1. Velocity field in the radial cross section of a ceramic plate at various times: a—$t=0.7$ μs, b—$t=1.8$ μs, c—$t=6$ μs, and initial impact velocity 100 m/s.

the middle layers, the vortex reaches the side surface after 5.5 μs. Figure 1c shows the instant when the vortex structure is most advanced, encompassing the entire thickness of the ceramic plate. The center of the vortex is located in the middle layers of the plate and is separated from the side surface by approximately half the thickness. The maximum velocity in this region reaches 16.4 m/s after 6.5 μs, which is fairly appreciable relative to the initial velocity of impact. After 8 μs, a short-lived, poorly defined ''antivortex'' structure, of approximately 1 μs duration, with the velocity vectors running in opposite directions, is observed in this region. The velocity field in the plate then becomes equalized and the process continues with the striker and the plate moving as a single entity.

An analysis of the calculations shows that the main factor responsible for vortex formation is the propagation of pressure waves of different sign in the ceramic plate. The rarefaction wave formed at the beginning of the process is localized in the front surface layers of the plate and propagates toward the side surface as the process proceeds. After reaching the rear surface of the plate, the compression wave begins to propagate along the rear surface in the same direction. The emergence of these two mutually opposed waves at the side surface of the plate causes the buildup of the vortex structure shown in Fig. 1c. Changes in the initial parameters such as the geometric dimensions and impact velocity have a substantial influence on the formation of vortex structures. Halving the radius of the plate, while keeping the size of the calculation elements the same, intensifies the mutual influence of the processes in the main and peripheral zones. A vortex structure near the side surface of the plate is observed within 2–3.3 μs. The influence of the peripheral region on the main one can be seen in that a powerful vortex structure, not observed previously, forms in the ceramic beneath the striker within 5.9–6.5 μs. On the whole, the wave processes are more vigorous in this case because of waves being reflected from the side surface of the plate. When the radius of the plate is doubled, a vortex similar to that shown in Fig. 1c still forms in the plate at the same distance from the axis of symmetry, which indicates that the wave factor plays a fundamental role in the formation of vortex structures. The side surface of the plate has no influence in this case, as can be seen from the fact that the maximum velocities in the vortex are almost halved and the center moves along the plate, which was previously prevented by the side surface. As the initial velocity of impact increases, the process of formation of vortex structures in the ceramic changes substantially. Whereas at a velocity of 300 m/s, the process is qualitatively similar to that analyzed above, at velocities of 600 m/s and above, the rarefaction wave is initially suppressed near the front surface and a vortex structure similar to that shown in Fig. 1a does not form. However, a vortex similar to that shown in Fig. 1c forms in the ceramic over the entire range of impact velocities. At velocities above 600 m/s the center of this vortex becomes mobile and its lifetime increases to 1–1.5 μs. With increasing velocity, the relative maximum velocity in the vortex decreases, being 10.2% of the initial impact velocity at 300 m/s, 7.4% at 600 m/s, and 6.6% at 1000 m/s. When a steel plate of the same dimensions is used, no regions with such clearly defined vortex motion are observed. The vortex near the side surface, which is the most clearly defined vortex structure in a ceramic, does not appear at all in a steel plate.

This work was supported by the Russian Fund for Fundamental Research (Grants Nos. 96-03-33659 and 97-01-00218).

[1] V. B. Lazarev, A. S. Balankin, A. D. Izotov, and A. A Kozhushko, *Structural Stability and Dynamic Strength of Inorganic Materials* [in Russian], Nauka, Moscow (1993).
[2] S. J. Bless, Z. Rosenberg, and B. Yoon, Int. J. Impact Eng. **5**, 165 (1987).
[3] V. A. Gorel'skiĭ and S. A. Zelepugin, Prob. Prochnost. No. 5–6, 87 (1995).
[4] G. R. Johnson and T. Holmquist, EXPLOMET-90, *Shock Waves and High Strain Rate Phenomena in Materials*, edited by M. A. Meyers, L. E. Murr, and K. P. Staudhammer (Marcel Dekker, 1992), pp. 1075–1081.
[5] V. A. Gorel'skiĭ, S. A. Zelepugin, and V. F. Tolkachev, Izv. Akad. Nauk MTT No. 5, 121 (1994).

Translated by R. M. Durham

Influence of degradation on the spectrum of voltage fluctuations in thick films of high-temperature superconductors

O. V. Gerashchenko

B. P. Konstantinov Institute of Nuclear Physics, Russian Academy of Sciences, St. Petersburg
(Submitted May 16, 1997)
Pis'ma Zh. Tekh. Fiz. **23**, 91–94 (December 26, 1997)

The noise parameters of high-temperature superconductors (yttrium barium cuprites) have been studied before and after degradation. The samples were thick films—10.5 mm×5.5 mm ×8 μm—fabricated by magnetron sputtering on a ZrO substrate. A model is proposed for the onset of voltage fluctuations. The results of the measurements confirm that the observed noise spectrum is caused by fluctuations in the resistivity. © *1997 American Institute of Physics.* [S1063-7850(97)03212-6]

It is known that condensation of water vapor on the surface of high-temperature superconductors—yttrium barium cuprites—during thermal cycling leads to deterioration (degradation) of the superconducting properties, so that it is of considerable interest to study the influence of degradation on the electrophysical characteristics of the material. In the present case, the noise parameters of the superconductor were studied before and after degradation.

The samples were thick, 10.5 mm×5.5 mm×8 μm, films of $YBa_2Cu_3O_{7-\delta}$ high-temperature superconductor prepared by magnetron sputtering on a ZrO substrate.

The sample was placed in an electromagnetic screen in a helium atmosphere and was cooled to liquid nitrogen temperature in a zero magnetic field. A static magnetic field H was applied perpendicular to the plane of the sample and to a direct current j, which flowed along the long side of the sample. The measurements were made using a standard four-contact system. The voltage $V(t)$ from potential contacts, separated by the distance $d=1.5$ mm, was passed via a step-up transformer to an amplifier, a low-frequency filter, and an analog-to-digital converter installed in a personal computer. The spectral power density of the voltage fluctuations $S_V(f)$ (equal to the mean square $\overline{V^2}(f)$ in a 1 Hz frequency band) was calculated by a fast Fourier transformation. The critical current of the superconductor was determined in the linear part of the current-voltage characteristic from the cutoff to zero voltage. After the measurements, the sample was heated in air at room temperature (19 °C), at normal pressure and humidity (around 60%). The measurements were repeated after approximately 10 h.

Figure 1 shows the spectral density of the voltage fluctuations $S_V(f)$ before degradation of the sample. The spectral intensity increases in the low-frequency range because of the system noise, since the signal-to-noise ratio is low in this range and thus, when the intrinsic noise of the system is subtracted from the measured spectral density, this gives a large error.

It can be seen that for $f \geqslant 100$ Hz, $S_V(f)$ consists of ''white'' noise. Assuming that the voltage fluctuations are generated by independent motion of magnetic flux quanta Φ_0 under the action of the Lorentz force (see Refs. 1 and 2), in the low-frequency limit ($f \ll \tau^{-1}$, where $\tau \sim (dwB)/\overline{V}$ is the transit time for a vortex in the sample, $\overline{V}$ is the average voltage drop at the potential contacts, d is the distance between them, w is the sample width, and B is the magnetic induction) we obtain $S_V(0)=2\Phi_0\overline{V}$. In our case, the critical current density was $j_c(H=0)\approx 30$ A/cm^2, and $\tau^{-1} \sim 10^4$ Hz. The spectral density was $S_V(0)=2.4\times10^{-20}$ V^2/Hz for $H=0$ Oe and $S_V(0)=7\times10^{-19}$ V^2/Hz for $H=318$

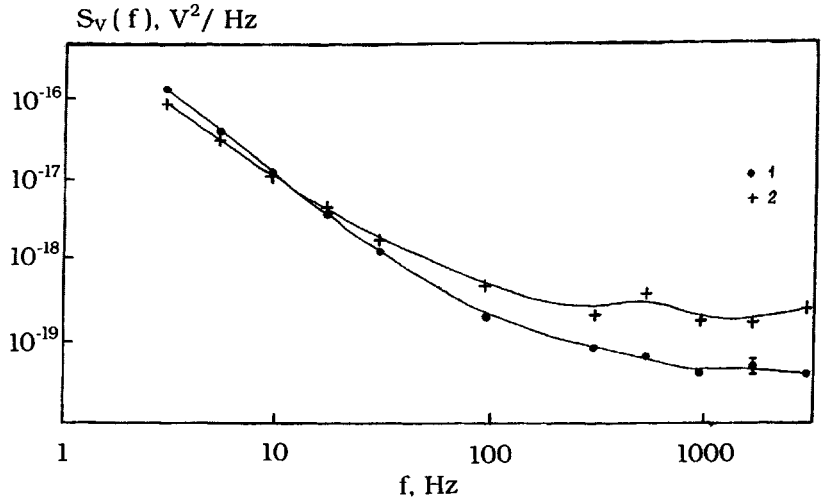

FIG. 1. Spectral power density of voltage fluctuations for $H=0$ Oe (*1*) and $H=318$ Oe (*2*) and a transport current density $j=1.43$ A/cm^2, $T\approx 78$ K. Sample before degradation.

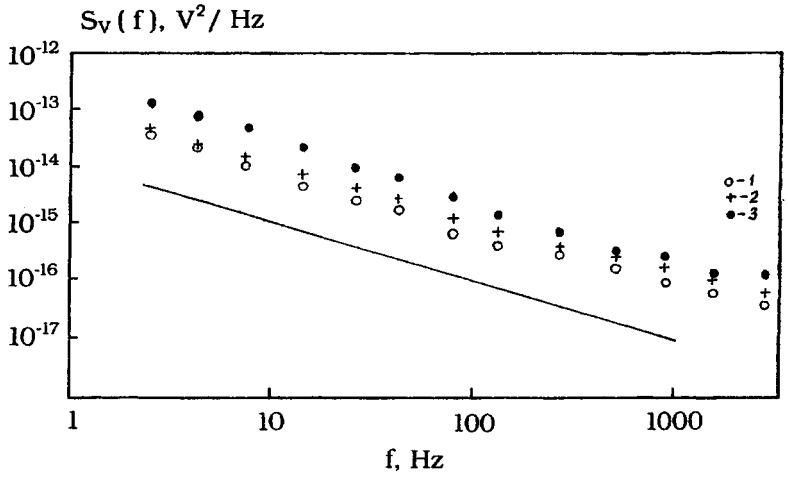

FIG. 2. Spectral power density of voltage fluctuations for $H=96$ Oe (*1*), $H=194$ Oe (*2*), and $H=400$ Oe (*3*). Transport current density $j=1.43$ A/cm^2, $T\approx 78$ K. Sample after degradation. The straight line has the slope $\gamma=-1$.

Oe. The measured fluctuation intensities in the white part of the spectrum were of the same order of magnitude (the difference did not exceed a factor of two). Thus, it is proposed that a model for the occurrence of voltage fluctuations as a result of the independent motion of magnetic flux vortices may be used to obtain an approximate estimate of the fluctuation intensity for these thick-film high-temperature superconductors.

After the sample had been heated in air and held for around 10 h, the experiments were repeated. It was found that the sample retained its superconducting properties but the critical current density was drastically reduced to $j_c\approx 1$ A/cm^2. Figure 2 gives the voltage fluctuation spectra of the same sample for the same transport current.

It can be seen that first, the absolute intensity of the fluctuations increased (by more than three orders of magnitude compared with the value before degradation and by two orders of magnitude for $f=1$ kHz, compared with the model value $S_V(0)=2\Phi_0\overline{V}\sim 10^{-18}$ V^2/Hz). It should also be noted that the relative intensity of the fluctuations is increased, for example, for $f=1$ kHz we have $S_V/\overline{V^2}\sim 10^{-11}$ Hz^{-1} before degradation and $\sim 10^{-9}$ Hz^{-1} after degradation.

Second, the frequency dependence of the spectrum changed fundamentally, now being described by $S_V(f)\sim 1/f^{\gamma}$, where $\gamma\approx 1$. The intensity of the spectrum was still sensitive to the external magnetic field (which also indicates that the sample retained its superconducting properties). Note that a $1/f$ spectrum is frequently observed when studying high-temperature superconductors (see Refs. 3 and 4) and is associated with resistivity fluctuations. The author also tends to this view, since degradation leads to an increased fraction of nonsuperconducting phase in the sample and thus to greater inhomogeneity (granulation), which may be a source of $1/f$ noise.

The author would like to thank M. A. Pustovoĭt and A. I. Sibilev for assistance with this work.

[1] J. D. Thompson and W. C. H. Joiner, Phys. Rev. B **20**, 91 (1979).
[2] S. M. Bezrukov and A. I. Sibilev, Preprint No. 1478 [in Russian], B. P. Konstantinov Institute of Nuclear Physics, Academy of Sciences of the USSR, Leningrad (1989).
[3] *Noise in Physical Systems and* 1/*f Fluctuations*, AIP Conference Proceedings No. 285, edited by P. Handel and A. L. Chung (AIP Press, New York, 1993).
[4] in *Proceedings of the 13th International Conference on Noise in Physical Systems and* 1/*f Fluctuations*, edited by V. Bareikis and R. Katilius, Palanga, Lithuania, 1995.

Translated by R. M. Durham